COMPUTATIONAL MODELING OF INTRACAPILLARY BACTERIA TRANSPORT IN TUMOR MICROVASCULATURE

Peter Windes

Thesis submitted to the faculty of the Virginia Polytechnic Institute and State University in partial fulfillment of the requirements for the degree of

Master of Science
in
Mechanical Engineering

Danesh K. Tafti, Chair

Bahareh Behkam, Co-chair

Rui Qiao

September 23, 2016
Blacksburg, Virginia

Keywords: computational fluid dynamics, immersed boundary method, capillary, red blood cell, bacteria, drug delivery, microvasculature, computational biology

Computational Modeling of Intracapillary Bacteria Transport in Tumor Microvasculature

Peter Windes

Abstract

The delivery of drugs into solid tumors is not trivial due to obstructions in the tumor microenvironment. Innovative drug delivery vehicles are currently being designed to overcome this challenge. In this research, computational fluid dynamics (CFD) simulations were used to evaluate the behavior of several drug delivery vectors in tumor capillaries—specifically motile bacteria, non-motile bacteria, and nanoparticles. Red blood cells, bacteria, and nanoparticles were imposed in the flow using the immersed boundary method. A human capillary model was developed using a novel method of handling deformable red blood cells (RBC). The capillary model was validated with experimental data from the literature. A stochastic model of bacteria motility was defined based on experimentally observed run and tumble behavior. The capillary and bacteria models were combined to simulate the intracapillary transport of bacteria. Non-motile bacteria and nanoparticles of 200 nm, 300 nm, and 405 nm were also simulated in capillary flow for comparison to motile bacteria. Motile bacteria tended to swim into the plasma layer near the capillary wall, while non-motile bacteria tended to get caught in the bolus flow between the RBCs. The nanoparticles were more impacted by Brownian motion and small scale fluid fluctuations, so they did not trend toward a single region of the flow. Motile bacteria were found to have the longest residence time in a 1 mm long capillary as well as the highest average radial velocity. This suggests motile bacteria may enter the interstitium at a higher rate than non-motile bacteria or nanoparticles of diameters between 200 nm and 405 nm.

Computational Modeling of Intracapillary Bacteria Transport in Tumor Microvasculature

Peter Windes

General Audience Abstract

The last 50 years have brought significant advancements in cancer treatment. Despite progress, cancer still remains one of the leading causes of death. In 2016, an estimated 1.7 million new cases of cancer will be diagnosed, and nearly 600,000 people will die from the disease in the United States alone. This is due to numerous unsolved challenges in the field of cancer research. The present study looks at one of these challenges—specially the delivery of drugs into a solid tumor. Several biological factors prohibit chemotherapy drugs from fully penetrating tumors. This prevents the drugs from completely killing the cancer, and can lead to ineffective treatment or recurrence. Innovative new techniques to help drugs better penetrate tumors are under development. One such technique is to harness bacteria to carry drugs inside of tumors. The goal of the present research is to evaluate the behavior of drug carrying bacteria with computer simulations. Blood vessels carry things in and out of tumors. The smallest blood vessels, the capillaries, are the location at which bacteria enter the tumor. The computer simulations found potential for swimming bacteria to enter the tumor at greater rates than other methods of drug delivery. Behavior of bacteria in capillaries is important, but just one of many aspects of this treatment strategy so research is ongoing. Beyond the simulations run for this study, the computer software developed during this project could also have other applications in engineering and biology research.

Acknowledgements

I would like to thank my advisors, Dr. Danesh Tafti and Dr. Bahareh Behkam, for all their help and guidance along the way. I have gained immeasurable insight from them over the past few years. Their expertise and passion in their respective fields is inspiring. I would also like to thank my third committee member Dr. Rui Qiao for his time and involvement.

Additionally, I am grateful to the past and current members of the HPCFD lab—Amit, Nagi, Husam, Hamid, Long, Keyur, Adam, Cody, Susheel—and members of the MicroN BASE lab—Chris, Zhou, Eric, Carmen, Apratim, Carolyn—for their collaboration and insight. I would like to thank Long for his help with IBM, Keyur for his help with Fortran, and Eric for his insight on bacteria modeling. Also, I owe many thanks to Nagi for his work implementing IBM.

I would like to thank Dr. Erik Anderson and Dr. Mark Paul for instilling in me a fascination with the field of fluid mechanics. I would like to thank Dr. George Chamoun for introducing me to the field of CFD.

I would like to especially thank my parents Larry and Lois Windes for their love and support over the years. Also, I would like to thank my family—Emily, Amanda, and Andrew—and all my friends for their support.

I would like to acknowledge Advanced Research Computing at Virginia Tech for providing the computational resources and technical support which made this work possible. I would also like to thank the Department of Mechanical Engineering at Virginia Tech for giving me the opportunity to study here over the past few years. This research was partially supported by the Institute for Critical Technology and Applied Science at Virginia Tech.

Table of Contents

Nomenclature

Chapter 2

$\vec{u}$	fluid velocity $\langle u, v, w \rangle$
$\vec{x}$	position in physical coordinates $\langle x, y, z \rangle$
t	time
p	pressure
ρ	density
μ	viscosity
Re	Reynolds number
$*$	denotes dimensional quantity (superscript)
ref	denotes reference quantity (subscript)
i	solid body vertex index (subscript)
j	solid body surface element index (subscript)
k	velocity movement probe index (subscript)
N_i	total number of solid body vertices
N_j	total number of solid body surface elements
N_k	total number of velocity movement probes
$\vec{F}_c$	total force acting on a solid body
$\vec{M}_c$	total moment about the mass centroid acting on a solid body
$\vec{r}$	radius vector from solid body centroid to a point
$\vec{p}_i$	position of ith solid body vertex in physical coordinates
$\vec{s}_j$	position of jth solid body surface element in physical coordinates
$\vec{x}_c$	solid body centroid position
$\vec{v}_c$	solid body linear velocity
$\vec{a}_c$	solid body linear acceleration
$\vec{\theta}_c$	solid body orientation
$\vec{\omega}_c$	solid body angular velocity about centroid
$\vec{\alpha}_c$	solid body angular acceleration about centroid
n	denotes time step number (superscript)

$\left[R_{\vec{\theta}_c}\right]$	rotation matrix
$\vec{\vec{I}}$	mass moment of inertia tensor
^	denotes unit vector (superscript)

Chapter 3

D	capillary diameter
$A_{capillary}$	cross sectional area of the capillary
H_T	tube (capillary) hematocrit
H_D	discharge (system) hematocrit
$L_{spacing}$	axial distance between consecutive RBC centroids
δ_{plasma}	plasma layer thickness
d_{RBC}	deformed red blood cell diameter
V_{RBC}	volume of a red blood cell (mean corpus volume)
A_{RBC}	surface area of a red blood cell
u_c	axial RBC velocity
u_p	axial plasma velocity averaged over a x-slice
$\bar{u}$	total axial velocity of RBCs and plasma
Q	total volumetric flow of RBCs and plasma
ΔP	axial pressure drop in capillary
μ_{app}	apparent viscosity in the capillary
μ_{rel}	relative apparent viscosity as compared to plasma viscosity

Chapter 4

μ	mean
σ	standard deviation
r	random number such that $0 \leq r \leq 1$
Δt	time step size
t_{run}	duration of run
t_{tum}	duration of tumble

$n_{\Delta t,run}$	number of time steps taken during current run
$n_{\Delta t,tum}$	number of time steps taken during current tumble
$\vec{v}_{run}$	Linear velocity during a run
$\vec{\omega}_{tum}$	angular velocity during a tumble
$\hat{d}$	unit vector pointing in the bacterium's forward direction
$\hat{a}$	unit vector along axis of rotation
$\lvert\Delta\vec{\theta}_{tum}\rvert$	magnitude of the angle change during a run

Chapter 5

Re_{eff}	effective Reynolds number
$\bar{u}$	total axial velocity of RBCs and plasma
D_c	capillary diameter
ν_{app}	apparent viscosity (kinematic)
μ_{app}	apparent viscosity (dynamic)
ΔP	axial pressure drop in capillary
$l_{spacing}$	axial distance between consecutive RBC centroids
H_T	tube (capillary) hematocrit
$\bar{u}$	total axial velocity of RBCs and plasma
u_c	axial RBC velocity
u_p	axial plasma velocity averaged over a x-slice
Q	total volumetric flow of RBCs and plasma
Stk	particle stokes number
t_0	particle relaxation time
D_{par}	diameter of the particle
ρ_{par}	density of the particle
μ_p	blood plasma viscosity
Pe	Peclet number (advection to diffusion ratio)
D	Brownian diffusivity
α^2	Womersley number (level of pulsatility in a flow)
ω	flow oscillation frequency in a blood vessel

De	Dean number (quantification of centripetal effects)
D_v	blood vessel diameter
k_B	Boltzmann's constant
T	temperature (Kelvin)
μ_p	plasma viscosity (dynamic)
Δt	time step size

Abreviations

CFD	Computational Fluid Dynamics
RBC	Red Blood Cell (erythrocyte)
IBM	Immersed Boundary Method
GenIDLEST	Generalized Incompressible Direct and Large Eddy Simulation of Turbulence
FVM	Finite Volume Method
BiCGSTAB	Biconjugate Gradient Stabilized method
ALE	Arbitrary Lagrangian-Eulerian method
hct	hematocrit
FEM	Finite Element Method
MPI	Message Passing Interface
COR	Coefficient Of Restitution
ESL	Endothelial Surface Layer
ECM	Extra Cellular Matrix
VEGF	Vascular Endothelial Growth Factor

1. Pharmacokinetics in Solid Tumors

Of the three primary modes of cancer treatment—surgery, radiation, and chemotherapy—chemotherapy is the broadest category with considerable potential for new breakthroughs [1]. However, a major challenge for chemotherapy is transporting the drug to the desired location in a high enough concentration to be effective. The tumor microenvironment poses many obstacles to the delivery of drug molecules. In recent years, there has been considerable research into new targeted drug delivery schemes in order to combat delivery challenges. Chemotherapy research has expanded into a large cross-disciplinary effort beyond simply biology and medical researchers. Recently, it has become apparent that a better understanding of biophysical phenomena may lend important insight into solving biological problems such as drug delivery [1, 2]. One such area of biophysics particularly important in drug transport is fluid dynamics. The aim of the present work is to study the intracapillary transport of a novel drug delivery method—bacteria mediated therapy—from a biophysics perspective focusing specifically on the fluid dynamics aspect. This chapter will give a brief summary of tumor characteristics before discussing the scope and objectives of the present work.

1.1 Cancer and Its Treatment

1.1.1 Tumor Physiology

The human body contains approximately 10^{13} cells [1]. Each cell's life cycle consists of highly regulated dividing, differentiating, and death based on complex signaling networks in the body. When these processes are working properly, the cell is said to be in homeostasis. However, every day each cell may experiences thousands of DNA damaging events [1]. These corruptions of DNA, or mutations, can produce proteins which impact controlled cell death thereby throwing

off homeostasis. This, in turn, can result in an uncontrolled proliferation of abnormal cells. Typically, such rogue cells are cleared by the immune system before becoming problematic. However, successive rounds of mutations and natural selection may result in a population of abnormal cells able to evade the immune system [3]. Eventually, a malignant tumor mass is formed. Overtime the tumor may continue to grow causing damage to nearby tissue and organs. Additionally, some cancer cells may migrate to other areas of the body in a process called metastasis which is responsible for 90% of cancer related deaths [4].

Cancer is more properly a category of diseases rather than a single disease. There exist over 100 distinct types of cancer [3]. Each form of cancer presents unique characteristics and treatment challenges—no two cancers are identical. However, there are several common functional capabilities all cancers have been observed to possess. First, abnormal cancer cells sustain proliferative growth signals allowing them to replicate rapidly without needing external signaling to do so. Second, the cells are able to ignore anti-growth signals which could stop or slow their proliferation. Third, they have the ability to evade apoptosis—that is, they simply do not die when a normal cell should die. Fourth, unlike healthy cells which have a limited number of divisions, cancer cells can continue dividing indefinitely. Fifth, cancer cells can trigger the growth of their own blood vessels in a process called angiogenesis. Lastly, cancer cells can metastasize and invade other tissues. [5]

1.1.2 Treatment Strategies and Challenges

As one of the leading causes of death worldwide, cancer has received much attention from the scientific and medical community. There is a wide range of survival rates across types of cancer. Some forms of cancer do not respond well to current treatment methods—the need for

innovation is clear in these cases. However even for well treatable cancers, new strategies could be hugely beneficial in reducing the adverse side effects of current treatments [6].

The three major categories of treatment which are currently in use are surgery, radiation, and chemotherapy. Surgical removal of the cancer tumor, when accessible, is widely used. However, it is normally paired some form of post-surgical treatment. In isolation, surgery has a limited impact on long term survival rates of cancer patients [1]. Radiation therapy is used to damage the DNA of cancerous cells causing them to die. Like surgery, radiation is often combined other treatment methods. In certain cancers radiation can be highly effective, but the method has limitations [1].

Chemotherapy is the treatment of cancer by drugs. Often, the term chemotherapy is used to refer to cytotoxic drugs which directly poison cancer cells. More generally, however chemotherapy is an umbrella term referring to any cancer treatment method using an ingested or injected chemical compound [1]. When introduced into the body, conventional chemotherapeutic agents indiscriminately circulate through the vasculature and into all tissues of the body, not just the cancerous region. Thus, the dosage of treatment must be finely tuned to minimize systemic toxicity. Even so, adverse side effects are common when undergoing chemotherapy. At the maximum tolerable dose, the therapeutic may not even penetrate all regions of the tumor. Poor drug penetration into the tumor is primarily due to abnormal vascular structure, elevated interstitial fluid pressure, and a dense interstitial structure resulting from cells proliferating in a confined volume. Incomplete penetration may lead to ineffective treatment, acquired resistance, or resurgence of the tumor later on when the untreated cells start to multiply. [4].

1.1.3 Targeted Drug Delivery

Targeted drug delivery is a phrase used throughout the literature to not so much describe a treatment strategy, but rather a treatment objective. The goal of targeted drug delivery is to maximize the effectiveness of a treatment while minimizing the adverse side effects. In order to maximize effectiveness, a drug must penetrate into all regions of the tumor—often certain regions of the tumor are poorly perfused by blood which prevents transport of therapeutics into those regions. In order to minimize side effects, a treatment should act locally to the tumor and have a limited impact on healthy tissue. There are many proposed strategies to achieve each of these two desired results.

One strategy which attempts to locally raise the concentration of therapeutic in the tumor environment is the use of nanoparticles as a delivery method. Tumor vasculature contains large pores or fenestrations as wide as 380 nm to 780 nm in diameter which allow nanoparticles to exit into the tumor interstitium [6]. However, the particles cannot easily enter heathy tissue which does not have large pores in its vasculature. In practice, less than 5% of nanoparticles—but typically under 1%—actually end up in the tumor site with the majority ending up in the liver and spleen [6]. Regardless, the technique has shown some limited success in drug trials and there are currently several clinically approved nanoparticle chemotherapeutics [7].

Another proposed strategy for improving drug penetration and lowering systemic toxicity is bacteria mediated therapy. Certain strains of *Bifidobacterium infantis*, *Clostridium tetani*, and *Salmonella* Typhimurium bacteria have been shown to possess a natural ability to penetrate and colonize solid tumors [8-10]. Bacteria alone may have some antitumor properties, but their effectiveness in immunocompetent patients is very limited due to the rapid clearing of the bacteria by the immune system [11]. Steps can also be taken to improve the effectiveness of

bacteria therapies. One such strategy is to attach biofunctionalized nanoparticles to the body of bacteria to be carried into a tumor. Another strategy is to use synthetic biology to engineer bacteria to release antitumor agents inside the tumor [12, 13]. Further research is needed to bring bacteria mediated treatments to clinical trials, but the strategy has shown early promise.

1.2 Modeling Bacteria Mediated Therapy

Any cancer therapeutic must be transported by convection and diffusion from the point of injection to the tumor site. Thus, fluid dynamics plays a prominent role in the transport process. The present work uses computational fluid dynamics (CFD) simulations to uncover biophysical insight into the transport of novel cancer treatment agents—specifically, bacteria and nanoparticle agents. Upon injection into a blood vessel, a therapeutic must first travel through the vasculature into a tumor capillary, then out of the capillary into the interstitium, and lastly through the interstitium to each cancer cell. The scope of the present work will be limited to intracapillary transport.

Due to the similar scales of capillaries and red blood cells (RBC)—both on the order of 10 μm—RBCs play a prominent role in the hydrodynamics of the capillary environment. Thus, the elements which will be included inside the capillary domain in the present computational model are red blood cells, plasma, and bacteria or nanoparticles. Other blood cells such as platelets and white blood cells are neglected due to their low mass fraction in whole blood and therefore negligible role in capillary hydrodynamics. The goal is to examine hydrodynamic interactions between elements in the capillary with a focus on the location and movement of the bacteria or nanoparticles. The primary interest in the present work is on bacteria based therapeutic agents, but nanoparticles are also be simulated for comparison.

The intracapillary transport of motile bacteria, non-motile bacteria, and nanoparticles will be modeled using CFD, the immersed boundary method (IBM) and a stochastic agent based bacteria model. Chapter 2 will outline the numerical methodology used in the computational modeling. Chapters 3 and 4 will describe the capillary and bacteria models respectively. Chapter 5 will describe the setup for the nanoparticle and bacteria transport simulations, and provide results and analysis. Questions to be answered by the end of the study are, what is the effect of motility in the transport of bacteria agents in a capillary, and how do motile and non-motile bacteria behave compared to nanoparticle agents in a capillary?

2. **Numerical Methodology**

This chapter will discuss the numerical methods used for simulating the transport of bacteria in capillaries. An incompressible Navier-Stokes solver (GenIDLEST [14]) was used to model the fluid flow of the blood plasma in the domain. The fully developed flow assumption was employed for simulating periodic flow through a characteristic repeating section of capillary. The immersed boundary method was used for modeling solids in the flow—the cylindrical capillary wall, the red blood cells, and the bacteria. Two procedures were used for moving the immersed rigid bodies in the flow. One method was based on fluid forces, and was employed to develop the capillary model in Chapter 3. The other method was movement based on the surrounding fluid velocity which was used for the main simulations discussed in Chapter 5. Lastly, solid-solid contact detection and handling will be described.

2.1 Fluid Modeling

2.1.1 Governing Equations

The incompressible Navier-Stokes equations are the governing equations for the blood plasma. The non-dimensionalized vector form of conservation of momentum (2.1) and mass (2.2) are,

$$\frac{\partial \vec{u}}{\partial t} + \vec{u} \cdot \nabla \vec{u} = -\nabla p + \frac{1}{Re} \nabla^2 \vec{u} \tag{2.1}$$

$$\nabla \cdot \vec{u} = 0 \tag{2.2}$$

The non-dimensionalized was done using the parameters,

$$\vec{x} = \frac{\vec{x}^*}{L^*_{ref}}, \qquad \vec{u} = \frac{\vec{u}^*}{U^*_{ref}}, \qquad t = \frac{t^* u^*_{ref}}{L^*_{ref}},$$

$$\rho = \frac{\rho^*}{\rho^*_{ref}}, \qquad \mu = \frac{\mu^*}{\mu^*_{ref}}, \qquad p = \frac{p^* - p^*_{ref}}{\rho^*_{ref} {U^*_{ref}}^2},$$

$$Re = \frac{\rho^*_{ref} U^*_{ref} L^*_{ref}}{\mu^*_{ref}}$$

where * denotes dimensional quantities. The energy equations is neglected since temperature is constant and not of interest.

Flow simulations were conducted using an in-house code, GenIDLEST (Generalized Incompressible Direct and Large Eddy Simulation of Turbulence). A brief description of the solution method will be provided here but a more full treatment can be found in Tafti 2001 [14]. The fluid domain is discretized into a structured mesh, and a mapping is created between physical coordinates (x, y, z) and computational coordinates (i, j, k). The governing equations in conservative form are discretized using the finite volume method (FVM). A structured non-staggered formulation is used where the velocities and pressures are stored at the cell centers, and contravariant mass fluxes are calculated and stored on the cell faces. A pressure based predictor-corrector solution method is used. During the predictor step, the momentum equations are iteratively solved without the pressure term to obtain a preliminary velocity field. Once a given tolerance is reached, the corrector step is carried out by iteratively solving the pressure Poison equation to obtain a divergence free velocity field. The momentum and pressure linear systems are solved using a stabilized biconjugate gradient solver (BiCGSTAB) with preconditioning. In all calculations in the present work, the predictor momentum equations were solved to a tolerance of 1×10^{-10}, and the corrector pressure equation was solved to a tolerance of 1×10^{-12}.

2.1.2 Boundary Conditions

The capillary validation simulations run in Chapter 3 used a developing flow framework. The boundary condition on the inlet of the capillary cylinder was “inflow”—that is the velocity was set to a fixed value. The boundary condition at the outlet of the capillary was “outflow”—that is, the gradient in the velocity was set to zero. The capillary wall boundary condition was imposed using the immersed boundary method which will be described later in this chapter (section 2.2.1). The main simulations of therapeutic transport (bacteria or nanoparticles) were done in a periodic framework. This was done using the fully developed flow assumption. In this framework, a pressure source term is applied in the streamwise direction driving the flow. The pressure computed is the fluctuation pressure above or below the local pressure at a slice in x. Fluid and solids exiting the domain re-enter the inlet of the domain. A more complete description of the process may be found in Patankar et al., 1977 [15] and Zhang et al., 1997 [16].

2.2 Solid Modeling

2.2.1 Immersed Boundary Method

Basic CFD modeling is done by discretizing the fluid domain and applying boundary conditions on the exterior of the fluid mesh. One such boundary condition is the no-slip condition which simulates a fluid-solid interface. However, it may be desired to have solids moving around inside the fluid. There are several common techniques used to achieve this—sliding mesh methods, dynamic mesh methods, arbitrary Lagrangian–Eulerian methods (ALE), or immersed boundary methods (IBM). In the present work, a sharp interface immersed boundary method is used to

simulate moving solids within the flow. Henceforth, this will simply be referred to as IBM, and will refer to the implementation in the GenIDLEST code [17].

IBM is often used to simulate complex geometries and moving solids in low or moderate Reynolds number flows [18]. Conceptually, IBM works by imposing a no slip condition at any location in the fluid domain without requiring the fluid mesh to conform to the solid body. For example when simulating a cylinder, the difference between body conformed mesh and immersed boundary is shown in Figure 2.1.

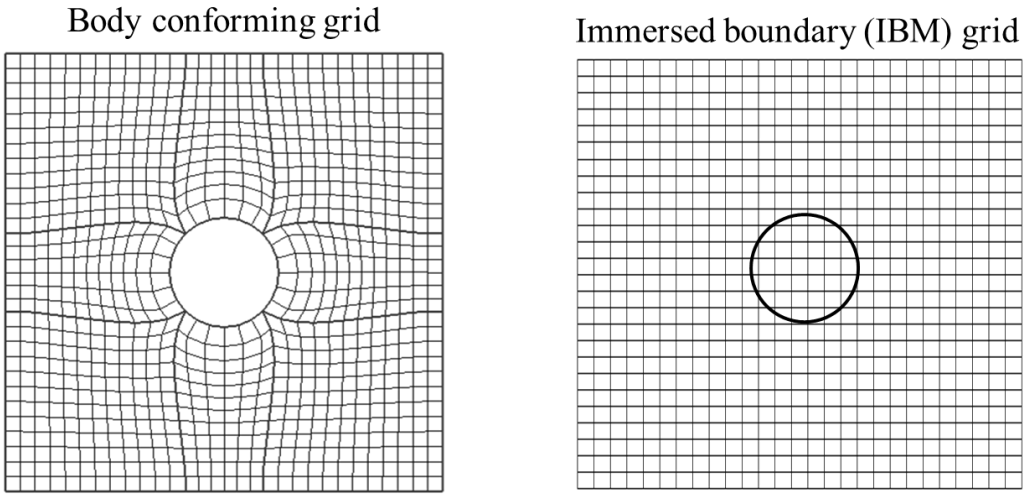

Figure 2.1. Left: when simulating flow around a cylinder using a body conformed grid, only the fluid volume is meshed. Right: the same setup is achieved using the immersed boundary method by defining the fluid-solid interface at a location within the fluid mesh.

When using IBM, the fluid-solid interface is tracked in the flow at each time step with a triangular surface mesh within the three dimensional fluid mesh. The corners of each triangle of the mesh will be referred to as vertices, and the area centroids of each triangle will be referred to as surface elements. Based on the location of the boundary, all the nodes in the fluid mesh will be designated as “fluid nodes” on the fluid side of the interface, “solid nodes” on the solid side of the interface, or “IB nodes” directly on the interface.

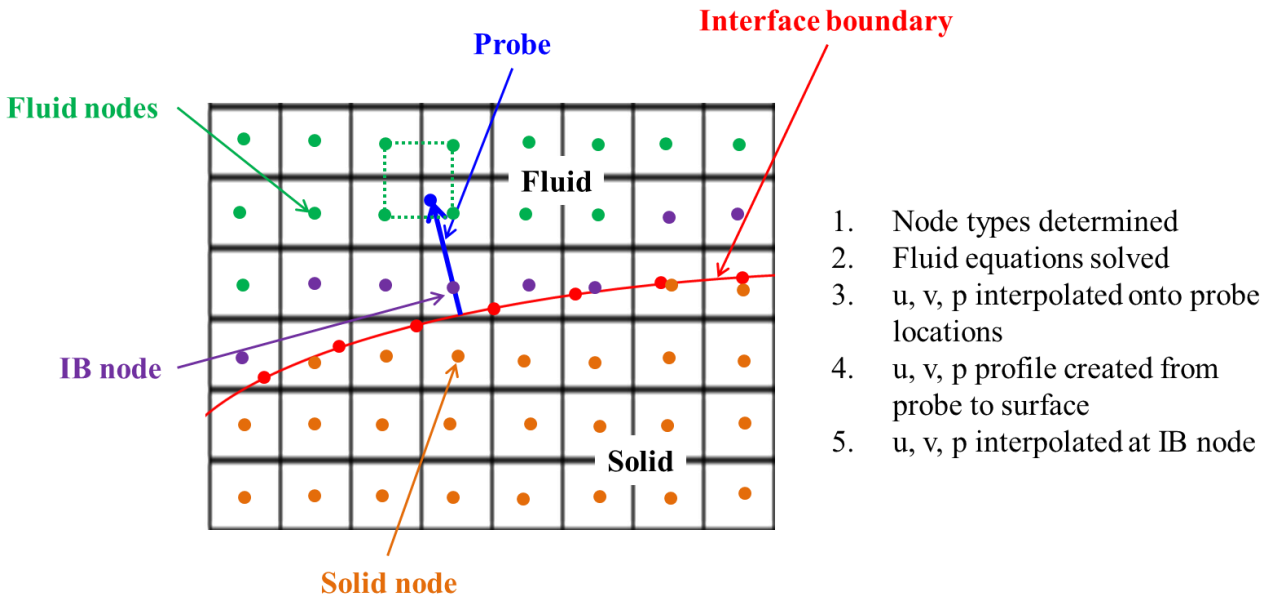

Figure 2.2. The basic process for determining properties at the IB nodes is shown. The red line defines the solid-fluid interface.

Based on the velocity of a given surface element, the nearby fluid velocity is adjusted such that a no slip condition at the sharp interfaces results as summarized in Figure 2.2. The details of this process may be found in Nagendra et al., 2014 [17].

A closed surface of triangular elements makes up a solid IB body. In the present work, all the solid bodies in the flow are considered rigid bodies. The reasoning behind treating RBCs as rigid bodies is explained in Chapter 3. Movement to a rigid body is achieved by changing the coordinates of the vertices defining the surface mesh. Surface element centroids are recalculated at each time step from the three corresponding vertices. Two methods are used to calculate the current position, $\vec{x}_c^{\,n+1}$, and orientation, $\vec{\theta}_c^{\,n+1}$, of the rigid body centroids based on the nearby fluid field—these methods are described in sections 2.2.2 and 2.2.3. Once $\vec{x}_c^{\,n+1}$ and $\vec{\theta}_c^{\,n+1}$ are known, section 2.2.4 describes the process of defining the vertex locations and setting the surface element velocity and acceleration.

2.2.2 Force Based Movement

The force based movement method uses the local fluid velocity field to calculate transient movement of a rigid IB body. It is used in Chapter 3 to calculate the movement of red blood cells. Two fluid forces, the pressure and shear force, act on each surface element of the body. The total force, $\vec{F}_c$, and total moment about the centroid, $\vec{M}_c$, are calculated by integrating these forces over the body at each time step,

$$\vec{F}_c = \sum_{j=1}^{N_{elem}} \vec{F}_{pressure,j} + \vec{F}_{shear,j} \tag{2.3}$$

$$\vec{M}_c = \sum_{j=1}^{N_{elem}} \vec{r}_j \times \left(\vec{F}_{pressure,j} + \vec{F}_{shear,j}\right) \tag{2.4}$$

$$(\vec{r}_j = \vec{s}_j - \vec{x}_c)$$

The force and moments are approximated to be constant over the duration of a given time step. Newton's second law is applied to calculate the acceleration over the time interval between time steps n and n+1,

$$\vec{a}_c{}^{n \to n+1} = \frac{1}{m}\vec{F}_c \tag{2.5}$$

Then, acceleration is numerically integrated twice to calculate the updated velocity and position of the rigid body,

$$\vec{v}_c{}^{n+1} = \vec{v}_c{}^{n} + \vec{a}_c{}^{n+1}\Delta t \tag{2.6}$$

$$\vec{x}_c{}^{n+1} = \vec{x}_c{}^{n} + \vec{v}_c{}^{n+1}\Delta t \tag{2.7}$$

A similar process is used for rotation,

$$\vec{\alpha}_c^{\,n\to n+1} = \vec{\vec{I}}^{-1}\vec{M}_c \tag{2.8}$$

$$\vec{\omega}_c^{\,n+1} = \vec{\omega}_c^{\,n} + \vec{\alpha}_c^{\,n+1}\Delta t \tag{2.9}$$

$$\vec{\theta}_c^{\,n+1} = \vec{\theta}_c^{\,n} + \vec{\omega}_c^{\,n+1}\Delta t \tag{2.10}$$

Note that the inverted moment of inertia tensor must be in global physical coordinates.

Given $\vec{\vec{I}}_{local}$, and a rotation matrix $\left[R_{\vec{\theta}_c}\right]$, the global tensor can be transformed,

$$\vec{\vec{I}}_{global} = \left[R_{\vec{\theta}_c}\right] * \vec{\vec{I}}_{local} * \left[R_{\vec{\theta}_c}\right]^T \tag{2.11}$$

where, $\vec{\vec{I}}_{local} = \begin{bmatrix} I_{xx} & 0 & 0 \\ 0 & I_{yy} & 0 \\ 0 & 0 & I_{zz} \end{bmatrix}$

The end goal for this force based movement model is to determine centroid position, $\vec{x}_c^{\,n+1}$, and orientation, $\vec{\theta}_c^{\,n+1}$ which are given by equations 2.7 and 2.10.

2.2.3 Velocity Based Movement

The velocity based movement method uses the local fluid velocity field to calculate the movement of a rigid IB body in equilibrium with the local fluid flow. This method is valid for low Stokes number objects. It is used in Chapter 5 to calculate the movement of the bacteria and nanoparticles. In this method, the solid body velocity is set to the instantaneous fluid velocity near the object. The velocity is measured at k probes normal to the IB surface at a distance of approximately 5 background grid cell lengths into the flow. The centroidal velocity of the body is set to the average of the probe velocities,

$$\vec{v}_c^{\,n+1} = \frac{1}{N_k}\sum_{k}^{N_k} \vec{u}_k^{\,n+1} \tag{2.12}$$

The rotation is calculated based on the angular velocity of a fluid parcel relative to the solid body centroid at each of the probe location averaged over all the probes.

$$\vec{\omega}_c^{\,n+1} = \frac{1}{N_k}\sum_{k}^{N_k} \vec{\omega}_k^{\,n+1} \tag{2.13}$$

where $\vec{\omega}_k$ at each probe is calculated as,

$$\vec{\omega}_k = \frac{\vec{r}_k \times \vec{v}_k}{|\vec{r}_k \times \vec{v}_k|}\frac{\left|\vec{v}_{k,rel,T}\right|}{|\vec{r}_k|} \tag{2.14}$$

$$(\vec{r}_k = \vec{p}_k - \vec{x}_c)$$

where $\vec{v}_{k,rel,T}$ is the tangential component of the velocity of the probe relative to the centroid velocity as given by,

$$\vec{v}_{k,rel,T} = \vec{v}_{k,rel} - \left(\vec{v}_{k,rel} \cdot \hat{r}_k\right)\hat{r}_k \tag{2.15}$$

$$\left(\vec{v}_{k,rel} = \vec{v}_k - \vec{v}_c, \qquad \hat{r}_k = \frac{\vec{r}_k}{|\vec{r}_k|}\right)$$

Once the linear and angular velocities are known, the accelerations can be determined by,

$$\vec{a}_c^{\,n+1} = \frac{\vec{v}_c^{\,n+1} - \vec{v}_c^{\,n}}{\Delta t} \tag{2.16}$$

$$\vec{\alpha}_c^{\,n+1} = \frac{\vec{\omega}_c^{\,n+1} - \vec{\omega}_c^{\,n}}{\Delta t} \tag{2.17}$$

and the displacement and orientation can be found by,

$$\vec{x}_c^{\,n+1} = \vec{x}_c^{\,n} + \vec{v}_c^{\,n+1}\Delta t \tag{2.18}$$

$$\vec{\theta}_c^{\,n+1} = \vec{\theta}_c^{\,n} + \vec{\omega}_c^{\,n+1}\Delta t \tag{2.19}$$

Now that the centroid position, $\vec{x}_c^{\,n+1}$, and orientation, $\vec{\theta}_c^{\,n+1}$, are known, the vertex locations, element velocities, and element accelerations may be determined from the process which will be described in the next section.

2.2.4 Determination of Surface Location and Velocity

At any time step, the physical coordinates of the surface element centroids must be determined. This is done using the position and orientation of the solid body centroid. Initially, the surface mesh is read into the code giving starting locations of each vertex, $\vec{p}_i^{\,0}$. At each time step the position is calculated by,

$$\vec{p}_i^{\,n+1} = \left(\vec{p}_i^{\,0} - \vec{x}_c^{\,0}\right) * \left[R_{\vec{\theta}_c}\right] + \vec{x}_c^{\,0} + \vec{x}_c^{\,n+1} \; for \; all \; i \tag{2.20}$$

The rotation matrix $\left[R_{\vec{\theta}_c}\right]$ is generated using an axis-angle quaternion [19]. This rotation matrix, when multiplied by any point or vector will rotate it by $\left|\vec{\theta}_c\right|$ radians about an axis defined by the unit vector $\frac{\vec{\theta}_c}{|\vec{\theta}_c|}$.

Once all i vertices, $\vec{p}_i^{\,n+1}$, are in their proper locations, all j surface elements centroid are calculated by,

$$\vec{s}_j^{\,n+1} = \frac{1}{3}\sum_{i=1}^{3} \vec{p}_i^{\,n+1} \; for \; all \; j \tag{2.21}$$

In order to apply the fluid boundary conditions at the surface, the velocity and acceleration of the surface elements must be known. These can be found by,

$$\frac{d\vec{s}_j}{dt} = \vec{v}_c{}^{n+1} + \vec{\omega}_c{}^{n+1} \times \vec{r}_j{}^{n+1} \; for\ all\ j \tag{2.22}$$

$$\frac{d^2\vec{s}_j}{dt^2} = \vec{a}_c{}^{n+1} + \vec{\alpha}_c{}^{n+1} \times \vec{r}_j{}^{n+1} \; for\ all\ j \tag{2.23}$$

$$\left(\vec{r}_j{}^{n+1} = \vec{s}_j{}^{n+1} - \vec{x}_c{}^{n+1}\right)$$

The surface element locations are then transformed from physical to computational coordinates for use in the immersed boundary method.

2.2.5 Solid-Solid Contact

During a simulation with moving solid bodies, overlap between two solids should not occur. However, there is no mechanism inherent in either movement algorithm described in sections 2.2.2 and 2.2.3 which would prevent solid bodies from moving through each other. Thus, a contact detection and collision algorithm was implemented. As will be described further in Chapter 3, the red bloods cells move axially down the center of capillary with relatively constant cell-to-cell spacing. Based on these assumptions, RBC-wall and RBC-RBC collisions do not occur reducing the possible collisions to bacterium-wall or bacterium-RBC. It was assumed that there would be no rebound during bacterium collisions due to the material properties of the soft bodies involved, and viscous damping from the fluid in the system. At any given time step, n, a check was done to determine if the movement of the objects from position n to position n+1 resulted in solid-solid overlap. If so, the displacement in the direction of the collision was reduced to prevent overlap.

2.3 Pseudo-Steady Formulation

Due to the viscous timescale, $\mathcal{O}(10^{-5})$ seconds, being significantly smaller than the timescale of bacteria movement, $\mathcal{O}(1)$ seconds, a pseudo steady state formulation is used for the main bacteria/nanoparticle transport simulations described in Chapter 5. Note that the capillary model validation simulations in Chapter 3 do not use this method because no set simulation duration is needed. Trying to solve a physiological problem in a transient framework would be prohibitively computationally expensive.

Using the pseudo-steady formulation, the fluid equations are solved to steady state without moving the solids or advancing time. Once convergence in the fluid field is achieved, a time step is taken and the solids are moved appropriately based on their respective velocities. Two separate quantities are monitored for convergence in the fluid field the L_∞ norm of the velocity residuals and the change in flowrate. The velocity residual norms are computed by,

$$L_\infty(u_{res}) = max\left(\left|{u_{i,j,k}}^n - {u_{i,j,k}}^{n-1}\right|\right) over\ all\ i,j,k \tag{2.24}$$

$$L_\infty(v_{res}) = max\left(\left|{v_{i,j,k}}^n - {v_{i,j,k}}^{n-1}\right|\right) over\ all\ i,j,k \tag{2.25}$$

$$L_\infty(w_{res}) = max\left(\left|{w_{i,j,k}}^n - {w_{i,j,k}}^{n-1}\right|\right) over\ all\ i,j,k \tag{2.26}$$

where ${u_{i,j,k}}^n$, ${v_{i,j,k}}^n$, ${w_{i,j,k}}^n$, are the velocity values at cell i, k, k at time step n. The change in flow rate, ΔQ, is evaluated at a x-slice located at the inlet (x = 0, i = 1),

$$\Delta Q = \pi R^2 \frac{1}{N_j N_k} \sum_j^{N_j} \sum_k^{N_k} {u_{1,j,k}}^n - \pi R^2 \frac{1}{N_j N_k} \sum_j^{N_j} \sum_k^{N_k} {u_{1,j,k}}^{n-1} \tag{2.27}$$

where, R, is the radius of the capillary. The convergence tolerances reported in Chapter 5 are compared to these four computed values.

3. Capillary and Red Blood Cell Modeling

A capillary is the physiological system which is the site of cancer therapeutics entering the tumor interstitum from the blood volume. Thus, modeling the process of drug transport into a tumor requires a working model of a human capillary. This chapter will discuss the basics of human circulation focusing especially on red blood cells. Then a computational fluid dynamics (CFD) based capillary model containing a characteristic section of capillary with red blood cells and blood plasma will be defined and validated.

3.1 Human Circulation and Blood

3.1.1 Biological Transport Phenomena

Blood is the primary means of transport throughout the human body. Several important transport processes in the body include moving oxygen from the lungs to the cells, moving nutrients from the intestines to the cells, and redistributing excess heat from the core of the body to the periphery. Blood is essential to biological transport because the diffusion of mass and energy in tissue is too slow to be practical. Thus, blood provides a means of transport by convection which is much faster than diffusion. For example, compare the transport of oxygen by diffusion through tissue with the transport of oxygen by convection through a major artery. Using an order of magnitude calculation, it can be shown that oxygen is transported several million times faster in the arteries. Even the smallest blood vessels, the capillaries, transport oxygen approximately twenty times faster than the speed with which oxygen diffuses through tissue [20]. Hence, a sophisticated network of blood vessels is required in the body to maintain function. Tissue cannot survive without a constant supply of oxygen and nutrients. Every cell in the body must lie

within approximately 200 μm of a capillary although this distance is typically closer to 50 μm [4].

3.1.2 Blood Composition

Blood is composed of many parts, each with a specific function in the body. Red blood cells (RBCs), also called erythrocytes, transport oxygen through the body. Five different types of white blood cells, also known as leukocytes, carry out immune function throughout the body. Platelets or thrombocytes cause clotting in the blood to plug leaks in the vasculature walls. Plasma, which is the liquid portion of blood, convects all the blood components through the vasculature. Plasma and red blood cells make up nearly the entire volume fraction of whole blood. Thus, these two components drive the hydrodynamic behavior of blood. White blood cells and platelets have extremely complicated mechanisms by which they carry out important functions in the body. Thus, discussion of them is outside the scope of this work, since hydrodynamics are the primary focus in this paper. [21]

Whole blood is slightly more than half plasma by volume and the remainder is red blood cells. The volume fraction of red blood cells is called “hematocrit” and is often abbreviated hct. A normal hct level in a human is 36% to 50%, thus hct can vary ± 7% from one healthy person to another [22]. Variation can be even more extreme due to outside influences such as living at a high elevation. Additionally, various abnormalities such as bleeding, cancer, sickle cell disease, or bone marrow suppression can cause low hct (called anemia). High hct (called Polycythemia) can be caused by decreased plasma volume or overproduction of red blood cells (called Erythrocytosis) [23]. Both elevated and depressed levels of hct are harmful to human health.

Hematocrit has a strong effect on the viscosity of blood along with other factors such as red blood cell deformability and plasma composition.

Blood plasma is composed of, by weight, 91% water, 1% ions (Na^+, Cl^-, HCO_3^-, Ca^{++}, Mg^{++}, etc.), 7% loose proteins (albumin, globulin, and fibrinogen), and 1% of assorted organic molecules (glucose, lipids, creatinine, lactic acid, urea, etc.) [21]. These components have important physiological functions, and may also affect blood rheology. Until recently blood plasma was considered a Newtonian fluid, however recent research suggests it may contain both non-Newtonian and viscoelastic properties [24]. These may have an impact on flow in the microvasculature, but it is yet unknown the extent to which these complexities affect the flow of plasma. This work uses the standard assumption that plasma is a uniform Newtonian fluid with a viscosity of 1.2×10^{-3} Pa·s [25].

Each microliter, or cubic millimeter, of blood contains approximately 4.2 to 6.1 million red blood cells [26]. Even though blood is a dense suspension of particles, when considered in aggregate, the blood cells and plasma can be approximated as a uniform non-Newtonian fluid. Specifically, the apparent viscosity decreases as the shear rate of the flow increases. Thus, blood is considered a shear thinning fluid described by various mathematical relations between viscosity and shear rate. This approximation is sufficient for the majority of blood vessels however it does not hold at small scales. This is because at small scales individual blood cells—not millions in aggregate—dominate flow behavior. Consideration of individual blood cells becomes important in vessels under 200 μm [27]. Human capillaries are generally classified as blood vessels between 5 and 8 μm in diameter so they are well below this threshold. Since red blood cells are around 8 μm in diameter they deform to fit in capillaries, and are carried through

the flow in a single file fashion. Thus, flow behavior in capillaries is strongly dependent on red blood cell properties.

3.2 Red Blood Cell Characteristics

3.2.1 Red Blood Cell Function

Red blood cells, in the simplest terms, are tiny carriers of oxygen. In structure, each cell is a fluid filled capsule. The internal fluid, or cytoplasm, is a dense hemoglobin solution. Hemoglobin is a molecule which can bind oxygen and is also responsible for the red color of blood. Even though red blood cells makes up less than half the blood volume, the hemoglobin solution inside them carries 98% of the oxygen in blood [28]. This is due to the poor solubility of oxygen in plasma. Without red blood cells and hemoglobin, oxygen transport in blood would not be effective.

Red blood cells have a unique shape which helps them carry out their function of oxygen transport. Unlike many other cells in the body, erythrocytes do not contain organelles or a nucleus with DNA. Erythrocytes are formed in the bone marrow in a process called erythropoiesis. During this multi-step process which takes about seven days, a pluripotent stem cell extrudes its organelles and nucleus, and becomes essentially a bag of hemoglobin. During erythropoiesis, the cell's size decreases and its cytoplasmic volume increases, allowing it to fulfill its role of carrying oxygen to the tissue. Erythrocytes have a life span of only 120 days, thus they are produced at a rate of approximately two million per second to maintain a constant supply in the blood stream. [29]

Red blood cells maintain a biconcave shape when floating freely in plasma. This shape has a high surface area to volume ratio which gives the cell two main advantages. First, transport of oxygen across the cell membrane is enhanced because of a larger surface area. Second, the cell

can deform extensively without significantly stressing its membrane. The three dimensional shape of an average normal red blood cell using an empirically derived equation in cylindrical coordinates is shown by equation 3.1 [30].

$$\frac{z}{3.91} = 0.5 * \left(1 - \left(\frac{r}{3.91}\right)^2\right)^{0.5} * (C_0 + C_1 * \left(\frac{r}{3.91}\right)^2 + C_2 * \left(\frac{r}{3.91}\right)^4) \quad 3.1$$

A scanning electron microscope image alongside the mathematical representation of a red blood cell is presented in Figure 3.1. A volume and surface integration of equation 3.1 yield a surface area of 134.1 μm^2 and volume of 94.1 μm^3. A sphere of equal volume to a red blood cell only has 100 μm^2 of surface area which is about 25% less.

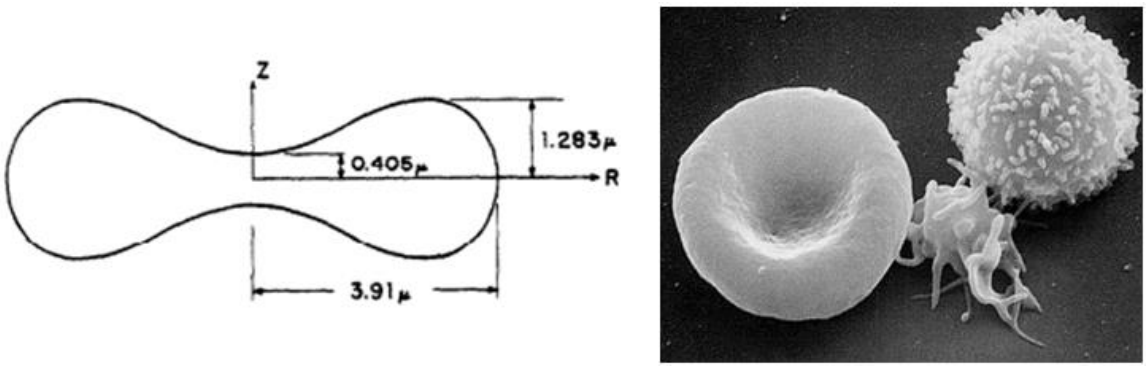

Figure 3.1. Left: size and shape of a red blood cell based on equation 3.1. Right: scanning electron microscope image of a red blood cell (left) along with a platelet (center) and a white blood cell (right) [31].

3.2.2 Red Blood Cell Membrane Structure

During their 120 day life span, red blood cells must pass through the microvasculature around one million times [32]. Thus their membranes must be able to repetitively hold up to large deformations without fatiguing. Additionally these deformations must be fully reversible—that is they cannot undergo plastic deformation or creep. In order to accomplish these criteria, red blood cell membranes are made of two basic parts—the bilayer and the cytoskeleton. The bilayer is made from the hydrophobic sides of two phospholipid sheets binding tail to tail. This creates a

flexible, semipermeable membrane. The cytoskeleton, a spectrin protein network, is necessary to prevent the bilayer from rupturing. The tethering between the cytoskeleton and the phospholipid bilayer occurs at junctions between spectrin fibers by transmembrane proteins such actin. Spectrin is a tetramer protein which gives the red blood cell membrane its structural integrity. An α and β spectrin monomers laterally associate to form a heterodimer. Then these dimers attach in a head to head configuration to form tetramers. The resulting tetramer form a structural web as shown in Figure 3.2 [33].

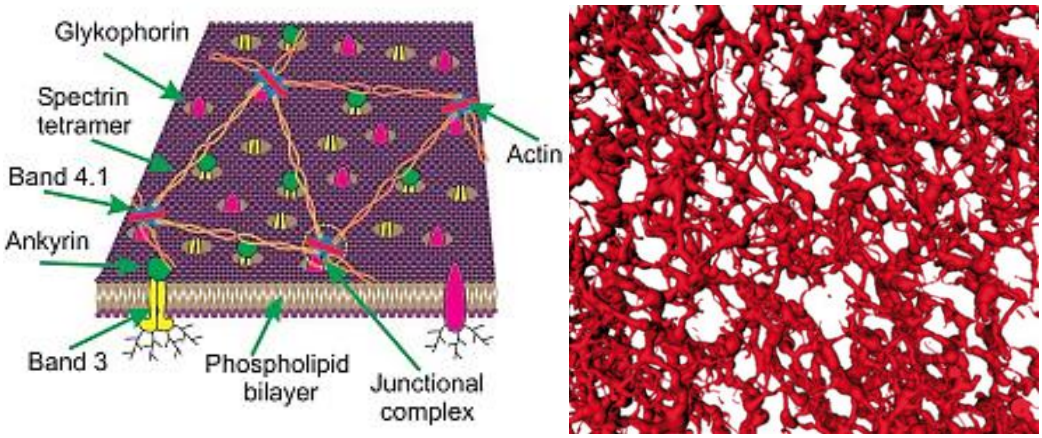

Figure 3.2. Left: schematic of the red blood cell membrane. Spectrin tetramers are tethered to the phospholipid bilayer at junctional complexes by actin and other binding proteins [34]. Right: volume rendering of cryo-tomography of a cytoskeleton spectrin web in a mouse's red blood cell [35].

The spectrin cytoskeleton can dynamically reorganize during a cell's journey in and out of tight vessels. The spectrin tetramers exist in rapid, dynamic equilibrium with spectrin heterodimers. Additionally, spectrin-actin disassociation can occur at the junctional complexes. Three primary factors influence the topography of the spectrin web—mechanical strain energy, thermal fluctuation energy, and biochemical activation. Under low shear stress the cytoskeleton behaviors as a weak elastic solid, but becomes fluidized under high shear. This allows the cell to pass through very small vessels. The spectrin web reorganization possibly accounts for the

dissipation of in-plane shear energy. This would explain why only accounting for bending energy provides such good membrane shape predictions. [34]

3.2.3 Membrane and Cytoskeleton Mechanical Properties

Since a red blood cell membrane is a heterogeneous active fabric, characterization of its properties in simple mechanical terms can be challenging. For some applications, however, it can be modeled as an effective continuum material as indicated in Figure 3.3. Since the membrane is thin, it can also be considered a shell. If the membrane is assumed to be area conserving, the parameters needed to characterize the material properties are reduced to the shear modulus and the bending modulus [36].

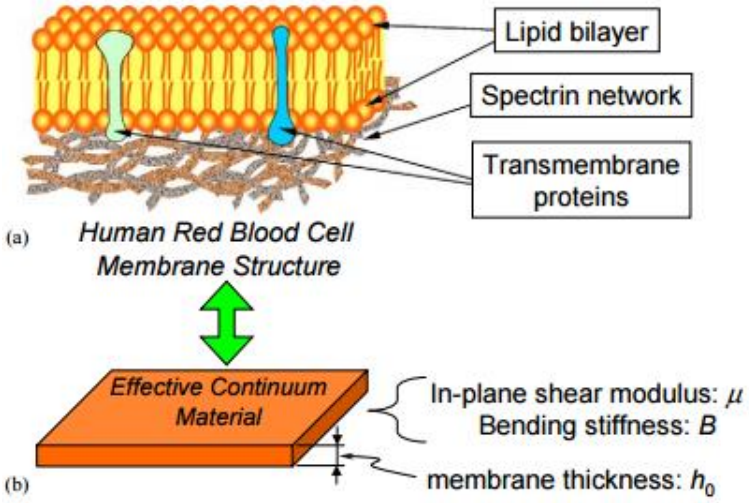

Figure 3.3. Above: the two parts of the red blood cell membrane, the bilayer and the spectrin cytoskeleton, are tethered by transmembrane proteins. Below: the combined structure can be modeled as a flexible continuum material and characterized by a shear modulus and a bending modulus [36].

There are several techniques that are used to determine the properties of red blood cell membranes. Micropipette aspiration is a technique in which a small part of the cell membrane is sucked into a micropipette. This technique attempts to isolate the membrane's mechanical properties from factors due to cell shape. Pipette tips of 1.0 to 1.5 μm are typically used for this experiment [33]. In order to calculate membrane properties, the distance which the cell

membrane is sucked in the pipette is measured as a function of suction pressure inside the pipette tube. This process is illustrated in Figure 3.4. Independent experiments using this method have yielded a shear modulus of 6-9×10^{-6} J/m^2 [37].

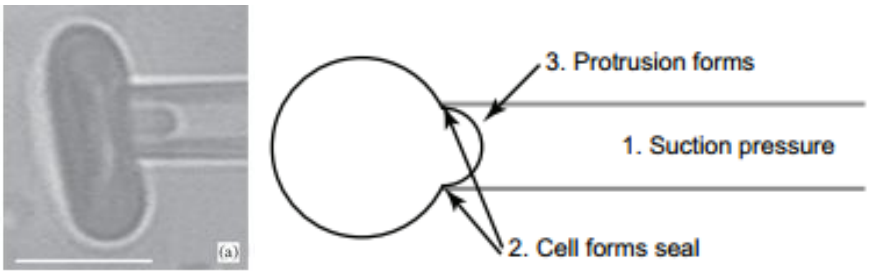

Figure 3.4. Suction pressure of the micropipette is increased in a stepwise fashion and the resulting distance the cell is sucked into the micropipette tube as a result of each pressure is measured [38].

Another method used in determining red blood cells' mechanical properties is stretching with optical tweezers. This method involves pulling the cell from either side with highly focused laser beams. High refractive index silica beads of approximately 4 μm diameter are attached to either side of the cell's membrane [36]. One bead is attached to a solid surface and the other is held in an optical trap. This optical trap is created by strong electric field gradients which attract the bead to the center of the laser beam. The use of a high refractive index bead is critical to generate the maximum stretching force possible. The trap is slowly moved and the resulting stretching force is on the order of tens to hundreds of picoNewtons [36]. The cell's response to the stretching lends insight into its mechanical properties. This setup is depicted in Figure 3.5. Property values obtained from these experiments are a shear modulus of 4-10×10^{-6} J/m^2 and a bending modulus of 2×10^{-19} J [34].

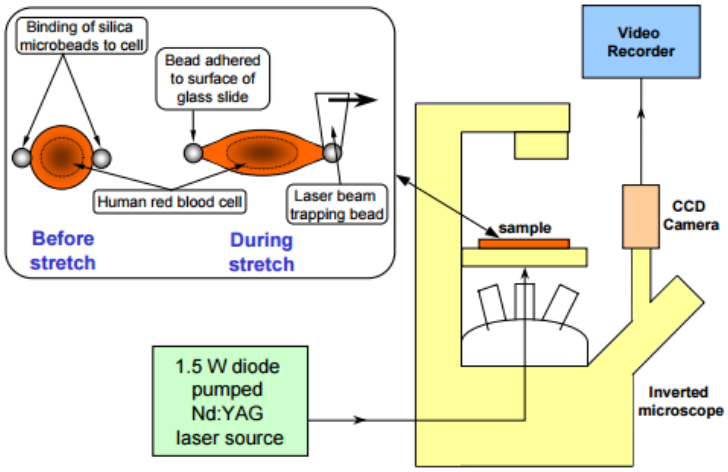

Figure 3.5. Silica microbeads are attached to either side of a red blood cell membrane. The beads are fixed in optical traps and pulled apart. The resulting deformation response is captured and analyzed [36].

3.2.4 Red Blood Cell Shape and Deformation

The membranes of red blood cells are highly flexible and do not strongly resist deformation. The internal cytoplasm provides minimal resistance to deformation as well. Assuming a body temperature of 38°C, the viscosity of the internal hemoglobin solution of a red blood cell is 30 times that of plasma and approximately equal to olive oil. The cytoplasm however is not viscoelastic thus it deforms continuously with shear. The driving force behind deformation of the cells is shear flow in the surrounding plasma. Shear rates in the larger blood vessels are relatively modest compared to in the microvasculature. At the capillary level large deformation are required for the cells to even fit through the vasculature. These deformations are achieved through shear rates as high as 1000 s^{-1} [21].

There is disagreement in the literature as to the exact shape deformed cells take on. This is because of the difficulty in determining a three-dimensional shape from two-dimensional images such as in Figure 3.6. Some researchers believe the symmetry axis of red blood cells aligns with the direction of flow [39] while others argue that it is usually perpendicular often called the "edge-on" orientation [40]. This difference is illustrated in Figure 3.7. The orientation of the

cells as they enter the capillaries appears to be a factor in the final deformed shape. Studies looking at the axial length of the deformed cells seem to indicate that the edge on configuration is more prevalent in capillaries. Given the edge-on configuration, the lower the velocity of the cells the less axisymmetric they are. Even at larger velocities the symmetry is caused by internal shifting of the hemoglobin, not a rotation of the cell. However, there are likely some cells which traverse the capillaries with their symmetry axis parallel to the flow and others with it perpendicular [41]. As seen in Figure 3.6, 4 to 5 μm vessels cause torpedo shaped cells, 6 to 9 μm vessels cause parachute shaped cells, and 10 to 12 μm vessels cause staggered slipper shaped cells. At the vessel wall, the plasma has a near zero velocity due to the no-slip condition between the plasma and the stationary endothelial cells at the capillary wall. This zero velocity ring of plasma causes cell shapes which are thought to aid oxygen transport out of the cells by bring the oxygen carrying hemoglobin closer to the vessel wall [39].

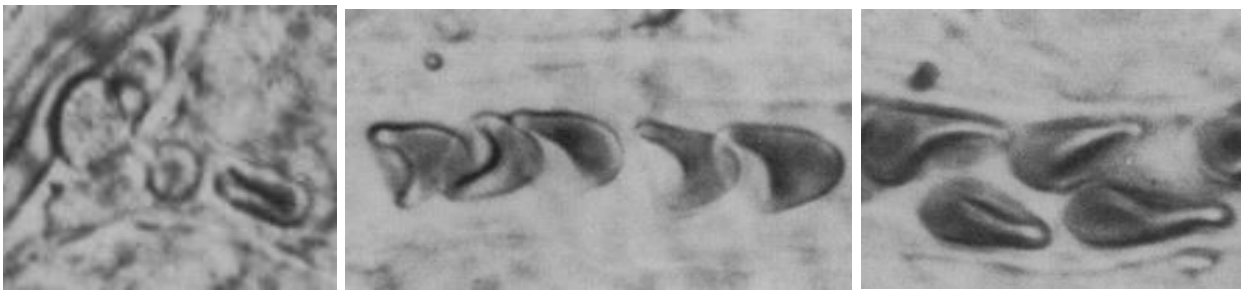

Figure 3.6. Left: red blood cell in a 4 μm capillary. The cell enters the capillary with the symmetry axis perpendicular to the flow in the "squished doughnut" configuration. Center: red blood cells in a 7 μm capillary. The orientation of the symmetry axis is ambiguous in this image. Right: red blood cells in a 12 μm capillary. The cells in this staggered configuration are referred to as "slipper" shaped cells. It starts to appear in vessels over 10 μm. [40]

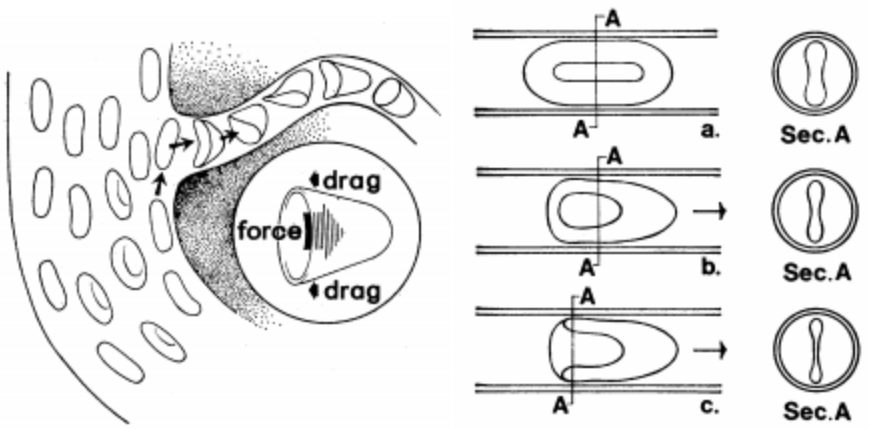

Figure 3.7. Left: cartoon illustrating the interpretation that the symmetry axis remains parallel to the flow. This is referred to as the "parachute" shape [39]. Right: cartoon illustrating the interpretation that the symmetry axis is perpendicular to the flow [40]. Notice how the photographs in Figure 3.6 could be interpreted either way.

The internal cytoplasm of the red blood cell can be assumed to be incompressible, so throughout the deformation process the cell's volume is conserved. This limits the possible shapes which a cell can take on. It has been hypothesized that in its resting state a red blood cell's shape minimizes the bending energy of its outer membrane [42]. Using this principle the cell's shape can be predicted analytically. This is illustrated in Figure 3.8.

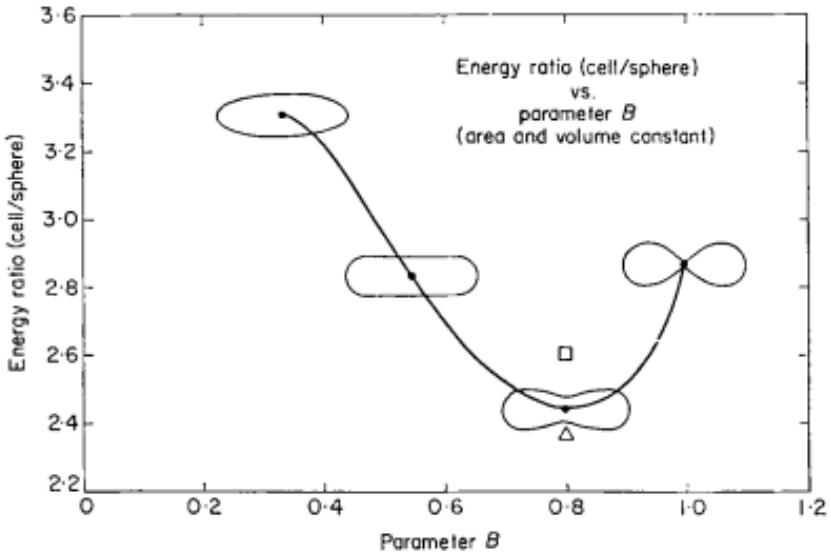

Figure 3.8. The normalized bending energy of different possible cell shapes is plotted. Notice the minimum energy state is the biconcave disc. [42]

A famous experiment was done by Canham to further verify this idea. As the osmolality of the fluid surrounding a cell changes, fluid will seep in or out of the cell. Using this principle, the volume of a red blood cell in a lab can be easily modified by adjusting the surrounding osmolality. Using the minimization of bending energy hypothesis, the resting shape of a red blood cell with various surface to volume ratios were predicted. These compared very closely with what was observed in experiment. The comparison is illustrated in Figure 3.9. Additionally, the outer membrane is thought to be area conserving. This is a more unexpected phenomenon but has held up in many different studies. The idea of minimization of membrane energy can be further extended to red blood cells in capillary flow to predict the deformed cell shapes. These models require the assumption of axis symmetry, and balance hydrostatic forces with the membrane deformations [43].

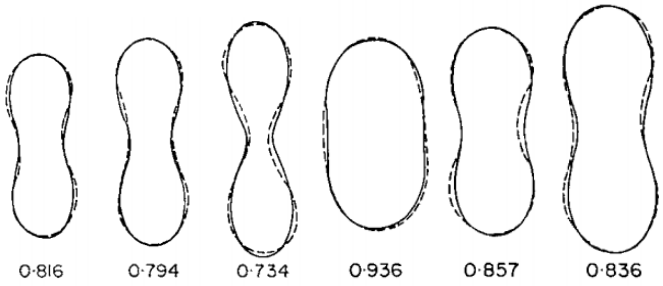

Figure 3.9. Cells placed in mediums with different osmolality exhibit different shapes. The number below each cell is its sphericity index, a dimentionless parameter ranging from 0 to 1 where 1 is a perfect sphere. The dotted line is the shape observed in experiment while the solid line is the shape predicted by minimizing the bending energy for the particular surface area to volume ratio. [42]

3.3 Capillary Model Description and Validation

3.3.1 Past Methods for RBC Modeling

Early models of blood capillaries focused on a simplified handling of red blood cells. For example, the Krogh model described the transport of oxygen from capillaries into tissue without considering individual red blood cells—that is the substance in the capillaries was taken as a

uniform fluid [44]. Other models relaxed this assumption by modeling red blood cells as perfect cylinders or spheres inside the capillaries. There have also been several efforts to analytically describe the deformed shape of red blood cells in capillaries [30, 41, 44-46]. Many of these models relied upon lubrication theory for the handling of the hydrodynamic effects.

With the advent of computational fluid dynamics, there have been several models of blood flow which resolve the entire blood vessel and red blood cell system [47, 48]. The plasma and internal red blood cell fluids are typically resolved using the incompressible Navier-Stokes or the Lattice-Boltzmann method. The red blood cell membrane is typically resolved using the finite element method (FEM) or a similar method to resolve the structure. The fluid and membrane models are often coupled using the immersed boundary method (IBM).

These computational models have appropriate uses, but for many applications they have two major drawbacks. First, these models can be computationally intensive. This is because both the fluid and the structure governing equations must be solved and then the results must be coupled. Secondly and more importantly, the red blood cell membrane is a very complex non-linear, anisotropic material which is not currently fully understood [32, 34]. This prohibits accurate resolution of the deformation of the membrane structure. For these two reasons, a lower order model may be desired. The present work describes a method for modeling a human blood capillary with red blood cells which is computationally undemanding, and contains accurate handling of the red blood cell membranes—it is called the Fixed-shape Deformed RBC Model.

3.3.2 Fixed-shape Deformed RBC Model

Red blood cells undergo large deformations as they enter capillaries from the arterioles. However, in a constant diameter capillary moving at a fixed velocity, a red blood cell's shape

should reach a fixed shape. This shape is a result of an equilibrium being reached between the plasma fluid forces and RBC membrane stress. It is hypothesized that an accurate capillary model can be constructed using fixed shapes for red blood cells assuming a constant diameter capillary and a fixed blood flow velocity. The biggest challenge for this method is determining what shape the deformed red blood cells adopt. A variety of methods were tested to generate the deformed red blood cell shapes including using revolved polynomial shapes, analytical models, and three dimensional reconstruction of optical images. A sample of each method is shown in Figure 3.10.

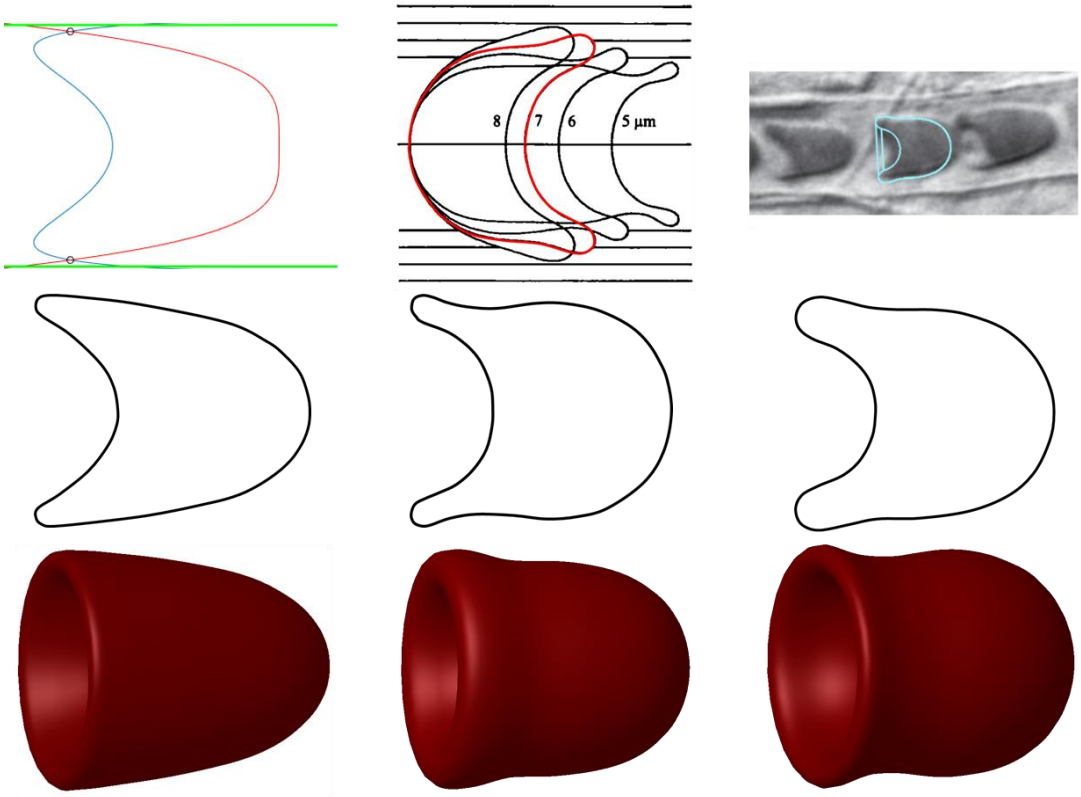

Figure 3.10. Left: polynomials were used to generate the membrane curvature and then the profile was revolved around the center axis. Center: shape was taken from solution to Secomb's analytical model using lubrication theory and minimization of membrane stress [46]. Right: cell profile was lifted from several optical images and revolved around the center axis [39, 40, 49].

The metrics considered during shape generation were cell volume, cell surface area, and radial diameter. All shapes have a surface area of 134 ± 4 μm^2 and volume of about 94 ± 1 μm^3. Each

deformed shape generated is specific to a particular capillary diameter and flow velocity. The axial cell diameter was determined based on the appropriate plasma layer thickness which is discussed further in section 3.3.5. Validation of this method to generate deformed red blood cell shapes is examined in section 3.3.7.

3.3.3 Capillary Hematocrit and the Fahraeus Effect

When studying capillary blood flow, it becomes necessary to specify between the hematocrit in capillaries versus the hematocrit in the rest of the body. The hematocrit in capillaries is lower than the hematocrit in the blood entering the capillaries because the mean plasma velocity is lower than the mean red blood cell velocity. This phenomenon is called the Fahraeus effect [50]. The hematocrit in capillaries is referred to as the "tube hematocrit" or H_T, and the hematocrit of the blood exiting into larger vessels is called the "discharge hematocrit" or H_D. In typical biological and medical discourse, the term "hematocrit" refers to discharge hematocrit. This was the hematocrit mentioned in section 3.1.2. The tube hematocrit in capillaries is a local and unusual decrease from the hematocrit everywhere else in the body. Mathematical determination of the capillary hematocrit, H_T, will be further discussed in the following section.

3.3.4 Capillary Model Parameter Definition

For clarity, the parameters in the present model are laid out in three groups—the capillary parameters (Figure 3.11), the red blood cell parameters (Figure 3.12), and the dynamics parameters (Figure 3.13). In each figure, a longitudinal slice of a capillary is shown where the capillary wall is depicted by bold black lines, and two deformed red blood cells represent a long series of consecutive cells.

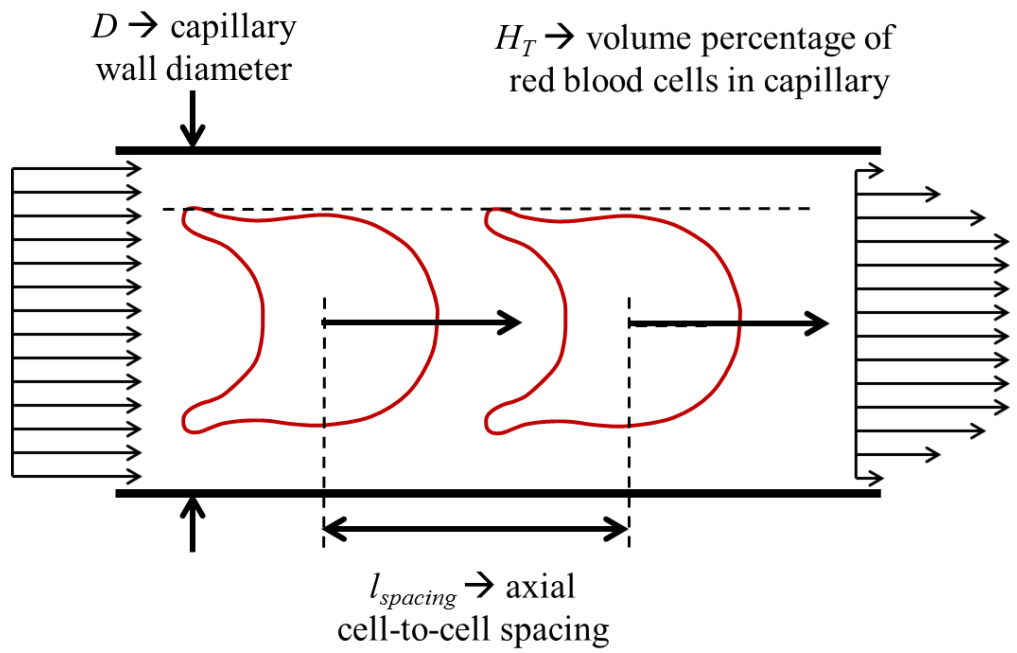

Figure 3.11. The three parameters defining the capillary portion of the system are depicted. The axial cell-to-cell spacing is a direct result of the capillary diameter and the tube hematocrit as shown by equation 3.2.

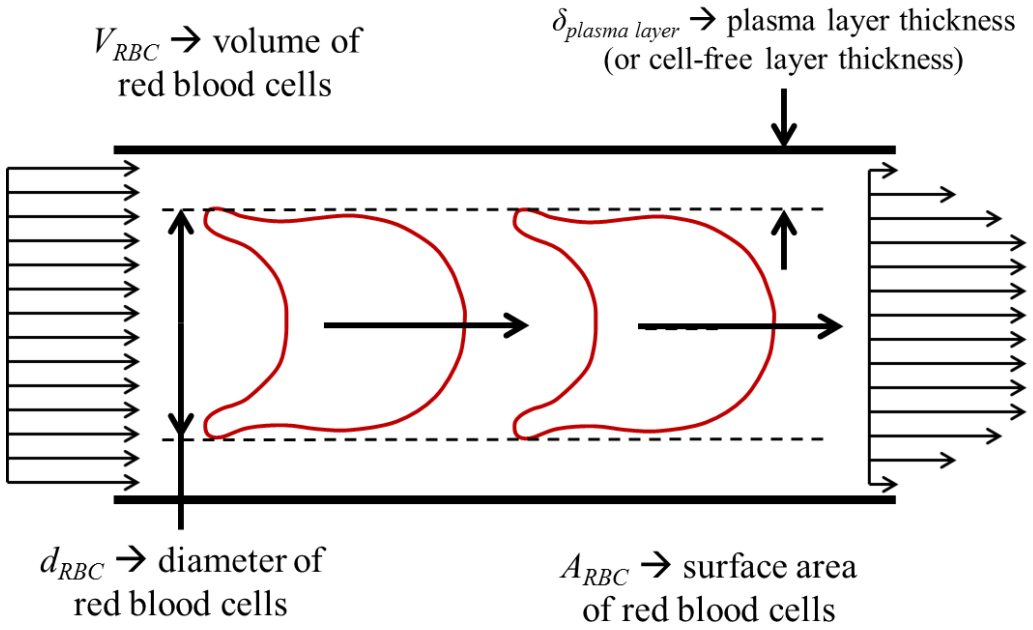

Figure 3.12. The deformation of a red blood cell can be accurately defined by its volume, surface area, and plasma layer thickness. The exact shape and curvature have a relatively small effect on the hydrodynamics of the system.

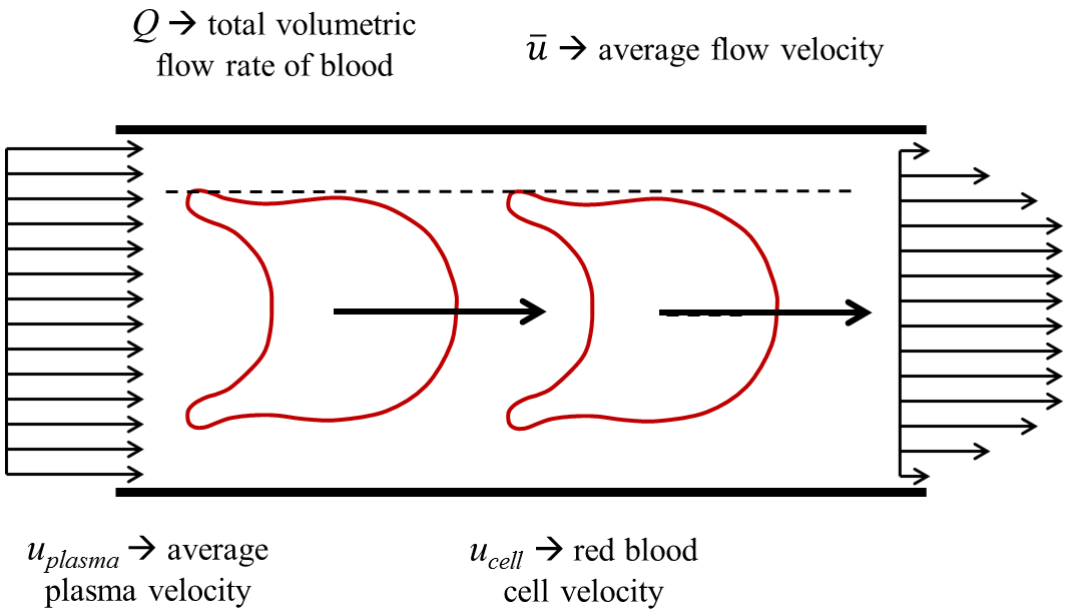

Figure 3.13. The relative velocity of the cells and plasma is determined by the internal hydrodynamics of the system. The average velocity and volume flowrate of the system are functions of the plasma and red blood cell velocities.

The three independent variables in the system are the capillary diameter, the average flow velocity, and the discharge hematocrit. These parameters can be varied within representative physiological ranges for use in the present model. The internal hydrodynamic forces of the system determine the plasma layer thickness and the relative cell velocity to plasma velocity ratio. The spacing of the cells, $l_{spacing}$, is determined by,

$$l_{spacing} = \frac{V_{RBC}}{\pi \left(\frac{D}{2}\right)^2 H_T} \tag{3.2}$$

where V_{RBC} is the volume of the red blood cells—typically around 94 μm^3—D is the capillary diameter, and H_T is the tube hematocrit determined by,

$$H_T = H_D \frac{\bar{u}}{u_{cell}} \tag{3.3}$$

where H_D is the discharge hematocrit, u_{cell} is the red blood cell velocity, and $\bar{u}$ is the average flow velocity determined by,

$$\bar{u} = u_{cell}H_T + u_{plasma}(1 - H_T) \quad 3.4$$

where u_{plasma} is the average velocity of the plasma integrated over a cross section of the capillary. u_{plasma} will always be less than u_{cell} because the cells migrate towards the center, faster regions of the flow. The total volume flow rate is given by,

$$Q = \bar{u}\, A_{capillary} \quad 3.5$$

where $A_{capillary}$ is the cross sectional area of the capillary. The volumetric flow rate can be used to find an apparent viscosity of the capillary flow,

$$\mu_{app} = \frac{\Delta P}{l_{spacing}} \frac{\pi D^4}{128\, Q} \quad 3.6$$

where $\Delta P/l_{spacing}$ is the axial pressure drop across a red blood cell. This is not a true viscosity—instead, Poiseuille's Law has been solved for the viscosity to generate a parameter representing viscosity in the two-phase, capillary flow [51, 52].

3.3.5 Plasma Layer Thickness Determination

The plasma layer thickness is a critical parameter governing the hydrodynamics in the capillary. In the present model, the plasma layer thickness is set when the deformed RBC shape is generated. In order for the model to appropriately reflect reality, the plasma layer thickness must be correct. Several experiments from the literature were examined and a correlation based on the capillary Reynolds number was established. Experimental data with a log fit is shown in Figure 3.14, and the correlation along with the non-dimensionalized data is shown in Figure 3.15.

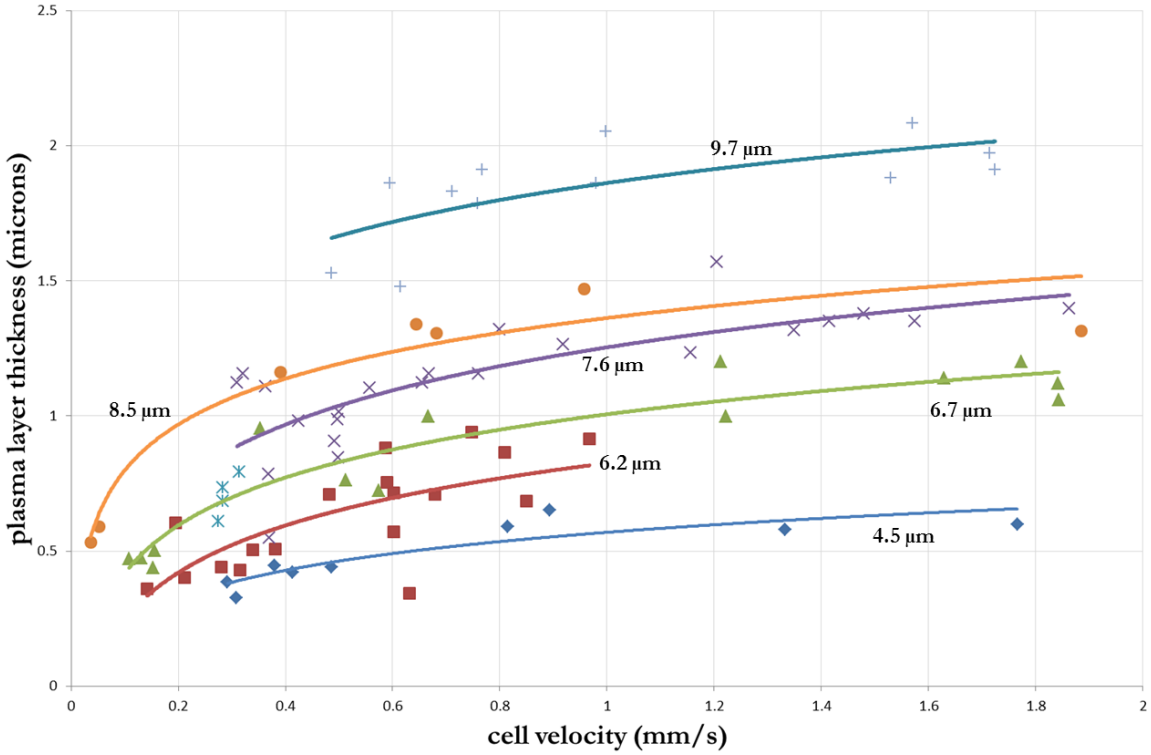

Figure 3.14. Experimentally observed plasma layer thickness data [53] is plotted versus cell velocity for six different capillary diameters. The fit lines were generated using logistic regression.

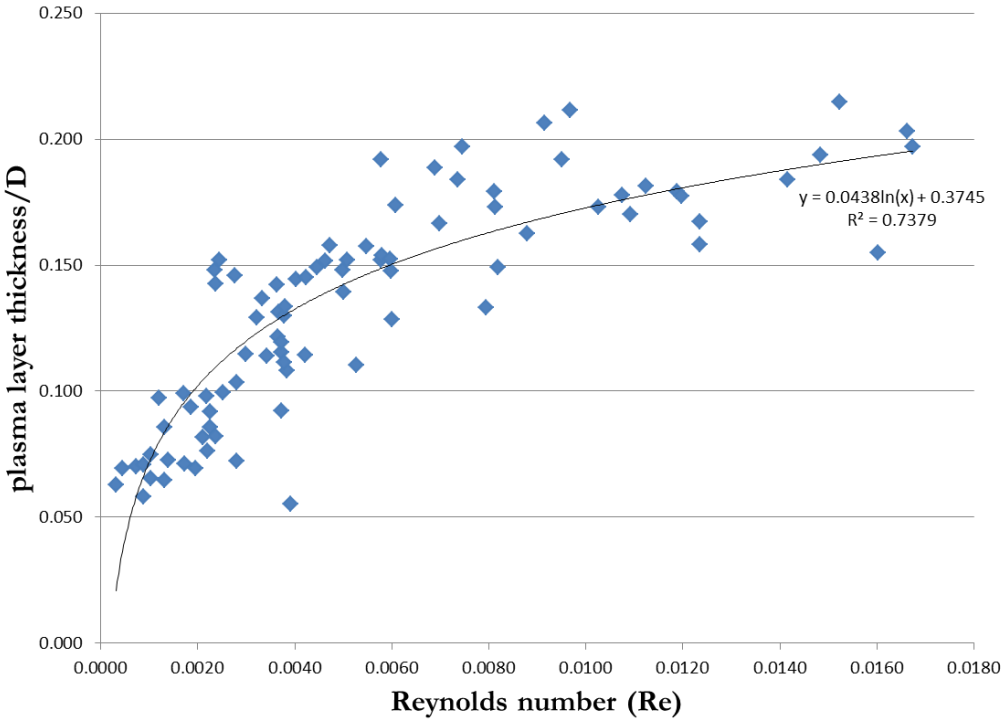

Figure 3.15. Non-dimensionalized plasma layer thickness data from Figure 3.14 plotted versus Reynolds number. The final correlation used to determine the plasma layer thickness is only a function of Reynolds number.

Equations 3.7 and 3.8 give the final form of the plasma layer thickness correlation.

$$\delta^*_{plasma} = \frac{\delta_{plasma}}{D} = 0.044\, ln(Re) + 0.37 \tag{3.7}$$

$$Re = \frac{\rho_{plasma}\, \overline{u}\, D}{\mu_{plasma}} \tag{3.8}$$

This is a novel correlation developed in the present work using existing experimental data from the literature.

3.3.6 Capillary Model Setup

The present model generates pressure and velocity fields in the plasma fluid domain such that any desired heat or mass transfer problems may be explored in the capillary system. Several simulations with varying parameters were run to validate the model. In each simulation, five deformed red blood cells were placed in plasma flow approximating a long series of cells. The plasma field was resolved using the incompressible Navier-Stokes solver described in Chapter 2. For each simulation, the system was non-dimensionalized by the capillary diameter, L_{ref}, the mean plasma velocity, U_{ref}, and the kinematic viscosity of the plasma, ν_{ref}. The Reynolds number of the system was around 0.01 but varied based on the exact input parameters chosen. The parameters tested are shown in Table 3.1.

Table 3.1. The input parameters used for the capillary validation simulations.

Case	Capillary Diameter	Plasma Velocity	Hematocrit (H_D)
1	6.0 μm	1.0 mm/s	45%
2	7.0 μm	1.0 mm/s	36%
3	7.0 μm	2.0 mm/s	35%
4	8.0 μm	0.5 mm/s	35%
5	8.0 μm	1.0 mm/s	35%
6	9.0 μm	0.1 mm/s	33%
7	9.0 μm	1.0 mm/s	33%
8	9.0 μm	4.0 mm/s	29%
9	9.0 μm	1.0 mm/s	13%
10	10.0 μm	1.0 mm/s	26%

The boundary conditions at the fluid-solid interfaces were enforced by the immersed boundary method described in Chapter 2 [17]. These interfaces included both the capillary wall and the red blood cell membranes (Figure 3.16 and Figure 3.17). The cells remain in a fixed, deformed shape and translated axially based on the pressure and shear forces of the plasma on each cell. These forces were integrated over the surface of each cell every time step. The resulting force was used to find the acceleration which was integrated in time to find the cell position at the next time step. The integration error was small due to the small time step required to resolve the highly viscous, low Reynolds number flow.

A structured Cartesian fluid mesh was used for maximum computational efficiency. Each simulation required approximately 2,000,000 fluid elements and 200,000 immersed boundary surface elements. The fluid elements were distributed into sixty-three blocks—organized into a 7 by 3 by 3 configuration and one processing core was used for each block. Message passing interface (MPI) was used to share information between block boundaries as described in Chapter 2. A typical simulation ran for 20,000 to 30,000 time steps at which point it reached steady state.

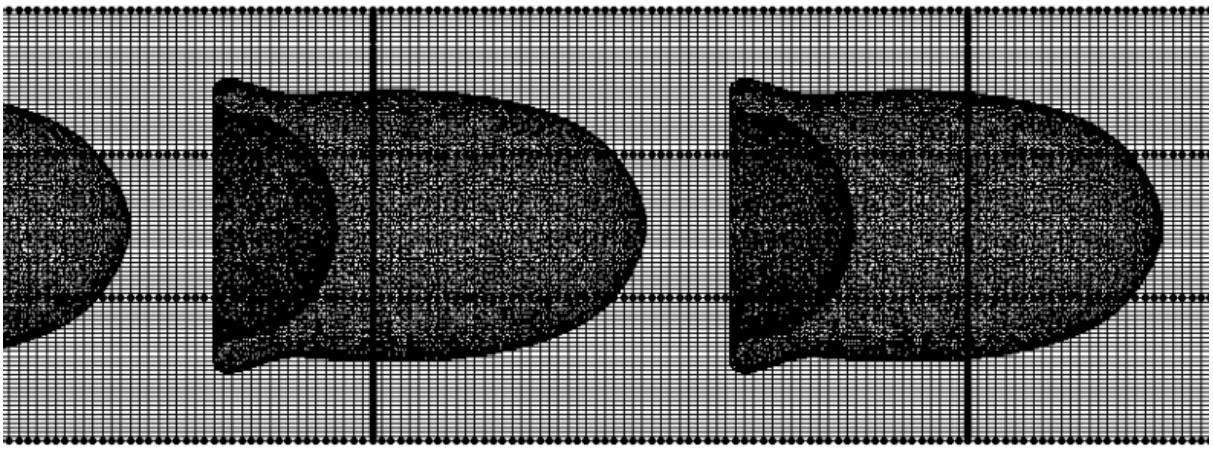

Figure 3.16. The background Cartesian fluid mesh is shown along with the red blood cells' surface meshes. The surface meshes define the IBM fluid-solid interfaces. The red blood cells shown here correspond to deformation within a 7 μm diameter capillary.

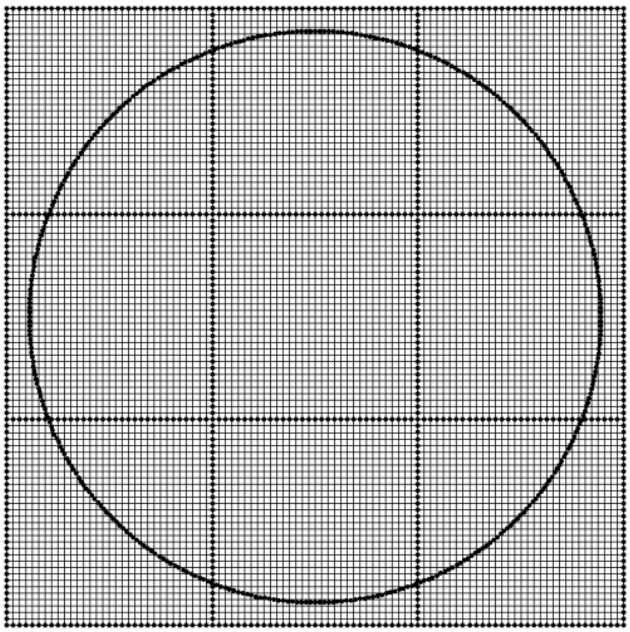

Figure 3.17. Looking axially into the capillary cylinder. The background Cartesian mesh as well as the surface mesh defining the capillary wall are visible. The red blood cell meshes are hidden for visualization purposes, but lie inside the center of the capillary.

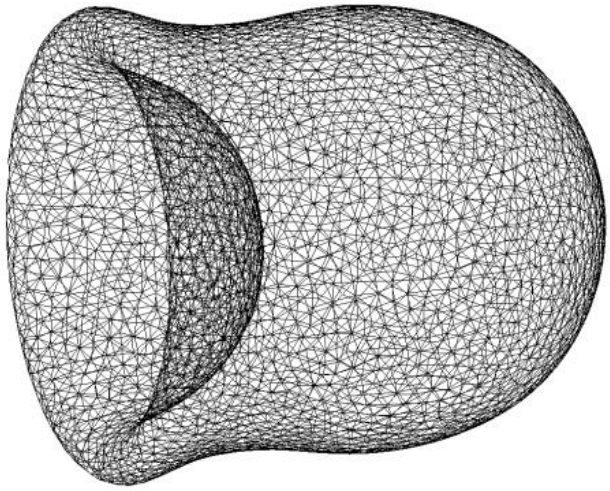

Figure 3.18. Surface mesh of a red blood cell which has been deformed characteristically of a cell entering a 9 μm diameter capillary. When using the immersed boundary method, fluid-solid interfaces are defined by edge connected vertices as shown.

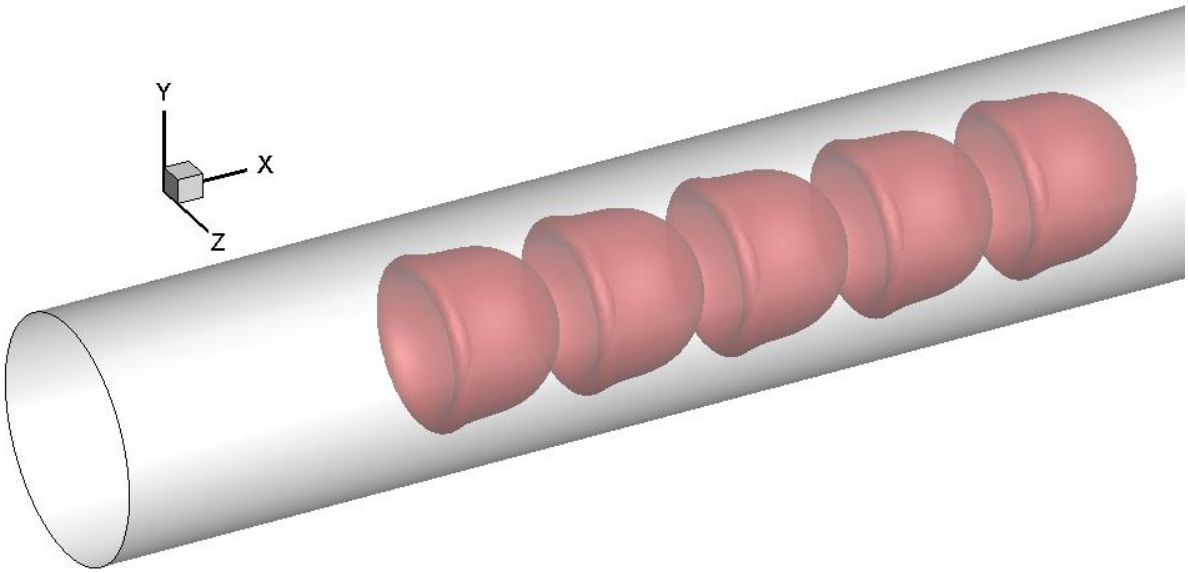

Figure 3.19. Surface mesh location of both the cells and the capillary wall. The plasma flow enters from the left, and propels the cells axially down the tube.

3.3.7 Capillary Model Results and Validation

Once the average axial velocity of the red blood cells became constant, data was collected for validation of the model. Figure 3.20 and Figure 3.21 show the cell force and cell velocity data for a characteristic simulation run. The cells are restricted from moving for the first 3000 time steps

to allow the flow to fully develop first. Once a steady cell velocity was reached, the force and acceleration of each of the cells approached zero.

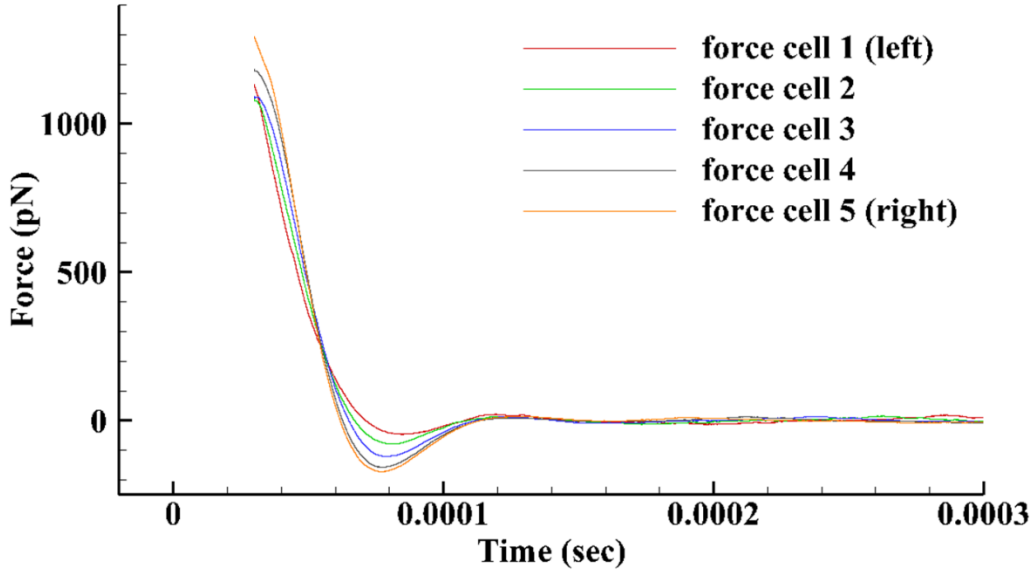

Figure 3.20. The fluid force on the red blood cells is maximum when the cells are initially stationary. As they approach a steady state velocity, the force approaches zero.

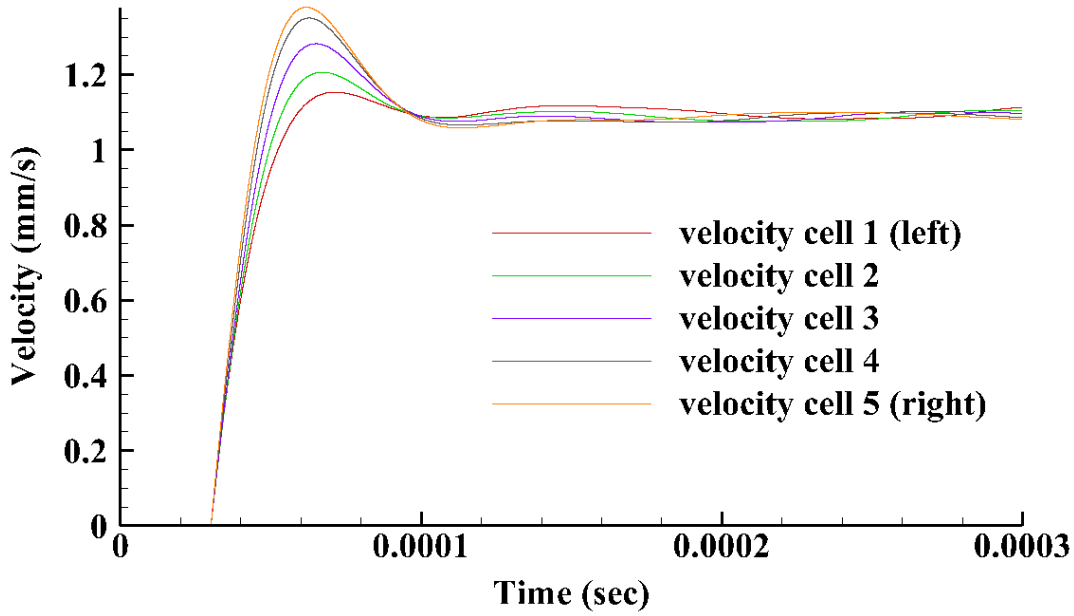

Figure 3.21. The axial velocity of the red blood cells from a typical simulation is plotted over time. The average velocity reaches a steady state, and the u_{cell} value can be read off the plot.

Since the flow was dominated by viscous forces, the system reached a steady state very quickly. The cells did not have a chance to exit the domain. The first and last cells were used as dummies,

but the three inner cells behaved as if they were in a long series of cells representative of physiological conditions. u-velocity and pressure contours are plotted in Figure 3.24, Figure 3.25, and Figure 3.26 to provide a qualitative understanding of the flow patterns around the red blood cells. When the relative velocity of the plasma with respect to the red blood cells is plotted, recirculation flow patterns emerge in the wake of the cells. This can be seen in Figure 3.23. The pocket of plasma in between consecutive red blood cells is called bolus flow. Bolus motion of intracellular plasma in recirculation patterns has been observed in experimental investigations of capillary blood flow [54].

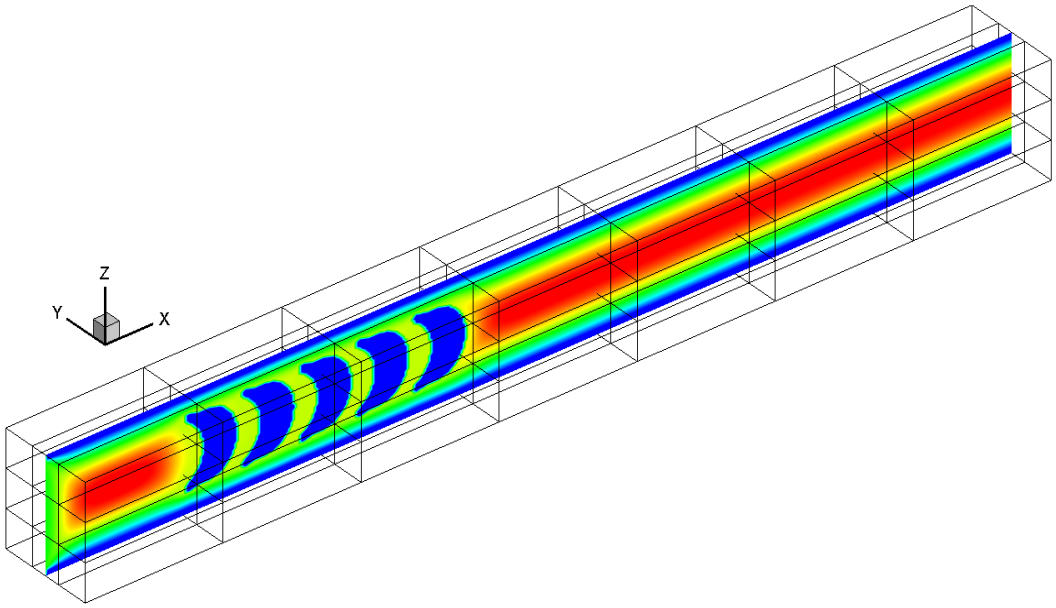

Figure 3.22. Shown is a slice of u-velocity contours in the context of the Cartesian mesh. The outlines of the 63 blocks are visible. The flow travels in the positive x direction. Because of the viscous dominated flow, a parabolic profile quickly develops after the inlet as well as in the space beyond the cells.

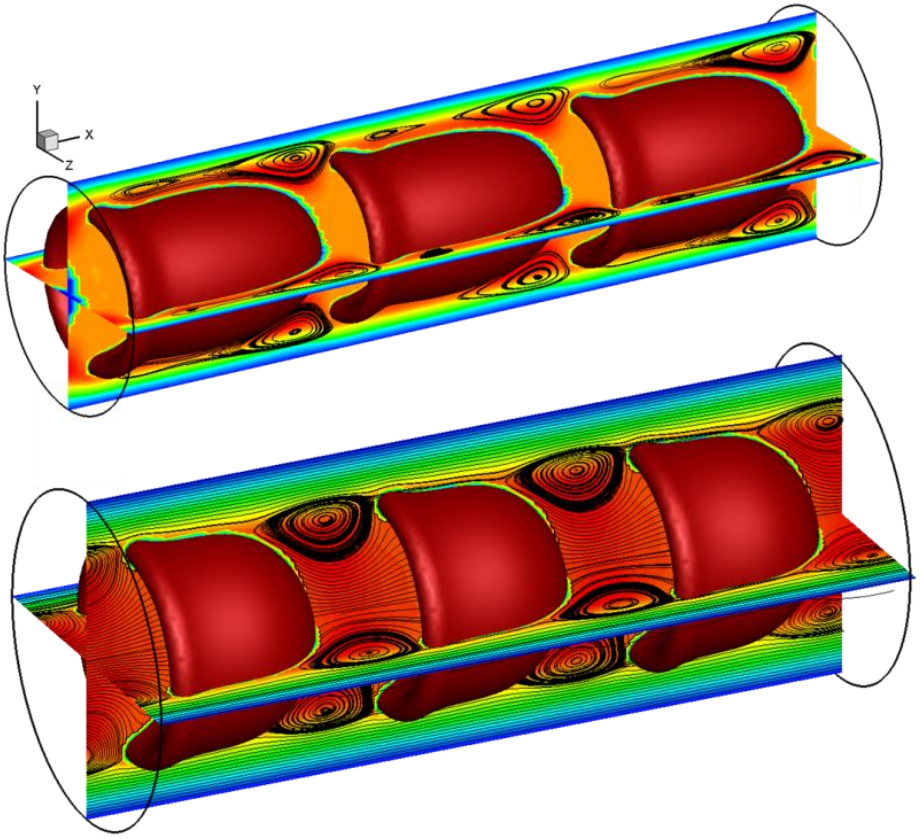

Figure 3.23. The cell velocity is subtracted from the plasma velocity field to get the relative plasma velocity. Streamlines in this relative velocity field reveal recirculation zones in the wake of the red blood cells. The top image is a 7 μm diameter capillary with a mean flow velocity of 2 mm/s. The bottom image is a 9 μm diameter capillary with a mean flow of 1 mm/s.

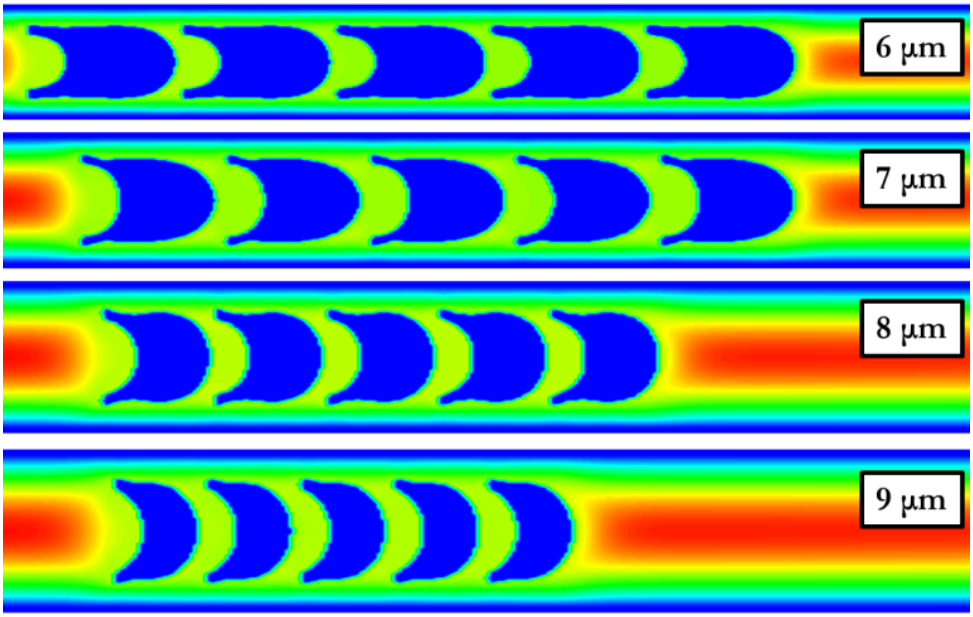

Figure 3.24. A qualitative comparison of u-velocity contours for four different capillary diameters. The surface and volume of the cells are constant across all four simulations and the plasma layer thicknesses are determined from the Reynolds number and calculated by equation 6.

The axial pressure drop across each cell is averaged for the calculation of apparent viscosity. Pressure is relatively constant in each cross-section, and the pressure drop across each cell is relatively constant as well. This can be seen in Figure 3.25 and Figure 3.26. In order to calculate apparent viscosity the pressure drop across the middle three cells was averaged and substituted into equation 3.6 along with the mean volume flowrate. The resulting apparent viscosity can be non-dimensionalized by the plasma viscosity to achieve relative apparent viscosity. This is a common parameter studied in capillary blood flow.

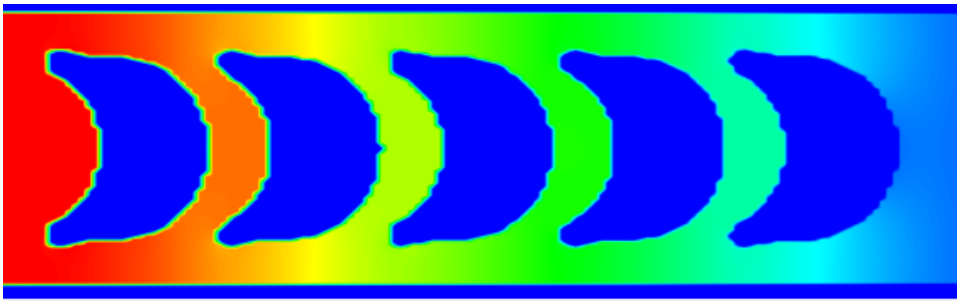

Figure 3.25. A qualitative depiction of streamwise pressure drop for a 9 μm diameter capillary. The pressure drop is used to calculate the relative apparent viscosity of the system.

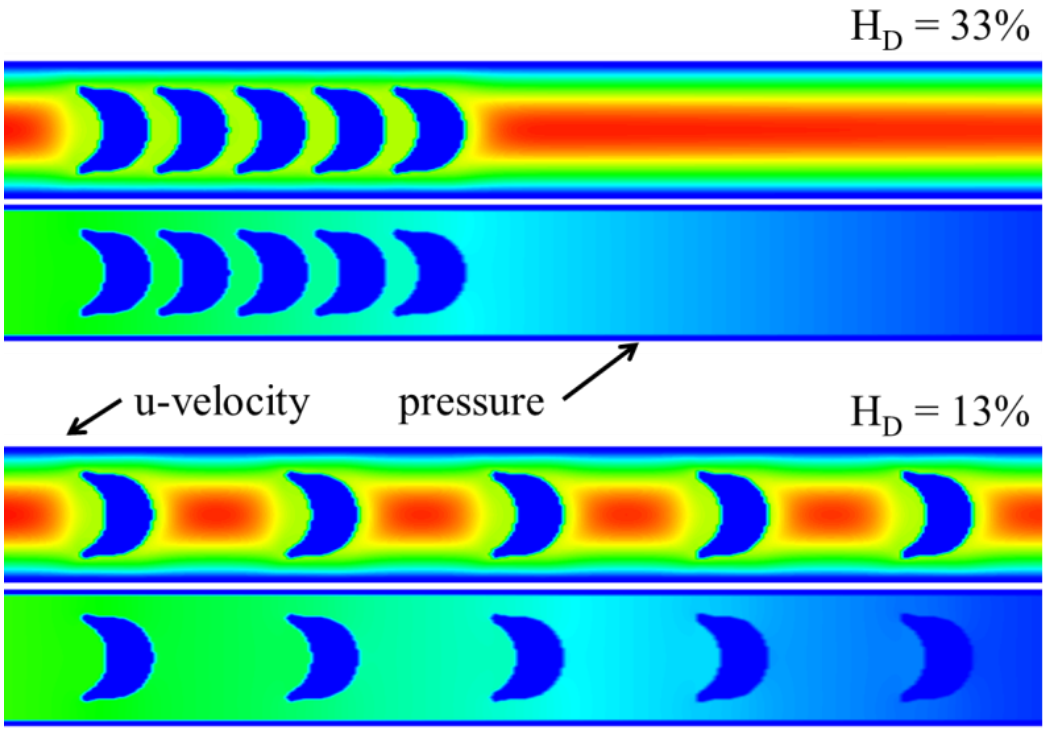

Figure 3.26. Pressure and velocity contours are depicted for two hematocrit values. The diameter of both capillaries is 9 μm and the average plasma velocity is 1.0 mm/s.

Figure 3.27 and Figure 3.28 compare the data retrieved from the present model with existing, well established experimental trends for hematocrit ratio and relative apparent viscosity in narrow glass tubes [49, 52, 55, 56]. Narrow glass tubes are commonly used *in vitro* analogues for human capillaries. Both the trends and magnitudes of hematocrit ratio and apparent viscosity compare favorably to experimental data. Uncertainty can be incurred in the experimental data from measurement challenges and procedural uncertainty. Uncertainty can be incurred in the present computational model from numerical error and uncertainty in the plasma layer thickness input. Due to the low Reynolds number flow and the refined mesh required for the immersed boundary method, numerical error is likely negligible compared to the uncertainty in the plasma layer thickness data used to generate equation 6. Since real physiological capillary systems have a high degree of variability in cell size and membrane properties, the results of the present model are quite good.

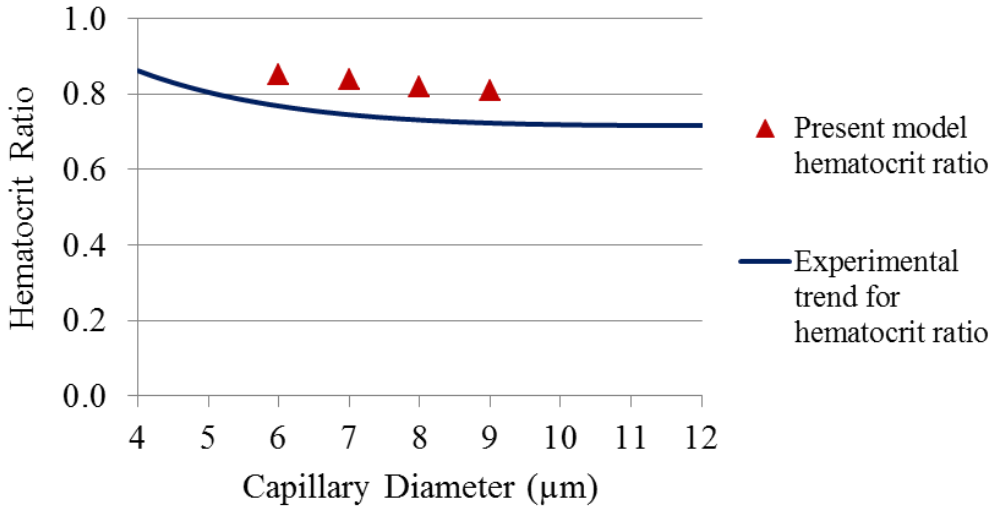

Figure 3.27. The hematocrit ratio (H_T/H_D) is plotted for capillaries of different diameters along with an experimentally determined relationship from Pries et al., 2005 [49].

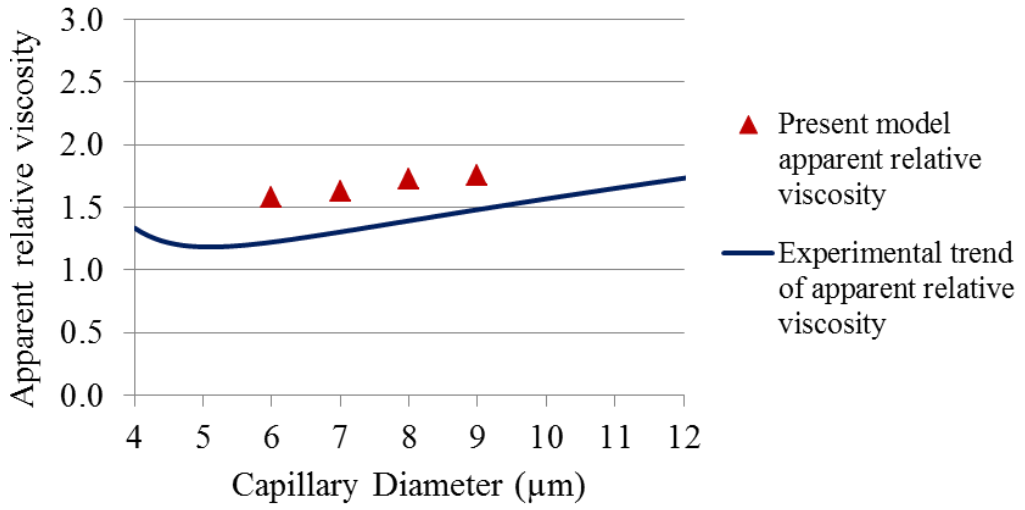

Figure 3.28. The relative apparent viscosity (v_{app}/v_{plasma}) is plotted for capillaries of different diameters along with an experimentally determined relationship from Pries et al., 2005 [49].

This *in silica* model of a capillary uses the same strategy as *in vitro* capillary models use—that is, it approximates the capillary as a straight tube. A possible improvement to the present computational capillary model would be to account for the differences between *in vitro* and *in vivo* flow. Several researchers have investigated the presence of an endothelial surface layer on the inside of capillary walls which is not captured *in vitro*. One method of incorporating this into the present model would be to use a reduced "effective" capillary diameter. Another possibility would be to include a thin porous layer near the capillary wall [49, 52, 57]. The fundamental setup and procedure of the simulations would remain the same.

4. Bacteria Modeling

Since the objective of this work is to examine the transport of bacteria in tumor capillaries, a computational model of bacteria must be developed. *Escherichia coli*, a model gram-negative strain of bacteria, is among the most studied and well understood microorganisms. Their process of locomotion has been thoroughly characterized. Phylogenetically, they are closely related to *Salmonella* Typhimurium which have shown promise in cancer therapy studies, as discussed in Chapter 1 [10]. For these reasons, *E. coli* will be the bacteria species computationally modeled in the present work. This chapter will introduce biological characteristics of *E. coli* focusing especially on the propulsive organelle, the flagella, as well as discuss swimming motility. Then a computational model of a single *E. coli* bacterium which can be incorporated into the previously developed capillary model will be described.

4.1 Bacteria Biology

4.1.1 Introduction to *Escherichia coli*

Escherichia coli is a common species of bacteria which is found in the intestines of humans and animals. As the most well studied bacteria species, it is often used as a model organism in microbiology research. A full sequence of its genome was first published in 1997, and many but not all of its approximately 5000 genes have known functions [58, 59]. *E. coli* has a rod shaped cell body which is around 2.5 μm long and 0.8 μm in diameter. The cell is about 70 percent water and is slightly denser than water. The total cell weight is approximately 1 picogram [60]. *E. coli* bacteria reproduce rapidly with a doubling time of approximately 20 minutes in ideal conditions. Thus, given adequate nutrients a population can expand very rapidly [60].

Many but not all strains of *E. coli* possess swimming motility. Motility can provide several advantages to an organism. For example, a bacterium can search for food, correct pH, light, or favorable temperature by swimming around its environment [61]. Due to the low Reynolds number experienced by a bacterium, motility is achieved not by flapping its tail, but rather by rotating a corkscrew like propeller [62]. *E. coli* and *S.* Typhimurium form this propeller by rotating a bundle of thin helical protrusions called flagella. They are peritrichously flagellated—that is, they have 6 to 8 flagellar filaments which are evenly distributed around their cell body. Other bacteria species, however, can have one single flagellum or a flagellum on each end of their body as illustrated in Figure 4.1.

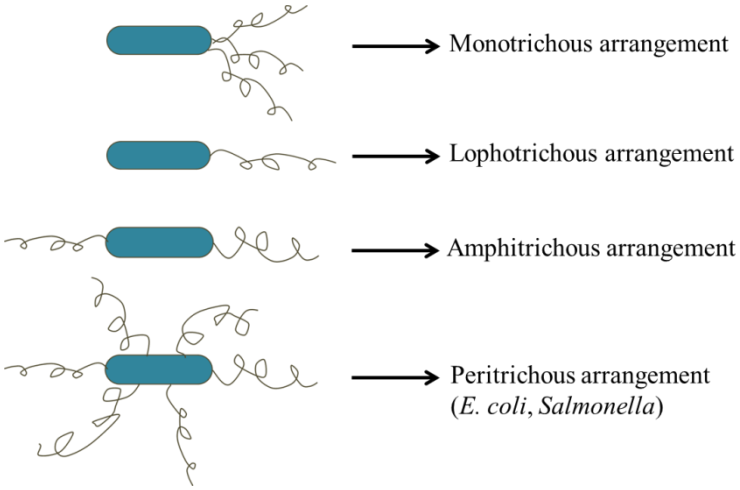

Figure 4.1. The four main flagella arraignments. *E. coli* fall under the peritrichous arraignment, meaning they have several flagella randomly distributed around their body.

Each filament is approximately 20 nm in diameter, and 5 to 10 μm long. At its base, is a rotary motor which can spin clockwise or counter clockwise. Each filament is made from 20,000 subunits of a protein called flagellin [59]. This protein gives the filament a stiffness two orders of magnitude higher than actin, a common structural protein found in eukaryotic cells. This makes the flagella quite suitable to be a propeller despite the filaments' thin diameter. The filaments have a coefficient of flexural rigidity on the order of 10^{-24} N/m^2, and a coefficient of torsional

rigidity on the order of 10^{10} N/m^2 [59]. Each filament is helical in shape with a pitch of 2.0 to 2.5 µm, and a helix diameter of 0.4 to 0.6 µm [59]. Typically, the helix is left handed however it also has a polymorphic state which is right handed. This is called the "curly" state and is activated by external torques, such as when the flagella motor reverses [63]. This polymorphic transition is essential to the unbundling of the multiple flagella allowing the bacteria to reorient itself while swimming.

4.1.2 *E. coli* Motility

The process of locomotion at the scale of a single *E. coli* bacterium has been thoroughly characterized in the literature [60, 64, 65]. *E. coli* swim by cycling between two modes of motion—a forward swimming mode called "running" and a reorientation mode called "tumbling."

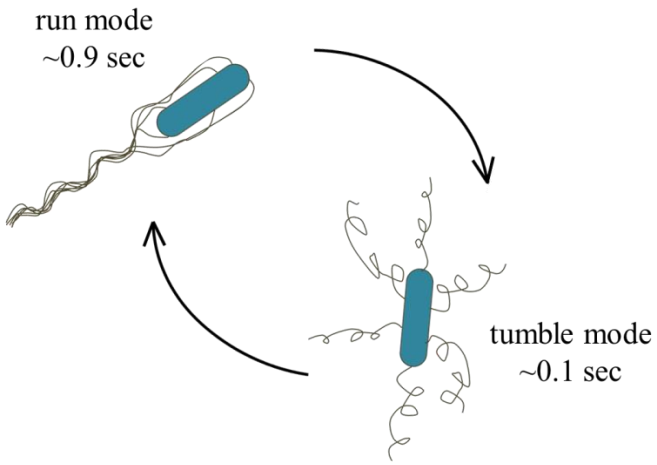

Figure 4.2. *E. coli* bacteria swim by switching back and forth between "running" and "tumbling" modes.

During the run mode, which typically last around 0.9 seconds, the bacterium's flagella motors all rotate counter clockwise causing the 6 to 8 filaments to bundle together into a corkscrew. Depending on the species and strain of bacteria, the run speed can vary from 10 µm/s to 50 µm/s.

At some point during the run, one or more flagella motors may reverse and start spinning clockwise. The reversal of the flagellar motor causes the filament to enter its curly polymorphic state. This disrupts the bundle causing the filaments to separate. Once the bundle is dispersed, a combination of Brownian motion and fluid forces causes the bacterium to reorient into a new direction. At the conclusion of the tumble, typically about 0.1 seconds later, the bacterium re-enters the run mode by resuming counter clockwise rotation of all flagella motors.

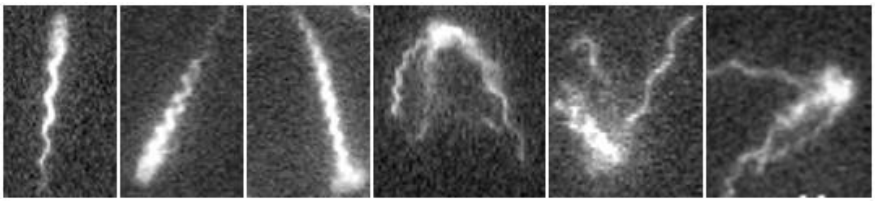

Figure 4.3. Left three: Bacteria in run mode with flagella bundled into a corkscrew. Right three: Bacteria in tumble mode. The flagella have come unbundled causing the bacteria to stop translation and reorient. Imaging of fluorescently labeled flagella was conducted by Turner et al., 2000 [66].

The tumble angle is defined as the difference between the pre-tumble and post-tumble direction of the bacteria as shown in Figure 4. 4.4.

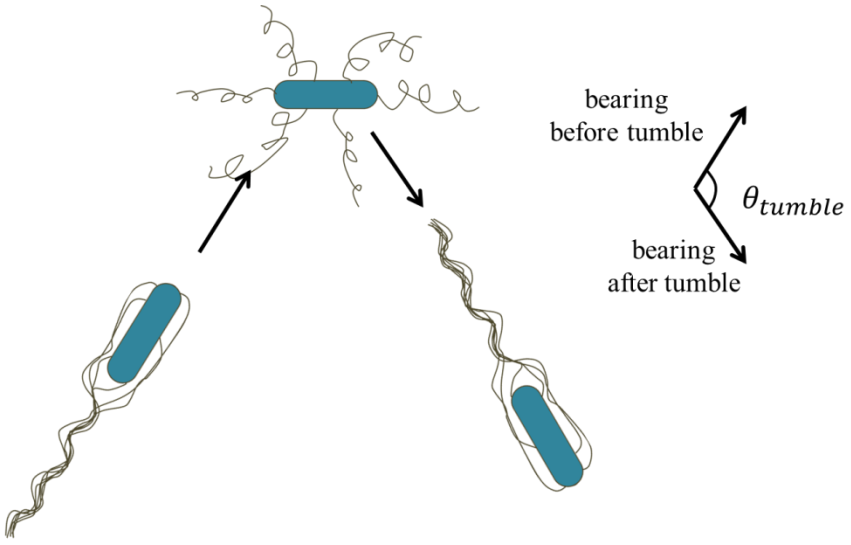

Figure 4.4. The tumble angle is calculated as the scalar angle between the final bearing and initial bearing.

Repeated cycling between running and tumbling causes the bacterium to engage in the so called random walk. Over time, the bacterium can move away from its original location however not in

an efficient manner. The displacement of the bacterium over time scales proportionally to the square root of the time interval over which the bacterium is swimming. In order to make favorable progress in a desired direction, *E. coli* engage in chemotaxis. This is the process in which a bacterium samples its environment and extends its run if it is headed in a favorable direction. Chemotaxis biases the random walk allowing the bacteria to progress in a favorable direction such as towards a desired food source or away from a toxin [61, 67].

4.2 Computational Modeling of Bacteria

4.2.1 General Bacteria Modeling Strategies

Many strategies exist for computationally modeling bacteria. The simplest method is to use a continuum approach. Since the run and tumble together form a random walk, an effective diffusivity can be calculated for a particular species of bacteria. Then a convection-diffusion equation can be solved to determine the concentration of bacteria in the domain over time. This can be solved in a two or three dimensional domain. In absence of a convective flow, it is only necessary to solve the diffusion equation. This is a low cost computationally strategy which is effective for large domains (greater than approximately 1 mm) and mid to high concentrations of bacteria. The Keller-Segel model is a classic continuum bacteria model which represents the population distribution in time based on the effects of chemotaxis, cell division, and cell death [68].

Another approach is to use an agent based strategy where bacteria are discretely modeled as infinitesimally small point-particles [69]. The location and movement of each bacterium is individually simulated unlike in the continuum model. A stochastic model can be applied to determine the run and tumble of each bacterium. Like the continuum model, an agent based

model can be solved in a two or three dimensional domain. Agent based models can be used with Navier-Stokes solvers or with only diffusion solvers if convection is negligible. Chemical species transport equations can be incorporated in order to track the concentration of chemotactic substances in the domain. Then, the run and tumble behavior of each bacteria will be modified based on the local chemoattractant gradient.

Besides continuum and agent based models, a third strategy is to fully resolve the bacteria cell in the simulation. Resolved models are appropriate for very small domains on the order of the bacteria length—5 μm to 50 μm. Most resolved models do not include the actual flagellar filaments due to their thin diameter. To date, modeling of flagella has been confined to lower order flagella models typically isolated from the bacterium body and in very small fluid domains [70-72]. The strategy used in the present work is to use an agent based model which resolves the bacteria body in the flow, but models the flagella propulsion. This is an appropriate balance of resolution and computational efficiency for a domain consisting of a section of capillary with a diameter of 8-12 μm.

4.2.2 Stochastic Motility Model for Agent Based Simulations

Bacteria motility can be reproduced *in silica* using an agent based stochastic model. The goal of the motility model is to accurately recreate the behavior of a single swimming bacterium. The implementation of this model will be briefly described in this section. In the beginning of a run, the duration of the run is randomly chosen from a log normal distribution with mean of 0.86 seconds and a standard deviation of 1.2 seconds—these experimentally determined parameters were reported for *E. coli* by Berg et al., 1972 [73].

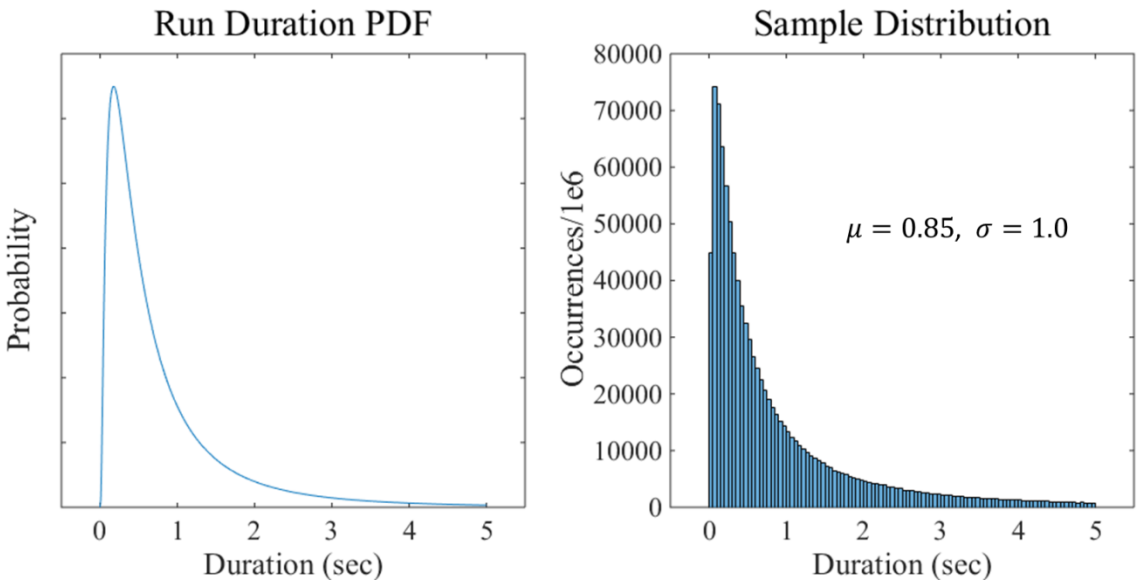

Figure 4.5. Left: log-normal probability distribution function of run durations. Right: histogram of 1 million computer generated run durations as generated by equation 4.3 using $\boldsymbol{\mu = 0.86\ sec,\ \sigma = 1.2\ sec}$. The mean and standard deviation were reported by Berg et al., 1972 [73].

Log-normally distributed random numbers with a given mean, μ, and a standard deviation, σ, can be generated from a simple set of equations. First parameters A and B are calculated,

$$A = \ln\left(\frac{\mu^2}{\sqrt{\sigma^2 + \mu^2}}\right), B = \sqrt{\ln\left(1 + \frac{\sigma^2}{\mu^2}\right)} \quad 4.1$$

Then, a normally distributed number is generated from two random numbers, r_1 and r_2, using the Box-Muller transformation shown in equation 4.2 [74]. Note that r_1 and r_2 are uniformly distributed random numbers over the open interval from 0 to 1.

$$r_{normal} = \sqrt{-2 \ln r_1}\cos(2\,\pi\, r_2) \quad 4.2$$

Lastly, $\boldsymbol{r_{normal}}$ is transformed into a log-normally distributed number with a mean of $\boldsymbol{\mu}$ and a standard deviation of $\boldsymbol{\sigma}$ by,

$$r_{log\ normal} = exp(r_{normal}\, B + A) \quad 4.3$$

After the run duration is calculated, it is divided by the time step size in order to get the number of time steps for the run.

$$n_{\Delta t,run} = round\left(\frac{t_{run}}{\Delta t}\right) \tag{4.4}$$

The quantity is rounded to obtain an integer number of time steps, however for sufficiently small time steps the error will be small—in the present work, the round off error is below 1%. For example, using a time step size of 0.001 seconds, a bacterium run of 0.7426 seconds would take 743 time steps, and the rounding error would only be 0.05%. A variable time step size may be needed if a large time step is being used. During the run phase the slip velocity is calculated by,

$$\vec{v}_{run} = |\vec{v}_{run}|\,\hat{d} \tag{4.5}$$

where $\hat{\boldsymbol{d}}$ is the bacterium's forward direction unit vector. The magnitude of the run velocity, $|\vec{\boldsymbol{v}}_{\boldsymbol{run}}|$, is a constant in the model based on the bacteria species and strain. In the present work, 20 μm/s was used. Depending on the application of the model, a variable run velocity chosen from a distribution could also be used. In a stagnant fluid, the slip velocity equals the bacterium velocity. However in moving fluid, the bacterium velocity is the local fluid velocity plus the slip velocity as illustrated in Figure 4.6.

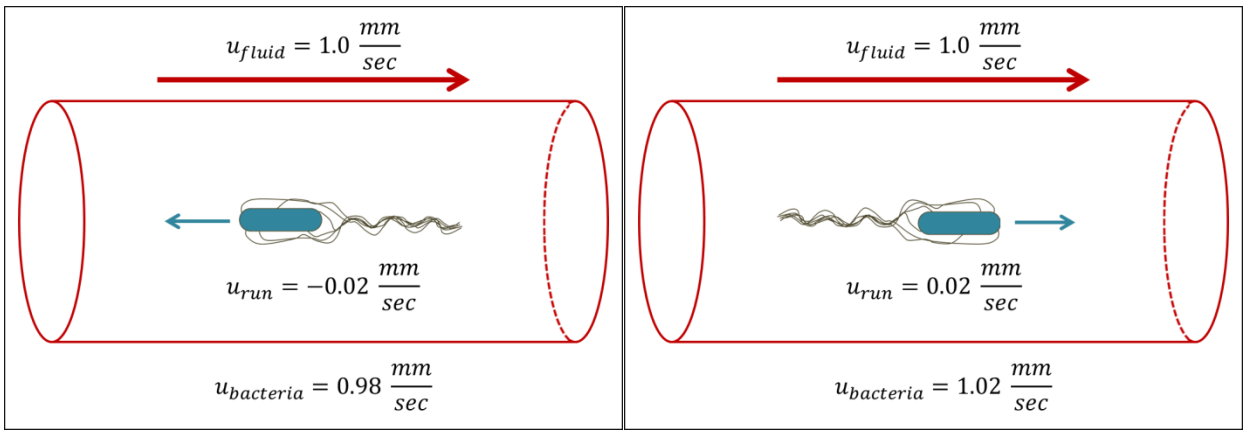

Figure 4.6. The run velocity is the slip velocity, not the absolute velocity. The vector sum of the local fluid velocity and the run velocity gives the total bacterium velocity as illustrated by the two examples above.

Upon $\boldsymbol{n_{\Delta t,run}}$ time steps passing, a tumble is initiated. At the beginning of a tumble, first a random axis about which the bacterium will rotate is chosen. This axis is restricted to be perpendicular to the forward direction vector, $\widehat{\boldsymbol{d}}$, based on the definition of the tumble angle in Figure 4.4.

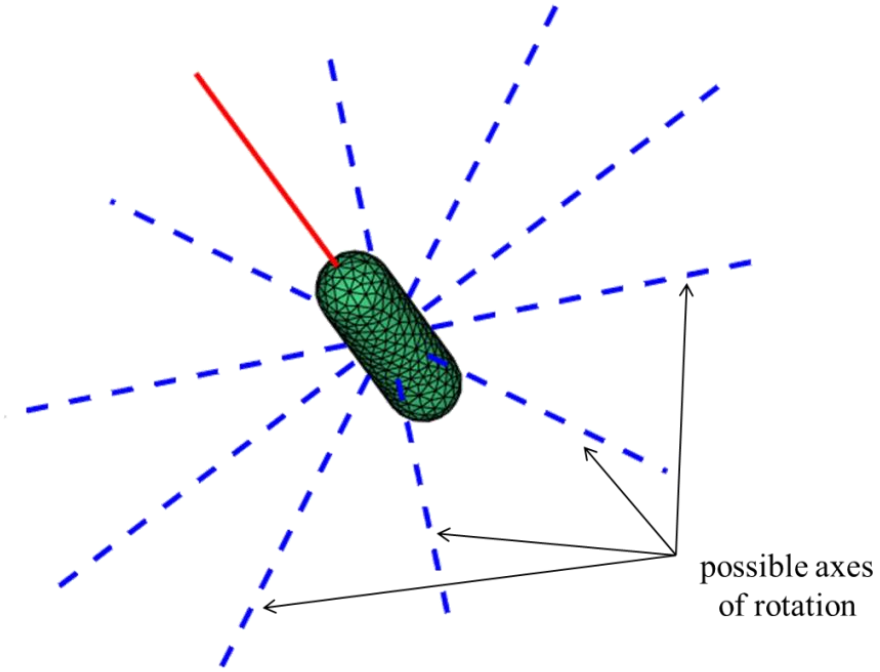

Figure 4.7. At the beginning of each tumble, an axis of rotation perpendicular to the red direction vector, $\widehat{\boldsymbol{d}}$, is randomly chosen and stored as the unit vector, $\widehat{\boldsymbol{a}}$. Ten possible axes of rotation are shown superimposed.

Second, the tumble angle or the magnitude of the angle change is randomly selected from a normal distribution using a mean of 68 degrees and a standard deviation of 36 degrees [73].

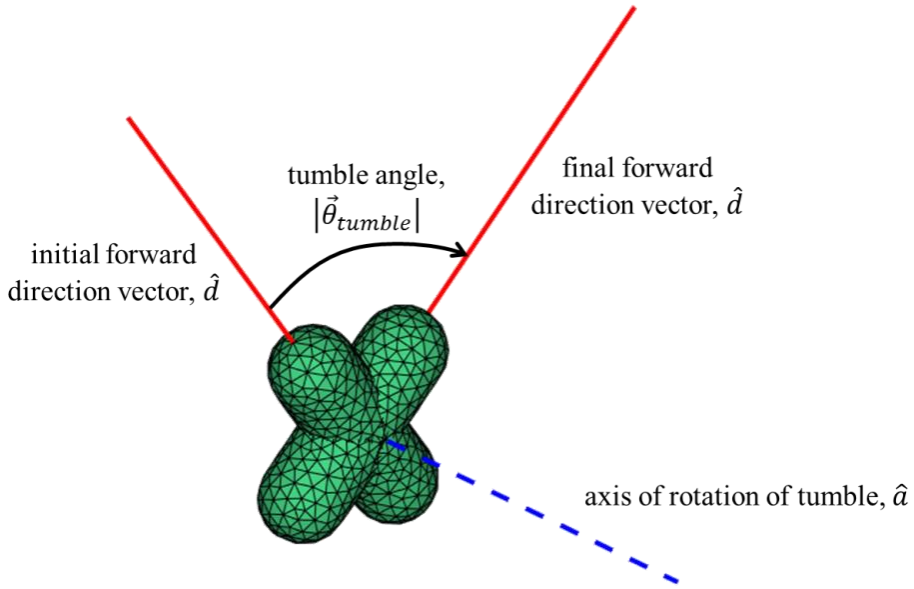

Figure 4.8. Once a tumble axis is chosen, the magnitude of the tumble angle is picked randomly from the distribution shown in Figure 4.. In the model, the bacterium pivots over the course of many time steps. After the tumble, the red direction vector is updated.

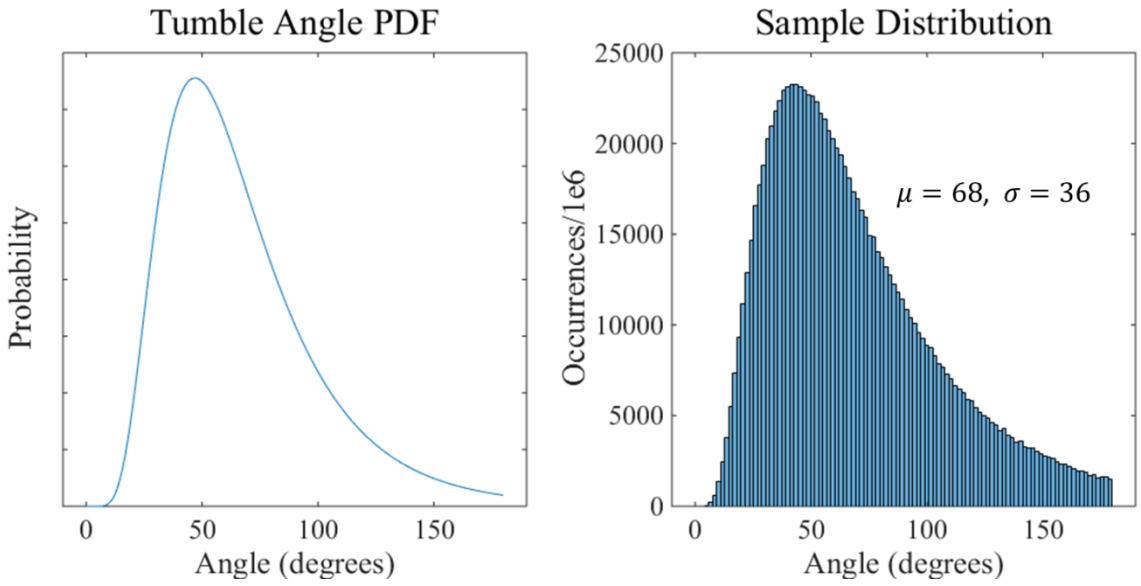

Figure 4.9. Left: log-normal probability distribution function of tumble angles. Right: histogram of 1 million computer generated tumble angles as generated by equation 4.3 using $\mu = 68°,\ \sigma = 36°$. The mean and standard deviation were reported by Berg et al., 1972 [73].

Third, an angular velocity magnitude is chosen from the distribution shown in Figure 4.10.

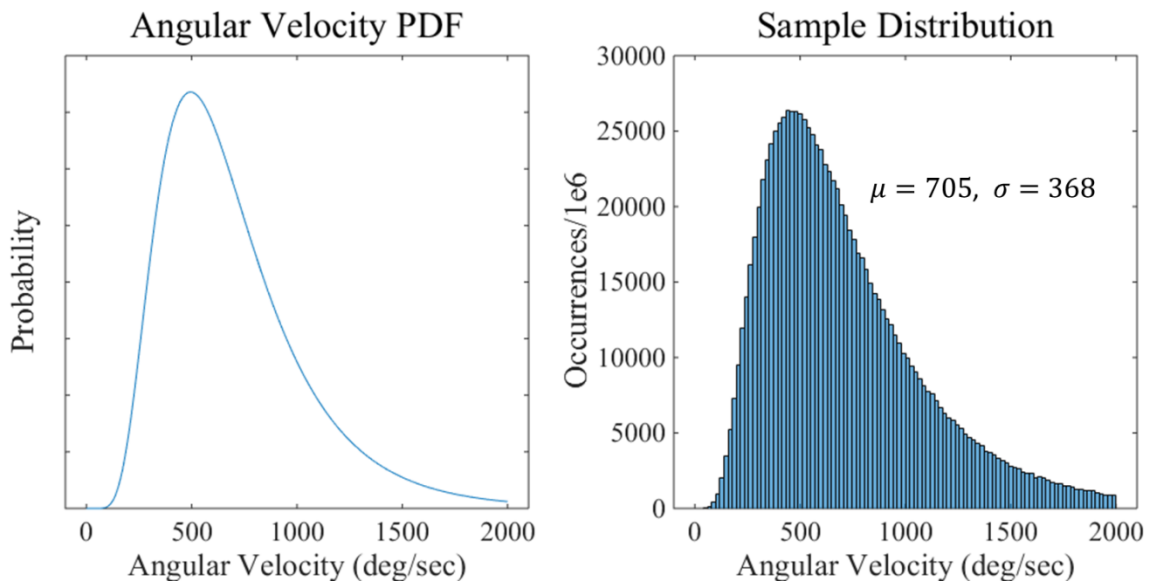

Figure 4.10. Left: log-normal probability distribution function of angular velocities. Right: histogram of 1 million computer generated tumble angular velocity magnitudes as calculated by equation 4.3 using $\boldsymbol{\mu = 706°/s,\ \sigma = 365°/s}$. The mean and standard deviation were reported by Berg et al., 1972 [73].

The duration of the tumble is calculated by solving equation 4.6 for t_{tumble}.

$$|\vec{\omega}_{tumble}| = \frac{|\Delta\vec{\theta}_{tumble}|}{t_{tumble}} \tag{4.6}$$

Once the duration of the tumble is determined, the number of time steps is calculated by,

$$n_{\Delta t,tumble} = round\left(\frac{t_{tumble}}{\Delta t}\right) \tag{4.7}$$

At each time step during the tumble, the vectoral instantaneous angular velocity is calculated by multiplying the random angular velocity magnitude by a unit vector along tumble axis generated in the beginning of the current tumble. At the conclusion of the tumble a new run begins using the updated forward direction vector and the process repeats.

The motility model can then be summarized as follows,

1. A random run duration is generated.
2. The bacterium swims forward for the duration of the run.
3. A randomly selected tumble axis, tumble angle, and angular velocity are generated.
4. The tumble duration is calculated based on the tumble angle and the angular velocity.
5. The bacterium rotates for the duration of the tumble.
6. The process repeats from step 1.

The model was implemented and tested in a large open domain without fluid interaction. Two characteristic bacterium paths are shown in Figure 4.. The model is three dimensional, so the paths depicted are planar projections of the actual path.

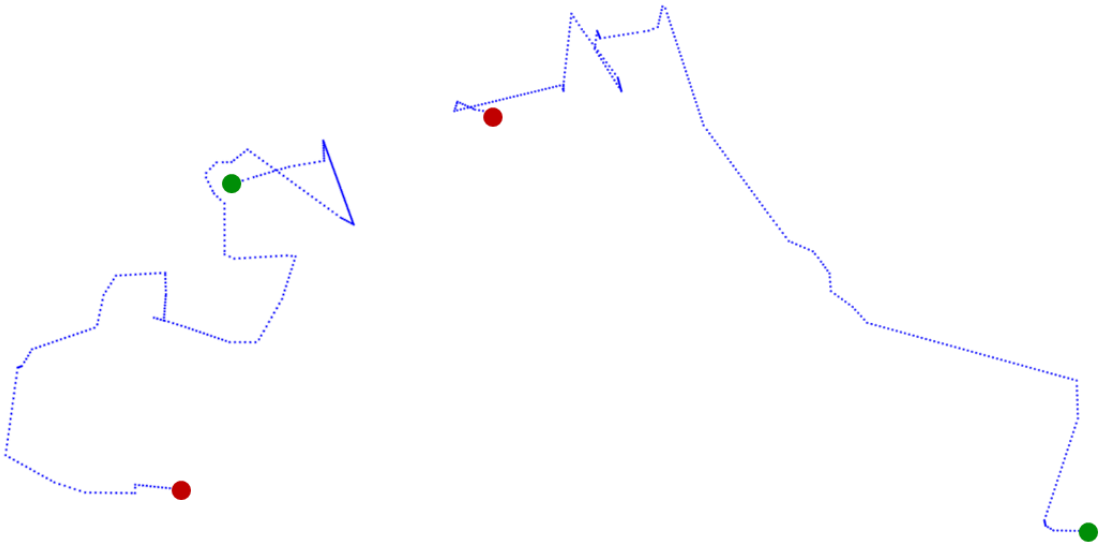

Figure 4.11. Two dimensional projections of the path of two different bacteria. The initial and final locations are denoted by the green and red dots respectively. Each simulation was run for 30 seconds. The run speed was 20 µm/s.

4.2.3 Interaction of Bacteria and Solid Objects

The behavior of a swimming bacterium when it encounters various solid surfaces has not been fully characterized in the literature. Chemical gradients [61, 67, 68], light [75], energy [76], and magnetism [77] are a few factors which are known to modify the run and tumbling cycle of certain specific bacteria species. Physical objects such as walls [78-81], porous media [82-85],

other bacteria [86], and cylindrical pipes [87-89] are known generally to affect the swimming of bacteria. However, it is not clear in all cases whether the mechanism by which these factors affect the swimming trajectory of a bacterium is mechanical, hydrodynamic, or biochemical. Understanding the mechanism of interaction is critical from a modeling standpoint—without complete characterization of a phenomenon, replication of reality *in silica* is hopeless.

In the present bacteria model, it was determined that contact with solid surfaces should not modify the run or tumble durations of a bacterium. That is, there is no communication between external contact of the membrane and the biochemical timers governing the runs and tumbles. Thus, the capillary walls and red blood cells affect the bacteria through hydrodynamic interaction only. If a bacterium hits an obstruction in the run phase, the flagellar propulsion will continue but the bacterium will remain in place. This is called an "idle" and has been observed experimentally of bacteria in porous media [84, 85]. Bacterium-solid collisions that happen are resolved using a zero coefficient of restitution (COR) assumption. Reorientation my happen as a result of contact, but that is not a tumble as strictly defined, because the flagella motors do not reverse direction.

5. Capillary Transport Simulations

This chapter will describe the procedure for running simulations using the capillary model discussed in Chapter 3 along with the bacteria model discussed in Chapter 4. In total, three categories of simulations were run—nanoparticle transport in a capillary, non-motile bacteria transport in a capillary, and motile bacteria transport in a capillary. The main interest is to compare motile bacteria transport with the other two control cases. This chapter will first describe the simulation setup and process. Then results will be shown and analyzed followed by discussion and conclusions. Lastly, possible future directions of the research will be described.

5.1 General Setup of Simulations

5.1.1 Fluid Domain Setup

Fixed capillary parameters were used for all nanoparticle and bacteria transport simulations to allow for direct comparison between the data from different runs. A 9.0 μm diameter capillary with a mean flow of 1.1 mm/s and a tube hematocrit of 20.5% were selected as characteristic of an average capillary [90]. This gave an effective Reynolds number of approximately 0.006 as calculated by equations 5.1, 5.2, and 5.3.

$$Re_{eff} = \frac{\bar{u}\, D_c}{\nu_{app}} \tag{5.1}$$

where D_c is the capillary diameter, $\bar{u}$ is the mean flow velocity as given by,

$$\bar{u} = u_c H_T + u_p(1 - H_T) \tag{5.2}$$

and ν_{app} is the apparent kinematic viscosity as given by,

$$\nu_{app} = \frac{\mu_{app}}{\rho_{bulk}} = \frac{1}{\rho_{rbc} H_T + \rho_p(1 - H_T)} \frac{\Delta P}{l_{spacing}} \frac{\pi {D_c}^4}{128\, Q} \tag{5.3}$$

A periodic fluid domain was chosen to allow for 1 to 2 second simulation times without requiring an excessively long spatial domain. To illustrate the need for a periodic framework, consider a flow where red blood cells are traveling axially through a 9 μm diameter capillary on the order of 1 mm/s. If it is desired to simulate 1 second of real time in a non-periodic flow domain, the aspect ratio of the cylinder would have to be 100 to 1. This is unfavorable and would require an excessive number of fluid elements. On the other hand, the periodic framework allows for simulation of an infinitely long capillary using a short domain. In the present work, a cylinder with an aspect ratio of 2.4 to 1 was used. Three RBCs were placed in the domain to achieve the desired hematocrit. In the periodic framework, the total effective distance traveled by a RBC with a fixed velocity is controlled by the duration of the simulation. Since capillaries are typically 1 mm or shorter [90], simulations were run on the order of 1 second of simulated time. The time duration required for a particle to travel from the capillary entrance at the arteriole to the exit at the venule will be referred to as the *residence time*.

Based on calculations done in the developing flow framework, a mean plasma velocity of 1.03 mm/s and red blood cell velocity 1.35 mm/s provided the target mean blood velocity of 1.10 mm/s. The RBC velocity was directly set to 1.35 mm/s throughout the simulation and imposed by both the displacement of the immersed boundary surfaces defining the RBCs as well as the velocity boundary conditions at the immersed surfaces. The plasma velocity was imposed by adjusting the Re_τ parameter until the dimensional u_{bulk} reached 1.0 mm/s. As described in Chapter 2, flow was induced in the periodic domain by adding a stream wise pressure gradient into the governing equations.

5.1.2 Fluid Meshes

A uniform Cartesian background fluid mesh was generated containing 48 total blocks in a 3×4×4 configuration. Each fluid block contained 65,536 fluid nodes in a 64×32×32 configuration. Thus, the total number of elements was about 3.1 million. This number of fluid elements yielded a mesh sufficiently fine to resolve the flow in the thin spaces between the RBCs, bacteria, and capillary wall. The simulations were run on 48 processing cores so one fluid block was assigned to each core. The configuration of the blocks is shown in Figure 5.1. Each block contained 16 cache blocks in a 3×2×4 configuration for a total of 4096 elements per cache block.

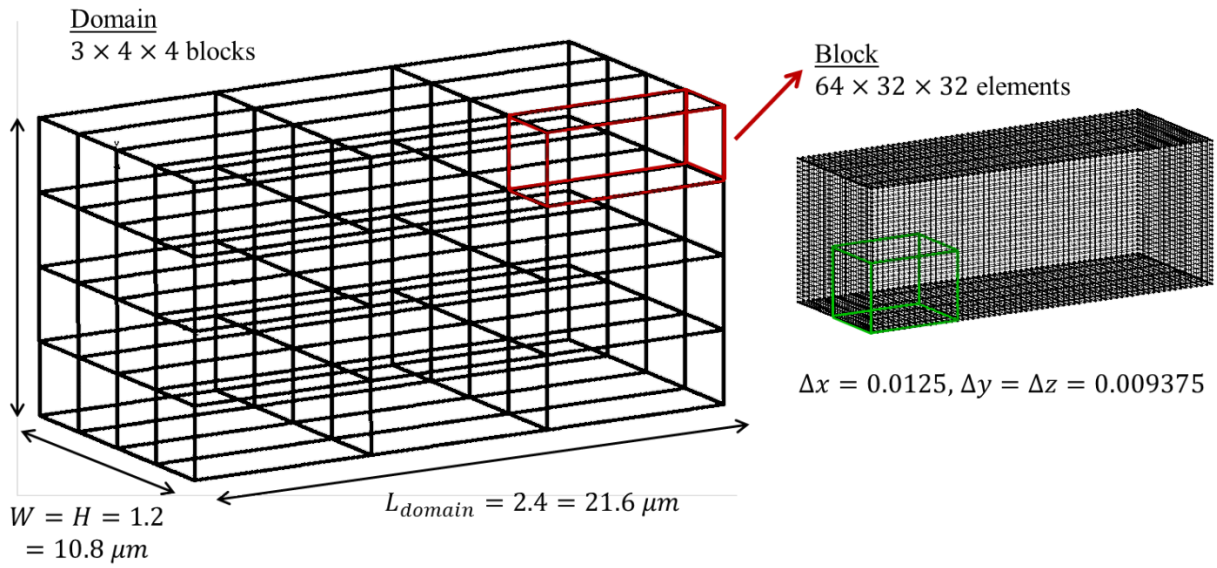

Figure 5.1. Left: periodic fluid domain with block structure. The red box is a single block. Right: characteristic block with elements. The green box is a single cache block.

The capillary walls were imposed using the immersed boundary method. An unstructured triangular capillary surface mesh was created by diagonalizing a structured cylindrical mesh depicted in Figure 5.2.

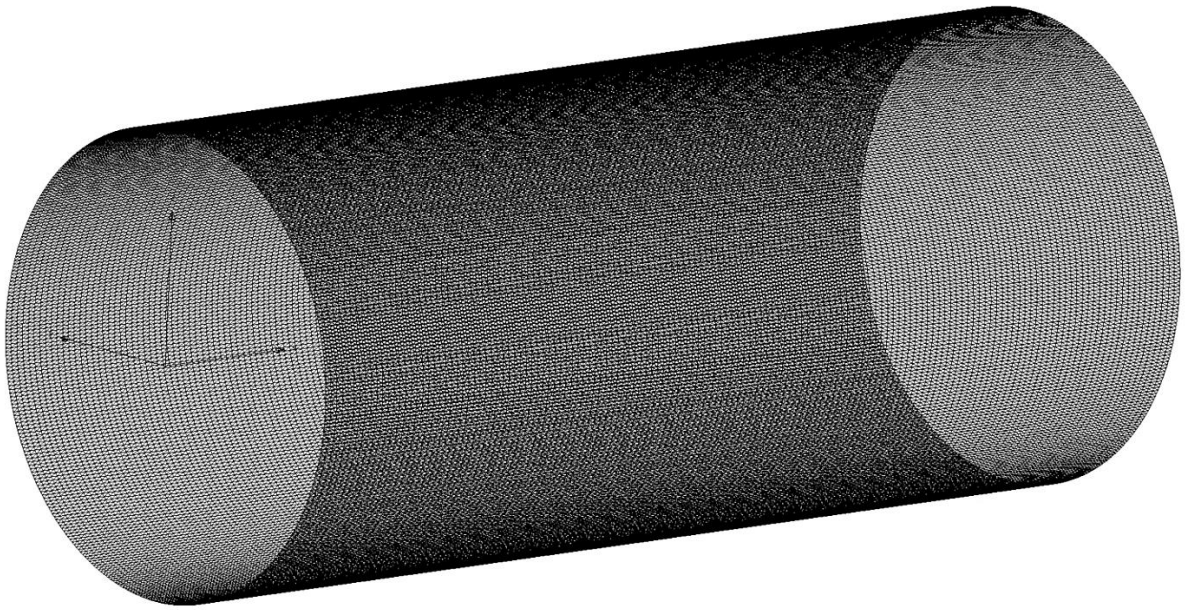

Figure 5.2. The cylindrical surface mesh which defines the capillary wall is placed inside the fluid domain.

The surface meshes for the nanoparticles, bacteria, and red blood cells are shown in Figure 5.3.

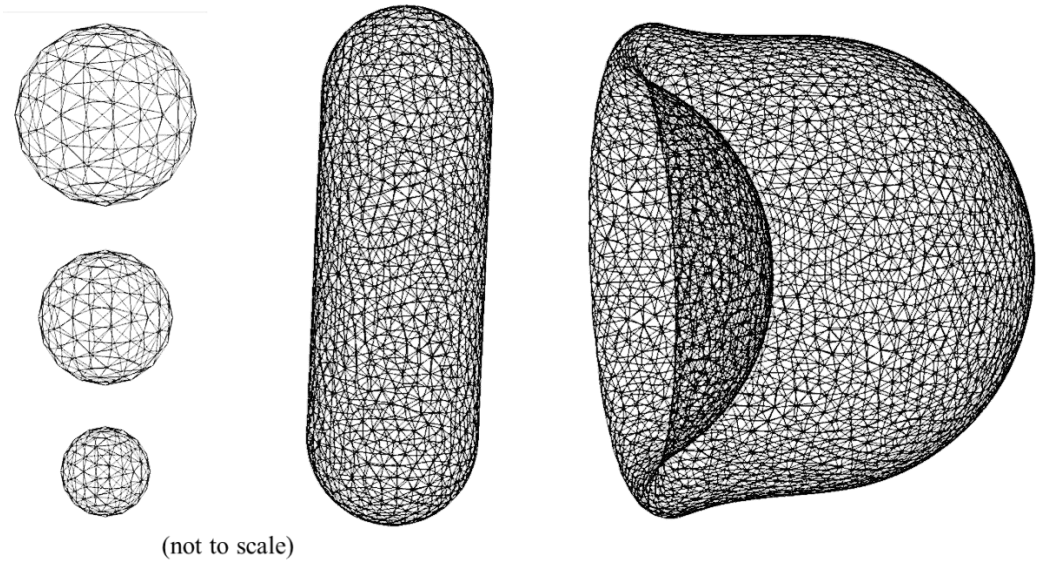

Figure 5.3. Left: 405 nm, 300nm, 200 nm particle meshes. Center: Rod shaped *E. coli* surface mesh. Right: A deformed red blood cell mesh for a 9 µm diameter capillary flowing at 1.1 mm/s. The RBC shape was determined using the process described in Chapter 3.

All the mesh parameters are aggregated in Table 5.1. The immersed surfaces were meshed with edge lengths to be of the same order as the average fluid element length.

Table 5.1 The fluid and IBM surface mesh parameters which were used are shown below. Δ represents the average edge length of a fluid or surface element. The non-dimensional and dimensional values are provided

Mesh	**Elements**	**Vertices**	$\Delta_{average}$ **(nd)**	$\Delta_{average}$ **(nm)**
fluid	3,145,728	3,211,713	0.010	93 nm
capillary	118,008	60,000	0.014	125 nm
red blood cells	7,434	3,831	0.023	207 nm
bacteria	3,110	1,602	0.0077	69 nm
200 nm particle	276	166	0.0035	32 nm
300 nm particle	276	166	0.0053	48 nm
405 nm particle	276	166	0.0074	67 nm

Typical fluid and surface meshes for a simulation are shown in Figure 5.4 and Figure 5.5 in their initial locations. The capillary surface mesh remained stationary, while the RBC, bacteria, and nanoparticle meshes move based on interactions with the fluid.

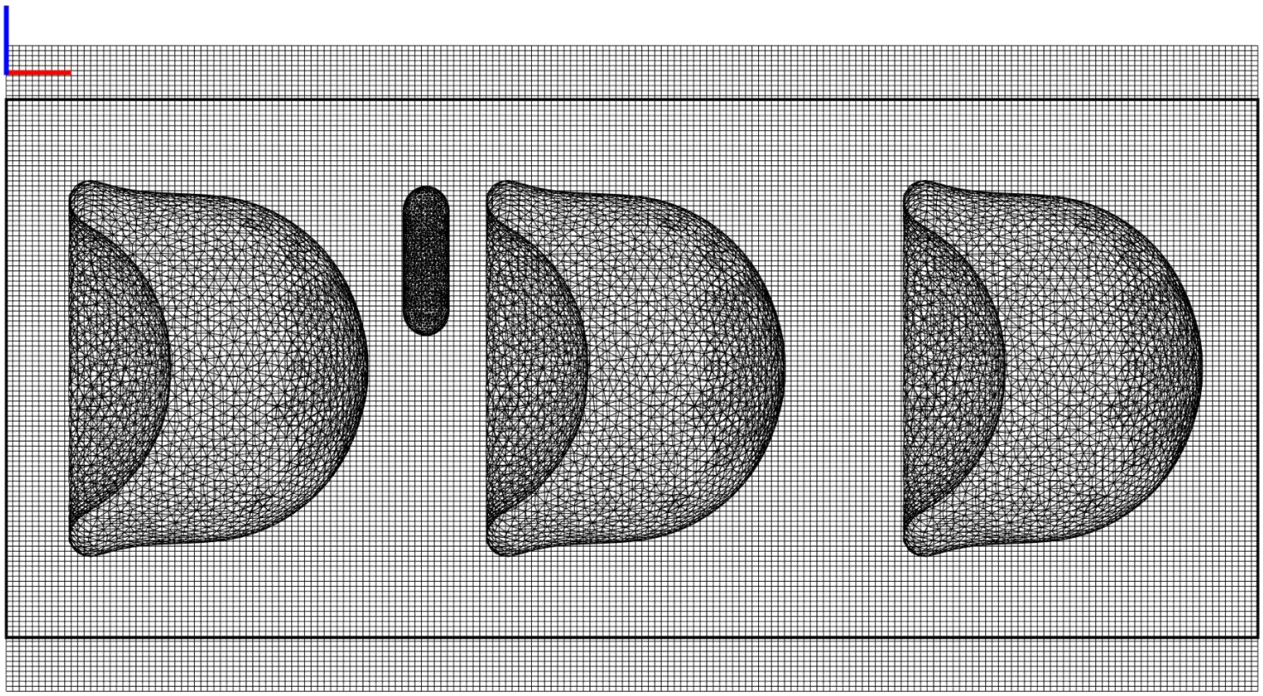

Figure 5.4. Fluid and surface meshes for a standard simulation setup. View is in the +y direction.

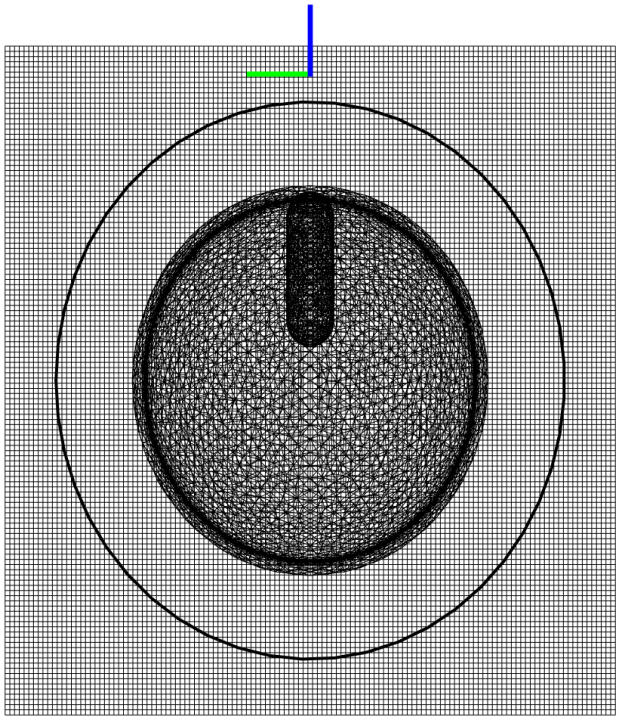

Figure 5.5. Fluid and surface meshes for a standard simulation setup. View is in the +x (streamwise) direction.

5.1.3 Assumptions and Justifications

This section will define and provide justification for the key assumptions underlying the simulations described in this chapter. The first assumption is that the fluid timescale is much smaller than the timescale of the bacteria. Physically, this is due to the highly viscous nature of the system. The viscous timescale is given by the square of the capillary radius over the kinematic viscosity, $\frac{R^2}{\nu}$, and is $\mathcal{O}(10^{-5})$ seconds. This is 5 orders of magnitude lower than the bacteria timescale, $\mathcal{O}(1)$ seconds. Thus, fluid field adjusts almost instantaneously to any perturbation caused by movement of the red blood cells or bacterium. The pseudo-steady method described in Chapter 2 is appropriate for the present simulations.

The second assumption is that the Stokes number of the bacteria and nanoparticles is negligible—that is, Stk << 1. The Stokes number is defined as,

$$Stk = \frac{t_0\, u_p}{D_{par}} \tag{5.4}$$

where u_p is the plasma velocity, D_{par} is the effective particle diameter, and t_0 is the relaxation time defined as,

$$t_0 = \frac{\rho_{par}\, {D_{par}}^2}{18\, \mu_p} \tag{5.5}$$

where ρ_{par} is the particle density, and μ_p is the plasma viscosity. The Stokes numbers in the present simulations are $Stk_{bact} \approx 10^{-4} \ll 1$, and $Stk_{np} \approx 10^{-5} \ll 1$ when taking the bacteria to be a 2 μm sphere with a density of $1105\ \frac{kg}{m^3}$, and taking the particles to be polystyrene spheres with diameters of 300 nm. The very low Stokes numbers means all the solid particles will move along the streamlines, and that there is no time lag for the particles to adjust to a transient fluid field. Numerically, this means that the particles directly take on the local fluid velocity at each time step—this process was described in detail as velocity based IB movement in section 2.2.3.

The third assumption is that Browning motion is not a major factor in the intracapillary transport of therapeutics. In the context of mass transport, the Peclet number is defined as the ratio of the rate of advection to the rate of mass diffusion as shown in equation 5.6. When Pe >> 1 advection dominates over diffusion.

$$Pe = \frac{advection}{diffusion} = \frac{D_c\, u_p}{D} \tag{5.6}$$

where D_c is the diameter of the capillary, u_p is the plasma velocity, and D is the Brownian diffusivity of the particle. With respect to bacteria, $Pe \approx 5 \times 10^4$ and with respect to 300 nm particles, $Pe \approx 10^4$. Thus, diffusivity should not be a dominant force in the system. Since we are primarily interested in the radial distribution of therapeutics, it could be argued that the

maximum radial velocity should be used in place of the plasma velocity as the characteristic velocity. Even for smaller particles and using the radial velocity—$u_{radial} \approx 50 \frac{\mu m}{s}$ and $r_{par} \approx 50\, nm$—the Pe is still order 100. That is, advection is two orders of magnitude higher than diffusion.

The fourth assumption is that collisions between a bacterium and RBC or a bacterium and the capillary wall do not result in rebounding. Mathematically, the coefficient of restitution (COR) of the collisions can be assumed to be zero. This is because the kinetic energy of a swimming bacterium is extremely low, as well as because there is so much viscous damping by the fluid in the system. A bacterium colliding with an object results in total loss of relative velocity between the bacteria and the object. Additionally, a bacterium colliding with an RBC is assumed not to affect the trajectory of the RBC. This is because the RBC has about 60 times the mass of the bacterium.

The fifth assumption is that the pressure drop from the arteriole to the venule is relatively constant in time. That is, pulsatile effects are negligible. In biofluid mechanics, the Womersley number is often used to quantify the level of pulsatility in a flow. It is defined as,

$$\alpha^2 = \frac{transient\ effects}{viscous\ effects} = \frac{\omega\, {D_c}^2}{\nu} \tag{5.7}$$

where ω is the frequency of oscillations, D_c is the vessel diameter, and ν is the kinematic viscosity. Several references in the literature report $\alpha \approx 10^{-4}$ [90, 91]. Thus, pulsatility can safely be neglected.

The sixth assumption is that any curvature in an actual capillary can be neglected in the current model with no effect on the solution. The Dean number is defined as,

$$De = \frac{centripetal\ effects * inertial\ effects}{viscous\ effects} = \sqrt{\frac{D_v}{2\ R_{curve}}}Re \quad (5.8)$$

where D_v is the diameter of the blood vessel and R_{curve} is the radius of the bend. Even for a highly curved capillary—i.e. a 180° u-bend—the Dean number cannot exceed the Reynolds number because geometrically, $R_{curve} \geq D_v$. Regardless of the curvature, in a low Reynolds number system the Dean number will be small. Thus, the effects of curvature do not impact the flow field inside the capillary. [90]

5.2 Nanoparticle Simulations

5.2.1 Nanoparticle Simulation Setup

The nanoparticle simulations contained 18 nanoparticles with diameters 200 nm to 405 nm placed in a periodic domain. Since the fluid field was mostly axisymmetric, the starting location of the nanoparticle was defined in terms of a radius from the centerline. The goal of the initial setup was to vary the radius across the sample of nanoparticles. The initial configuration is show in Figure 5.6.

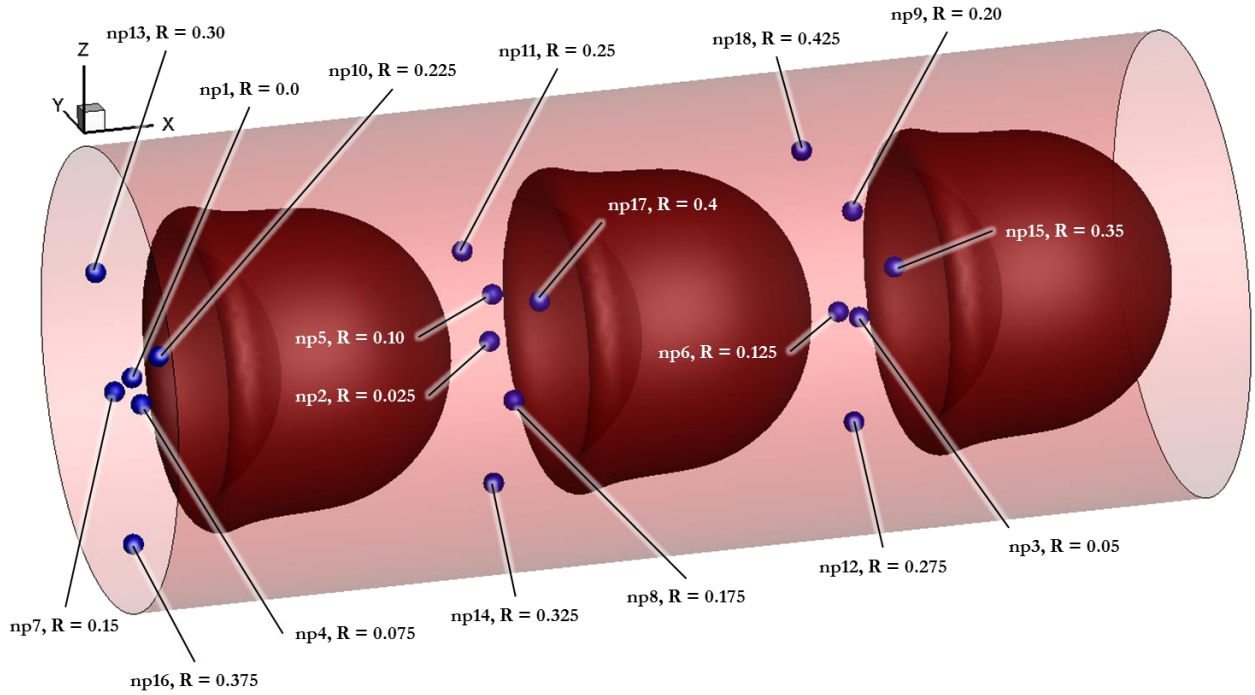

Figure 5.6. 18 nanoparticles are distributed in the domain with their respective initial distance from the centerline, R, varying from 0.0 to 0.425—the non-dimensional the capillary radius is 0.5.

The fluid parameters were set as described in section 5.1.1—that is, the RBC velocity was fixed at $u_{rbc} = 1.35\ \frac{mm}{s}$, while the average plasma flow velocity equilibrated to $u_{bulk} \approx 1.0\ \frac{mm}{s}$. The simulations were run for durations of 0.3 sec to 1.1 seconds required for streamwise travel of approximately 400 μm to 1.5 mm. An average capillary is around 0.5 mm to 1.0 mm long [90]. Despite the initial prediction that Brownian motion would have a limited effect on particle transport, several simulations were run with non-zero diffusivity to verify this hypothesis. In order to implement Brownian motion, the Stokes-Einstein equation was used to calculate the diffusivity of the particle as shown in equation 5.9.

$$D = \frac{k_B T}{6\,\pi\,\mu_p\,\frac{D_{par}}{2}} \qquad 5.9$$

where k_B is Botzmans constant, T is temperature, μ_p is the plasma viscosity, and D_{par} is the particle diameter. Over the interval of one time step, Δt, the root mean squared displacement due to Brownian motion was calculated as,

$$\sqrt{\langle r^2 \rangle} = \sqrt{6\, D\, \Delta t} \qquad 5.10$$

This estimated root mean squared displacement was applied to each particle in a random direction at each time step.

Figure 5.7 gives an overview of the computational procedure used for the nanoparticle simulations. Detailed explanation for the numerical implementation can be found in Chapter 2. Additionally, a subroutine call graph is provided in the Appendix for reference.

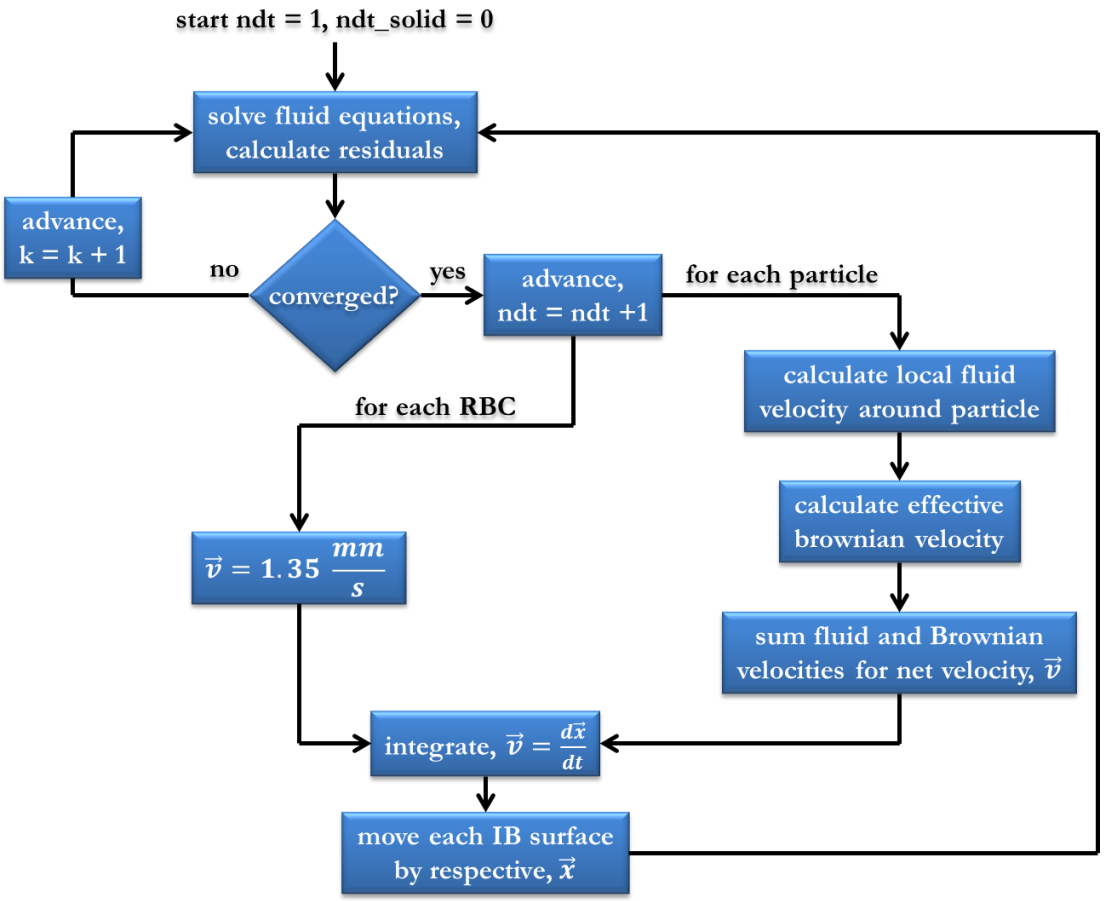

Figure 5.7. The basic process for the nanoparticle simulations is shown. Further details are described in Chapter 2.

5.2.2 Results from Nanoparticle Simulations

Eleven simulations with were run with the input parameters shown in Table 5.2. Each simulation was run using the initial positions of the 18 nanoparticles as shown in Figure 5.6.

Table 5.2. Eleven nanoparticle simulations were run using the parameters shown. The two convergence tolerances correspond to the velocity infinity norm and the change in flowrate as defined in Section 2.3. A zero diffusivity means that no Brownian motion was used.

Run Number	Time step	Convergence Tolerances	Particle Diameter	Diffusivity	Duration
1	5e-4 sec	1e-5/2e-5	300 nm	0.0 m^2/s	0.36 sec
2	1e-3 sec	1e-6/2e-5	300 nm	0.0 m^2/s	0.34 sec
3	1e-3 sec	1e-5/2e-5	200 nm	0.0 m^2/s	1.00 sec
4	1e-3 sec	1e-5/2e-5	300 nm	0.0 m^2/s	1.00 sec
5	1e-3 sec	1e-5/2e-5	405 nm	0.0 m^2/s	0.85 sec
6	1e-3 sec	1e-5/2e-5	200 nm	1.9e-12 m^2/s	0.89 sec
7	1e-3 sec	1e-5/2e-5	300 nm	1.3e-12 m^2/s	0.61 sec
8	1e-3 sec	1e-5/2e-5	405 nm	9.4e-13 m^2/s	0.86 sec
9	1e-3 sec	1e-5/2e-5	200 nm	1.9e-12 m^2/s	0.87 sec
10	1e-3 sec	1e-5/2e-5	300 nm	1.3e-12 m^2/s	1.11 sec
11	1e-3 sec	1e-5/2e-5	405 nm	9.4e-13 m^2/s	0.84 sec

Runs 1 and 2 were carried out to determine an appropriate time step and fluid convergence tolerance. Runs 3 through 5 were run to study the particle motion due to the fluid dynamics without Brownian motion. Runs 6 through 11 were run to test the effect of Brownian motion for comparison to runs 3, 4, and 5.

Velocity contours and streamlines of a characteristic nanoparticle simulation are shown for both absolute and relative velocity of blood plasma in Figure 5.8 and Figure 5.9. The plots are taken from simulation 4 which contained 300 nm particles.

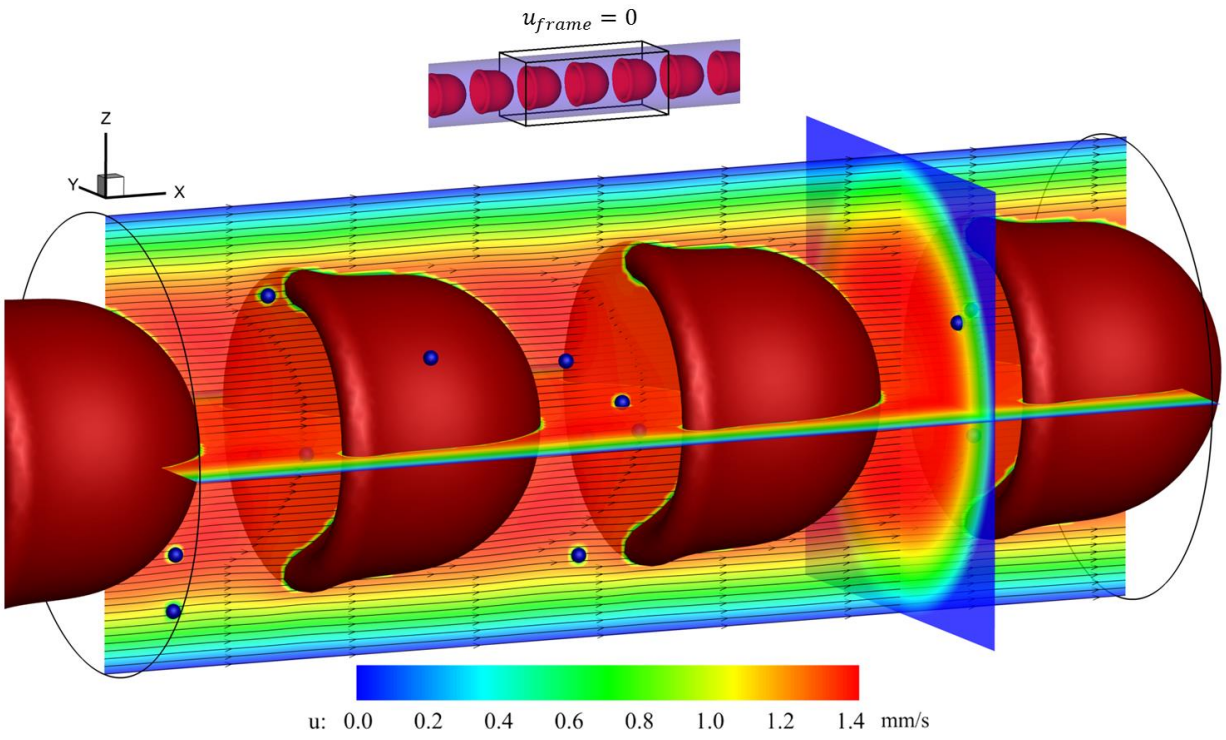

Figure 5.8. Contours of absolute velocity with streamlines. A well-defined ring of low velocity plasma can be seen in the cross-sectional slice.

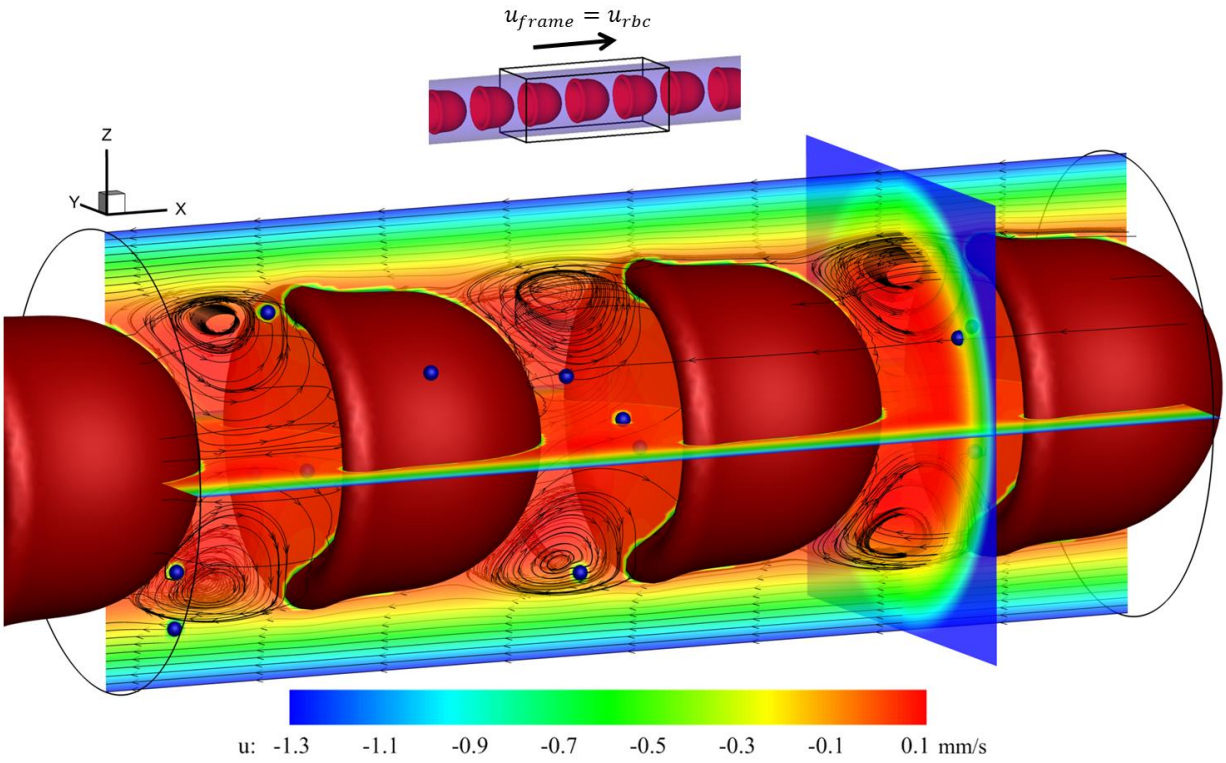

Figure 5.9. Contours of relative velocity with streamlines. The relative velocity field is generated by subtracting the absolute velocity field by the reference frame velocity (which is the RBC velocity).

Initial observation of the qualitative data indicated that nanoparticles situated between the RBCs tended to remain there at a nearly identical velocity as the RBCs. Nanoparticles in the outer plasma layer tended to stay in the near wall region at a significantly lower axial velocity. Conversely, nanoparticles in the intermediate region moved around more as they were impacted by the radial fluid velocity appearing in the RBC wakes. The nanoparticles in the simulations with Brownian motion had a noticeable jiggle as expected, but it was unclear as to the actual impact on the particle transport or the particle distribution in the capillary looking at the qualitative data.

Figure 5.10 to Figure 5.13 show the paths of the 18 nanoparticles during a characteristic simulation. The location trace is designated by the radial and streamwise components separately.

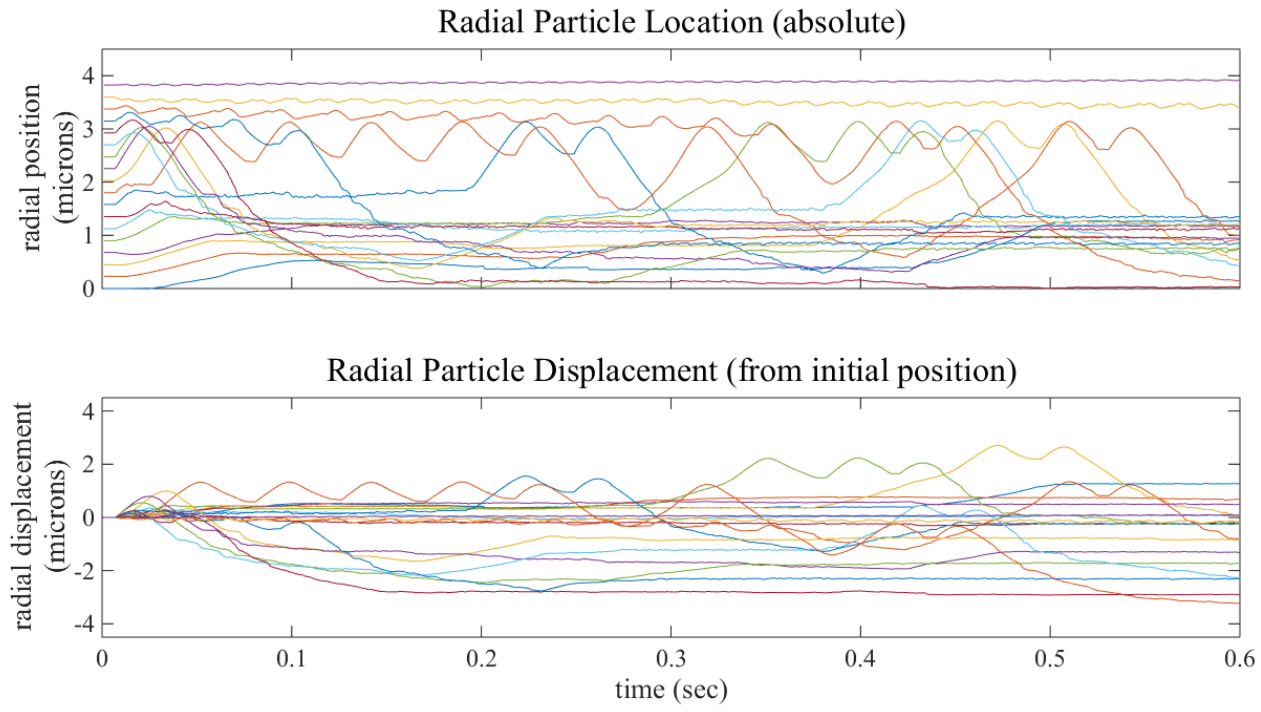

Figure 5.10. Radial position traces for 300 nm particles. No Brownian motion was used.

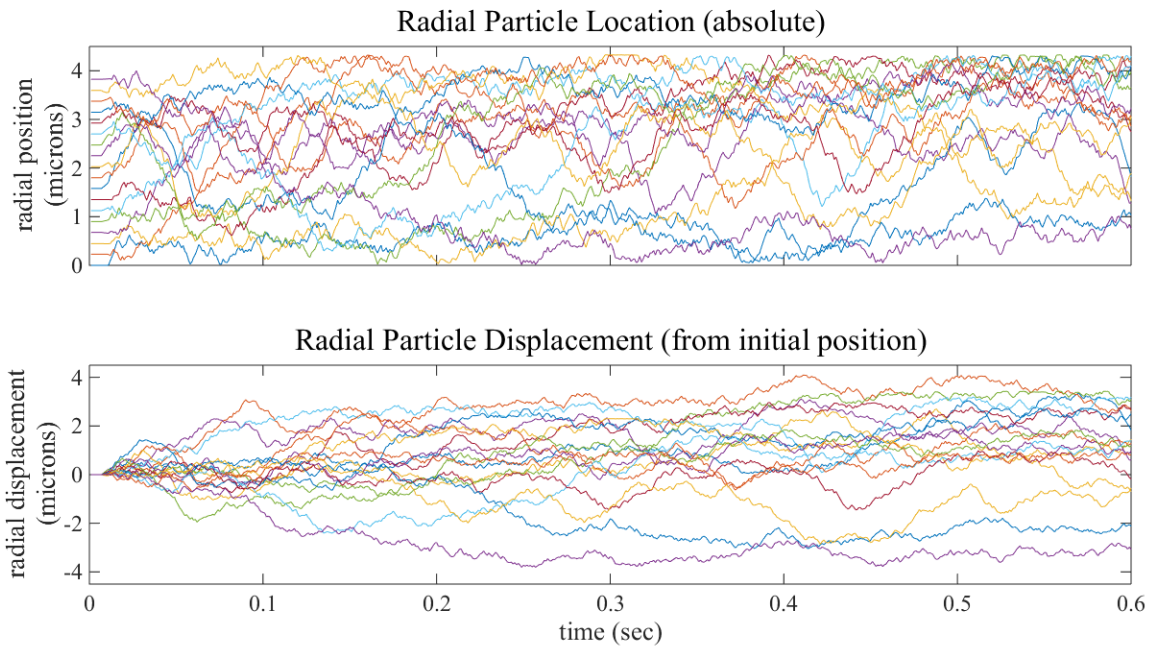

Figure 5.11. Radial position traces for 300 nm particles. Brownian motion was used (D = 1.3×10^{-12} m^2/s).

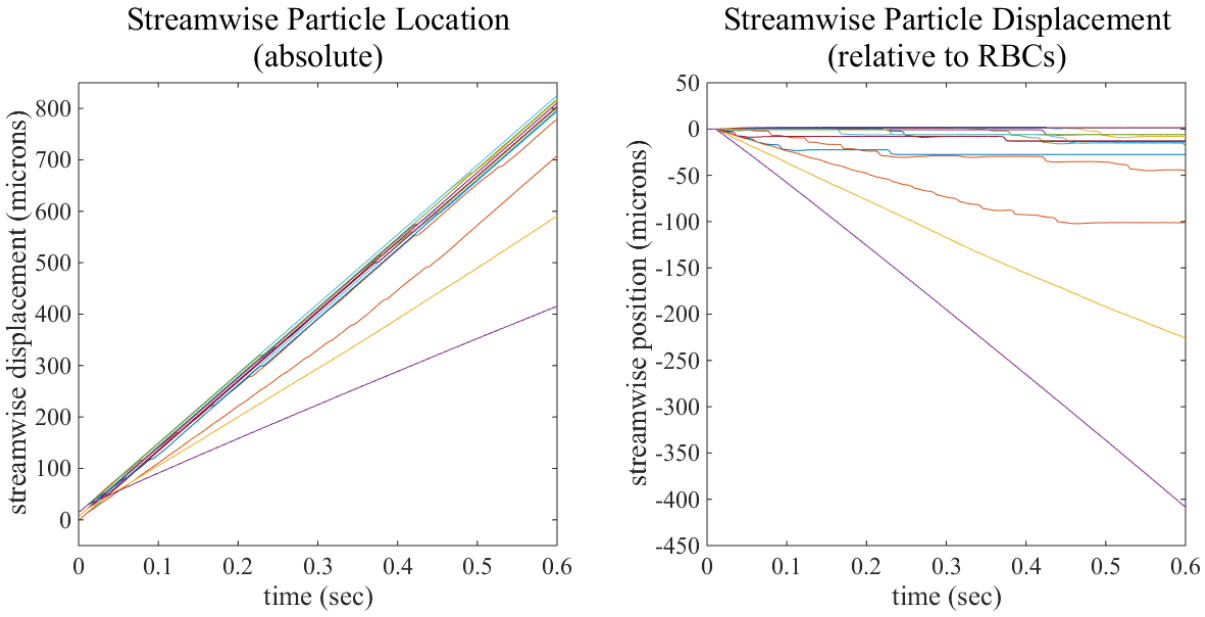

Figure 5.12. Streamwise position traces for 300 nm particles. No Brownian motion was used.

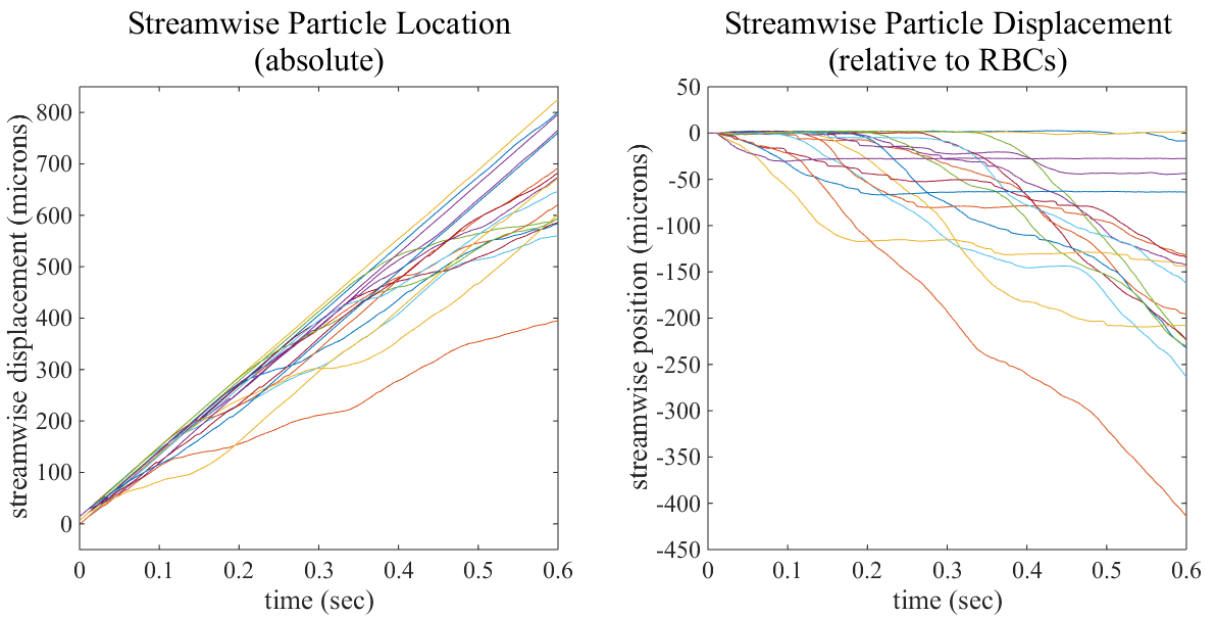

Figure 5.13. Streamwise position traces for 300 nm particles. Brownian motion was used (D = 1.3×10^{-12} m^2/s).

There is some difference in the fluctuations when the Brownian motion is used, but the general trends are similar. Figure 5.14 through Figure 5.16 show time averaged results plotted versus the starting positions of the nanoparticles.

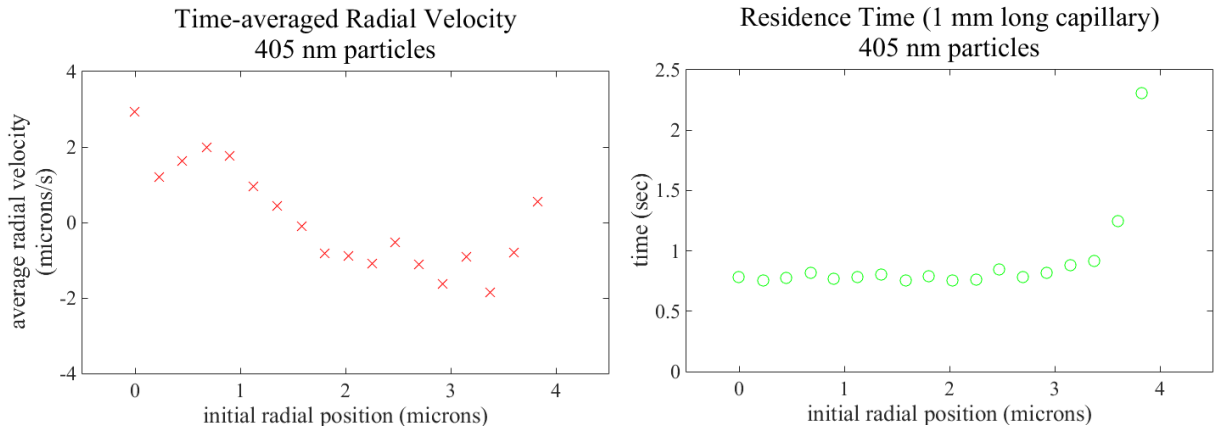

Figure 5.14. Time averaged results are shown for 405 nm particles. Results are averaged from multiple simulations.

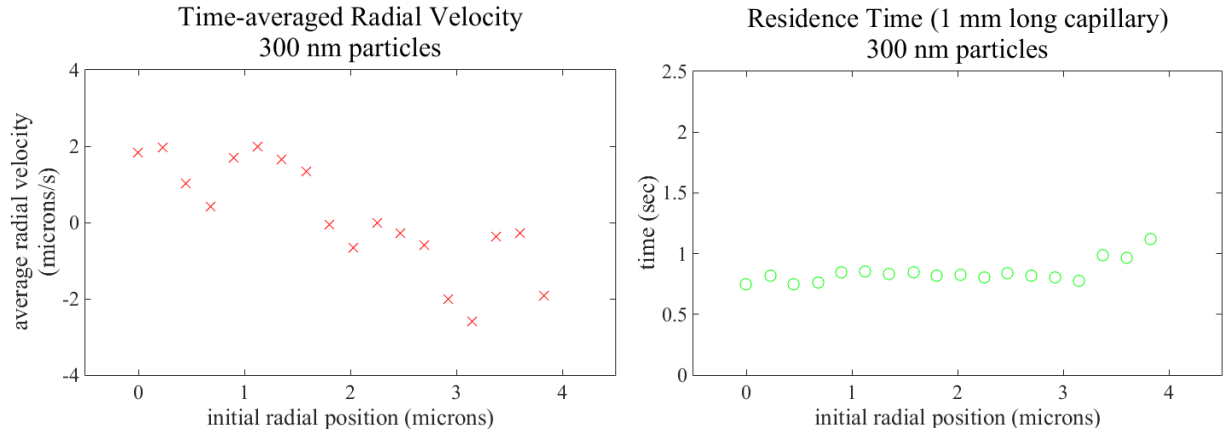

Figure 5.15. Time averaged results are shown for 300 nm particles. Results are averaged from multiple simulations.

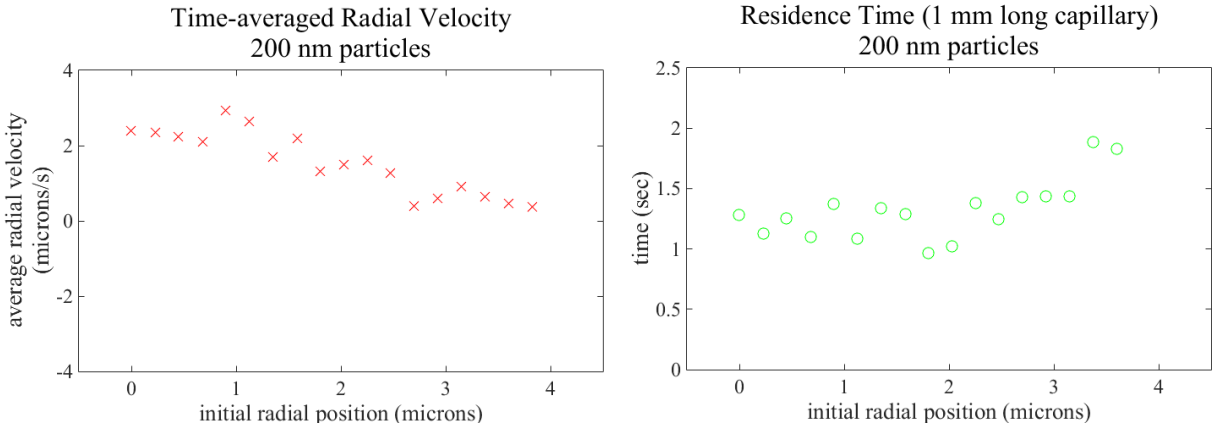

Figure 5.16. Time averaged results are shown for 200 nm particles. Results are averaged from multiple simulations.

5.3 Non-motile Bacteria Simulations

5.3.1 Non-motile Bacteria Simulation Setup

Several cases were run with non-motile bacteria. These bacteria are passively convected through flows and have no propulsion. The movement of the immersed bodies was done using the velocity based approach as described in Section 2.2.4. This movement method is appropriate due to the low Stokes number of the bacterium "particle" in the flow. Additionally, Brownian forces were neglected due to the low Peclet number.

A range of starting locations was used just as in the nanoparticle simulations. The starting positions are shown in Figure 5.17. The initial non-dimensional radii, R, at which the bacteria centroids were placed are 0.0, 0.1, 0.2, 0.3, and 0.4. Four orientations, ±x-facing and ±z-facing, were used. The starting axial (x-dir) position was shifted to prevent initial contact between the bacterium and RBC.

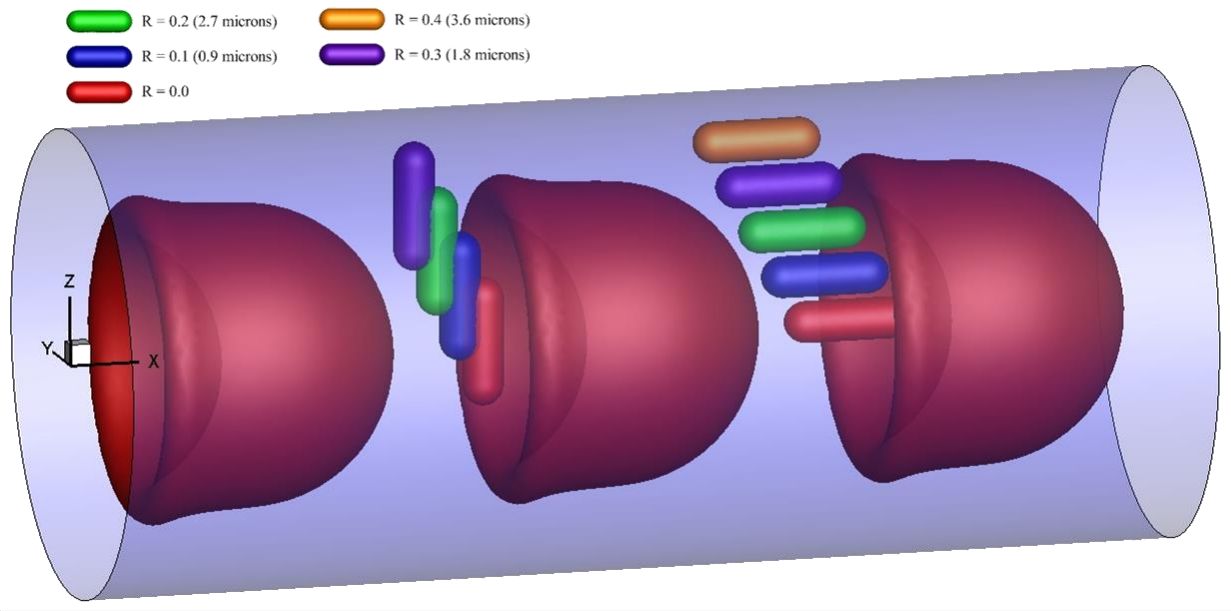

Figure 5.17. Nine different starting positions of bacteria are shown superimposed. Each bacterium position represents two possible configurations—forwards or backwards facing resulting in 17 possible initial conditions. Forwards versus backwards only makes a difference in motile bacteria—thus, there are only 9 possible initial conditions for non-motile bacteria.

Figure 5.18 gives an overview of the computational procedure used in the non-motile bacteria simulations.

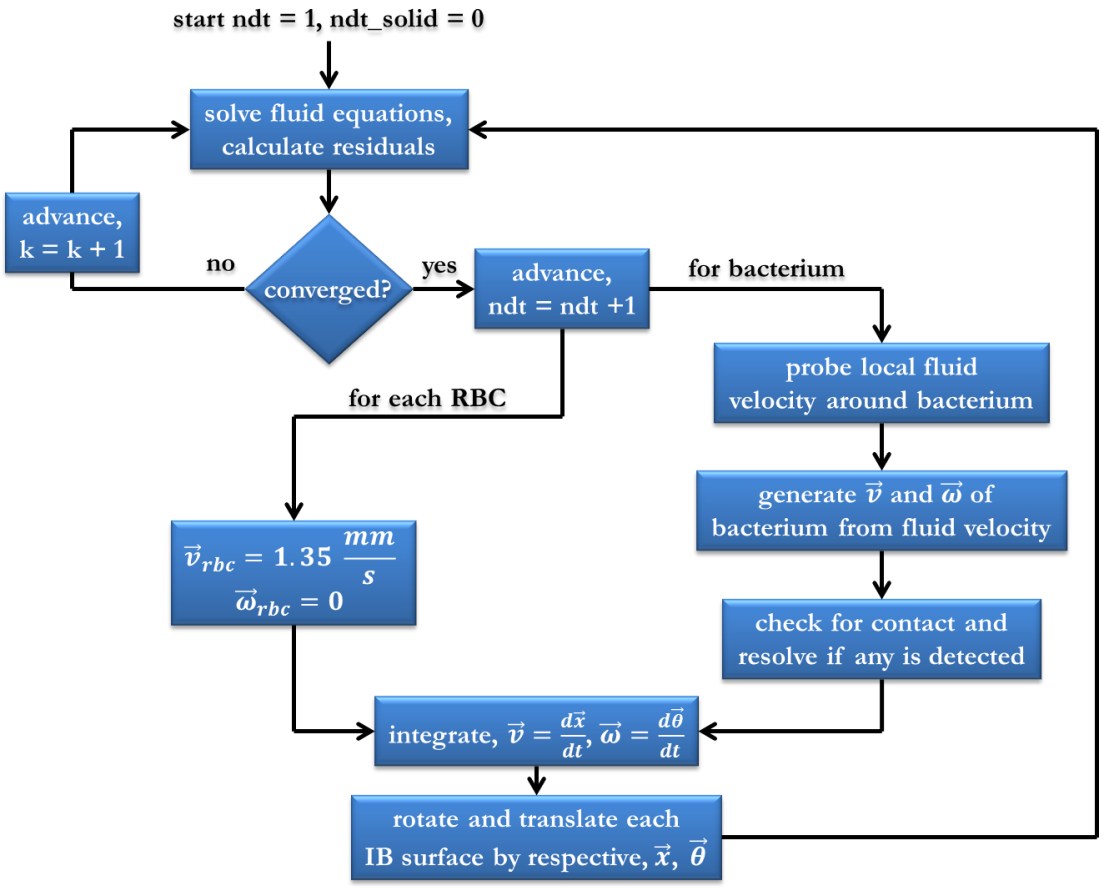

Figure 5.18 An overview of the computational process for the non-motile bacteria simulations is shown. Further details are described in Chapter 2.

The same basic procedure is used as in the nanoparticle simulations with a few key differences. First, rotation is needed due to the capsule shape of the bacteria. Second, contact is explicitly resolved using the algorithm described in Chapter 2. Lastly, no Brownian velocity is applied, since the effect of thermal noise on bacteria motion is negligible.

5.3.2 Results from Non-motile Bacteria

Nine different non-motile bacteria simulations were run with varying starting locations and orientations. Only one simulation was run for each case since the outcome was deterministic

based on the initial condition. This is in contrast with the motile bacteria simulations which have a stochastic component to their movement. The run parameters are shown in Table 5.3.

Table 5.3 Nine non-motile bacteria simulations were run using the parameters shown. The two convergence tolerances correspond to the velocity infinity norm tolerance and the flowrate convergence.

Case Number	Time step	Convergence Tolerance	Initial Radius	Orientation	Duration
1	5e-4 sec	1e-5/2e-5	0.0	+z	0.72 sec
2	5e-4 sec	1e-5/2e-5	0.1	+z	0.52 sec
3	5e-4 sec	1e-5/2e-5	0.2	+z	0.56 sec
4	5e-4 sec	1e-5/2e-5	0.3	+z	0.14 sec
5	5e-4 sec	1e-5/2e-5	0.0	+x	0.54 sec
6	5e-4 sec	1e-5/2e-5	0.1	+x	1.24 sec
7	5e-4 sec	1e-5/2e-5	0.2	+x	0.56 sec
8	5e-4 sec	1e-5/2e-5	0.3	+x	0.16 sec
9	5e-4 sec	1e-5/2e-5	0.4	+x	0.01 sec

Since there is no front or back to a non-motile bacterium, "+z" orientation simply refers to vertical or radial alignment, while "+x" refers to horizontal or streamwise alignment.

Characteristic results of the velocity field in the capillary along with the bacteria and red blood cells are shown in Figure 5.19 and Figure 5.20. The bacteria are larger than the nanoparticles thus they have more of an impact on the flow. For example, in the relative velocity plot the bacterium can be seen disrupting the circular relative flow structure.

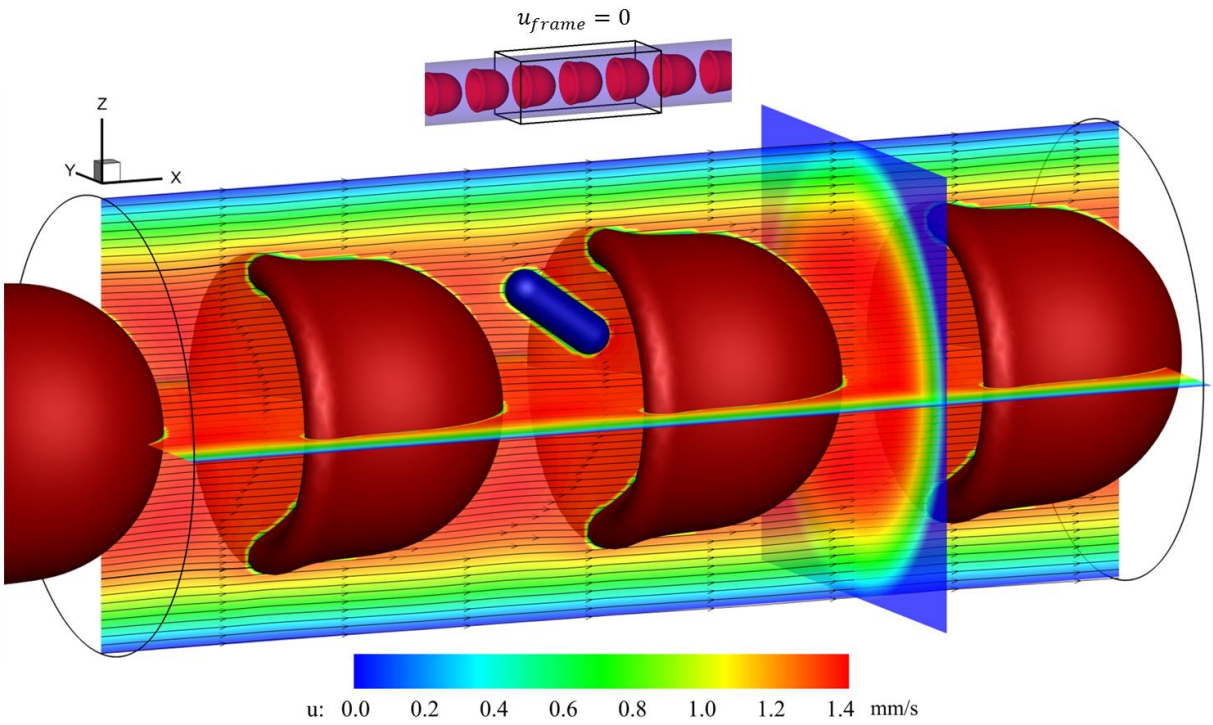

Figure 5.19. Contours of absolute velocity with streamlines. A well-defined ring of low velocity plasma can be seen in the cross-sectional slice.

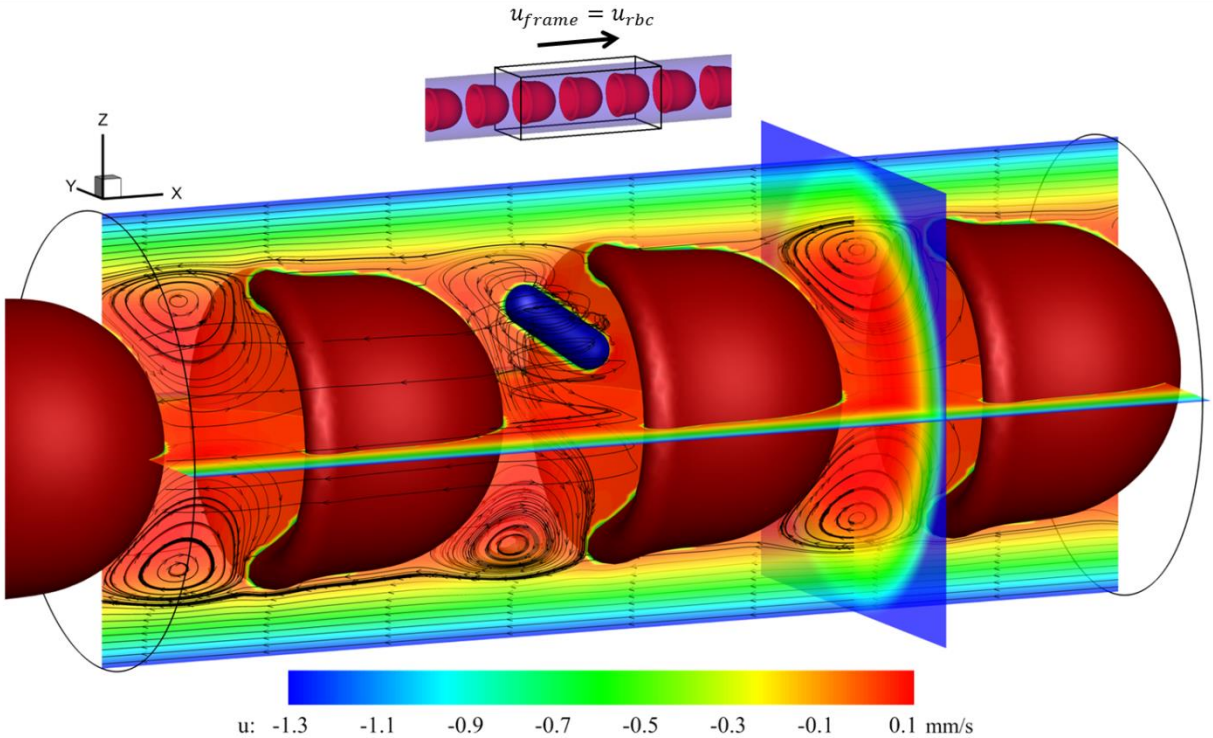

Figure 5.20. Contours of relative velocity with streamlines. The plasma velocity is normalized by the red blood cell velocity. Visualization of relative velocity flow structures gives insight into the radial movement of an object traveling at a similar velocity to the RBCs.

In the non-motile simulations, the bacteria velocity reached a steady state typically within 0.2 seconds. Thus, long simulation times were not needed for these cases. This can be seen in the position plots where the bacterium path is designated by the radial and streamwise components separately.

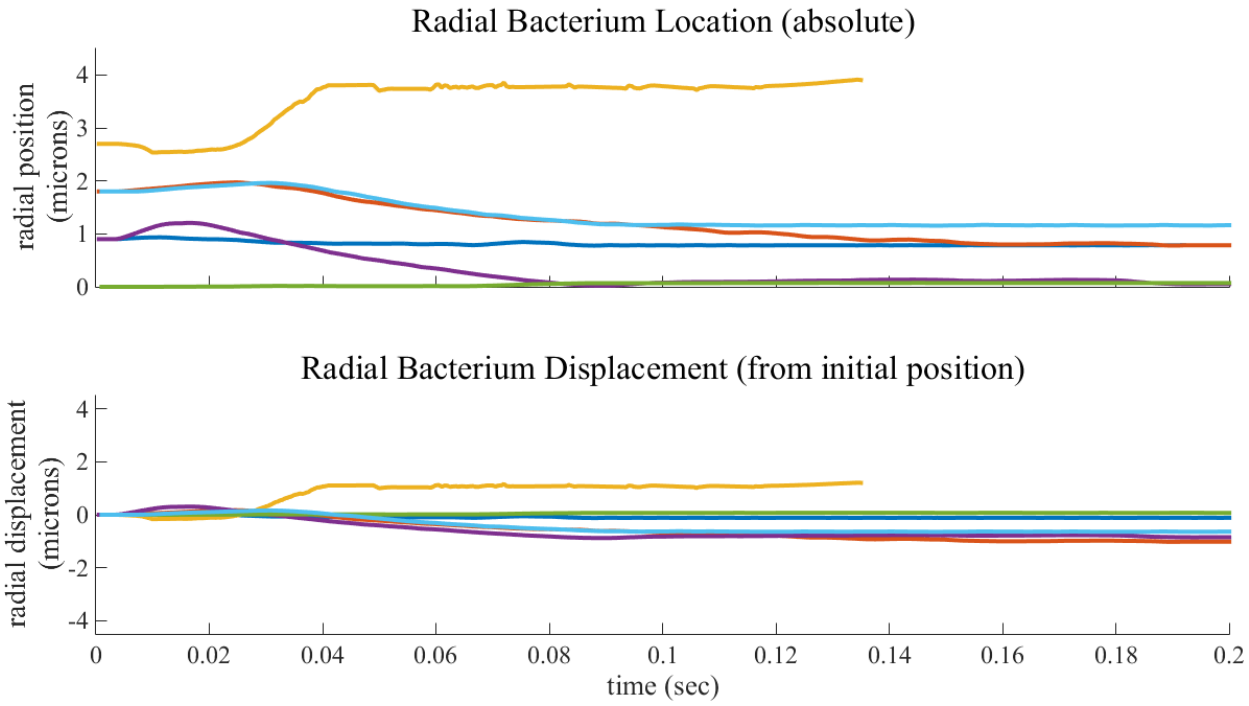

Figure 5.21. Radial position traces for six different non-motile bacterium. The point of divide in the initial positions between bacteria moving towards the center and wall can be seen around R = 2 µm.

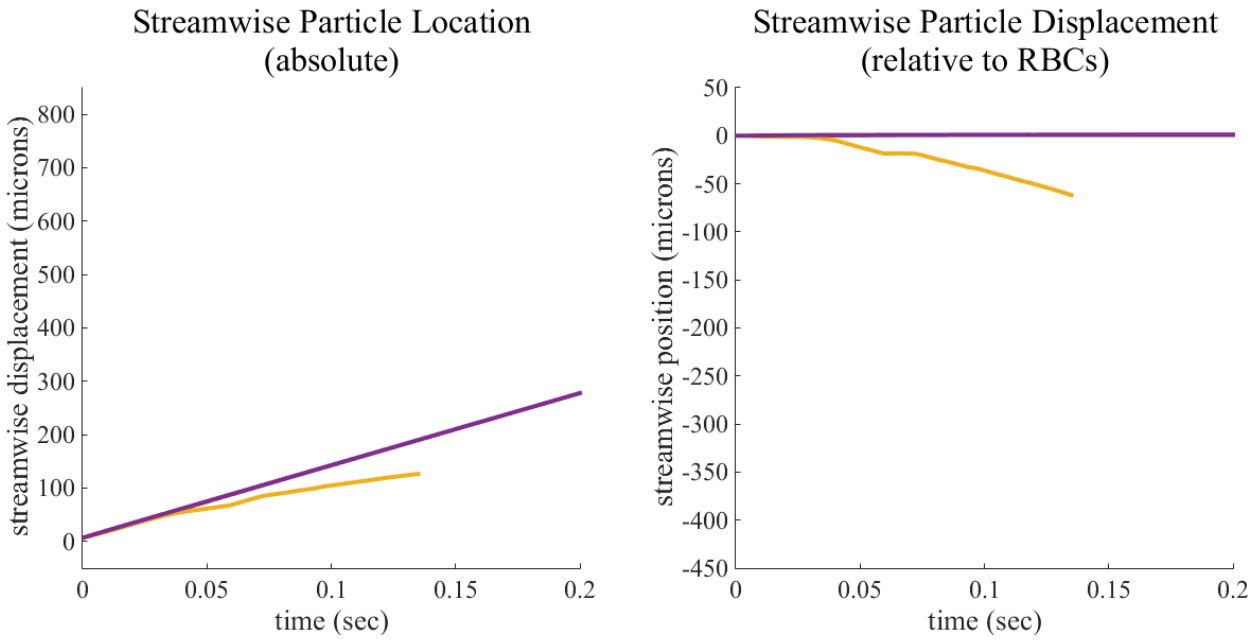

Figure 5.22. Streamwise position traces for six different non-motile bacterium. Non-motile bacterium which start near the center tend to the center and move at the same velocity as the RBCs. Thus, the purple line overlays four other traces.

The non-motile have no stochastic motion and are not strongly affected by small scale perturbations in the fluid field. For this reason, only a few simulations were run for short durations. Figure 5.21shows the bacteria position reaching a steady state in about 0.1 or 0.2 seconds.

5.4 Motile Bacteria Simulations

5.4.1 Motile Bacteria Simulation Setup

For the motile bacteria simulations the starting configurations were the same as the non-motile case. A swimming bacterium has a forward direction, so the orientations “+x”, “-x”, “+z”, “-z” were all used. The bacterium was initiated in a tumble phase and the run/tumble cycle proceeded after that as described in Chapter 4. Several simulation runs were conducted for each starting orientation due to the stochastic nature of the motility model, and the results were averaged over the cases. The basic simulation procedure is shown in Figure 5.23.

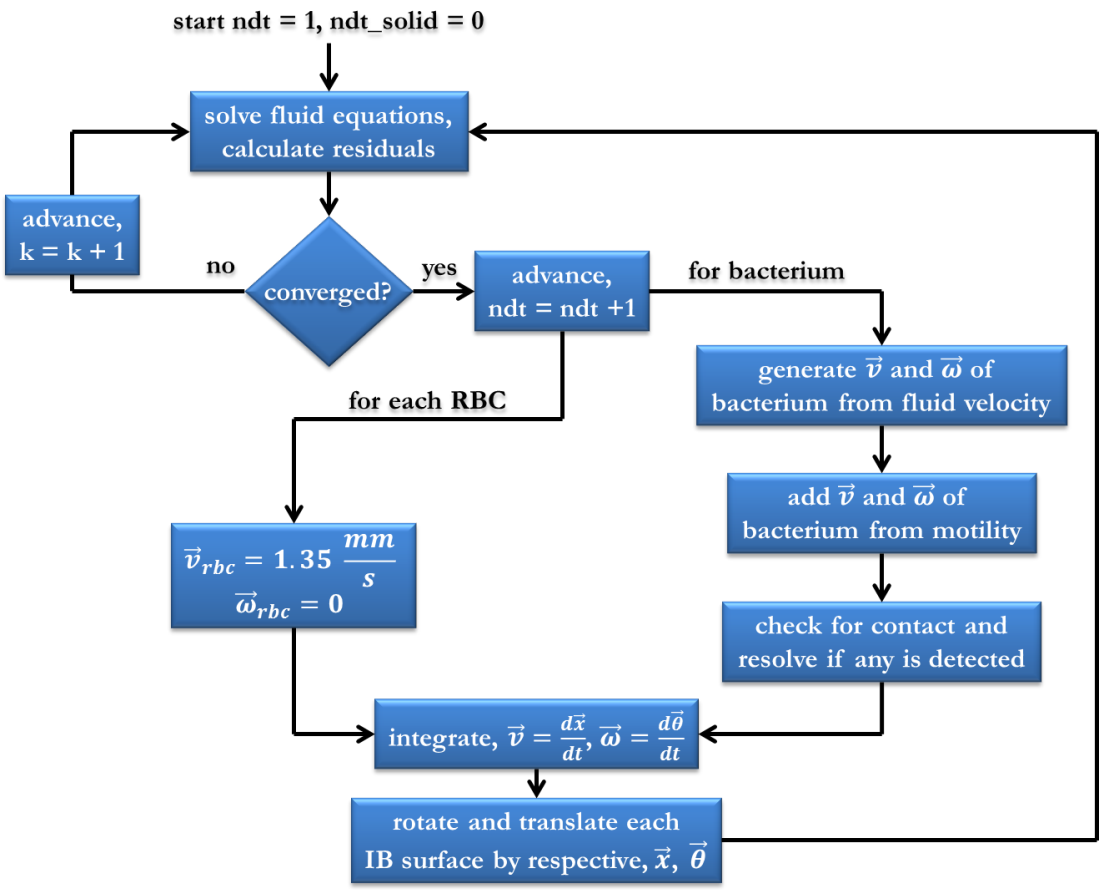

Figure 5.23 An overview of the computational process for the motile bacteria simulations is shown. Further details are described in Chapter 2.

5.4.2 Results from Motile Bacteria

Seventeen cases were run simulating motile bacteria, and several runs were conducted for each case. The parameters for each case are shown in Table 5.4.

Table 5.4. Seventeen non-motile bacteria cases were run using the parameters shown. The two convergence tolerances correspond to the velocity infinity norm tolerance and the flowrate tolerance.

Case Number	Number of Runs	Time step	Convergence Tolerance	Initial Radius	Initial Orientation
1	6	5e-4 sec	1e-5/2e-5	0.0	+z
2	2	5e-4 sec	1e-5/2e-5	0.1	+z
3	4	5e-4 sec	1e-5/2e-5	0.2	+z
4	6	5e-4 sec	1e-5/2e-5	0.3	+z
5	2	5e-4 sec	1e-5/2e-5	0.1	-z
6	2	5e-4 sec	1e-5/2e-5	0.2	-z
7	2	5e-4 sec	1e-5/2e-5	0.3	-z
8	2	5e-4 sec	1e-5/2e-5	0.0	+x
9	10	5e-4 sec	1e-5/2e-5	0.1	+x
10	3	5e-4 sec	1e-5/2e-5	0.2	+x
11	3	5e-4 sec	1e-5/2e-5	0.3	+x
12	2	5e-4 sec	1e-5/2e-5	0.4	+x
13	4	5e-4 sec	1e-5/2e-5	0.0	-x
14	4	5e-4 sec	1e-5/2e-5	0.1	-x
15	4	5e-4 sec	1e-5/2e-5	0.2	-x
16	2	5e-4 sec	1e-5/2e-5	0.3	-x
17	2	5e-4 sec	1e-5/2e-5	0.4	-x

Figure 5.24 and Figure 5.25 show relative and absolute velocity contours along with streamlines for a typical motile bacteria case.

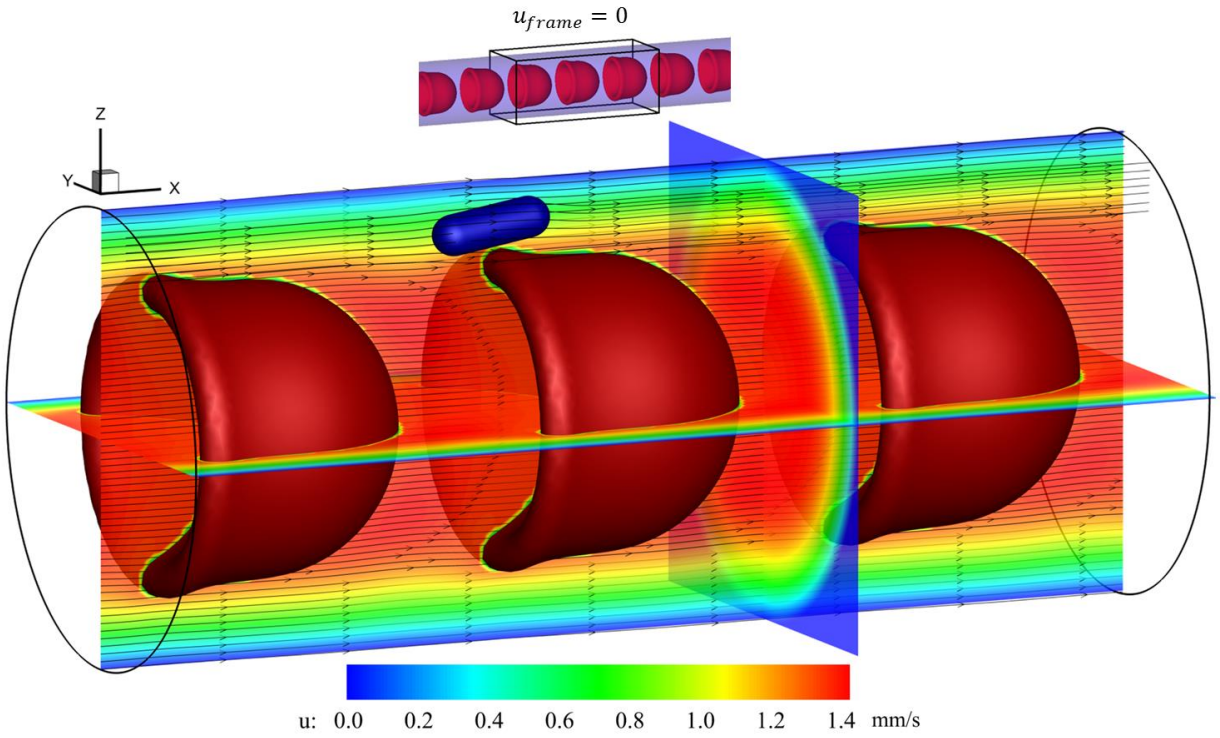

Figure 5.24. Contours of absolute velocity with streamlines. A bacterium in the plasma layer may travel at less than half the speed of the RBCs.

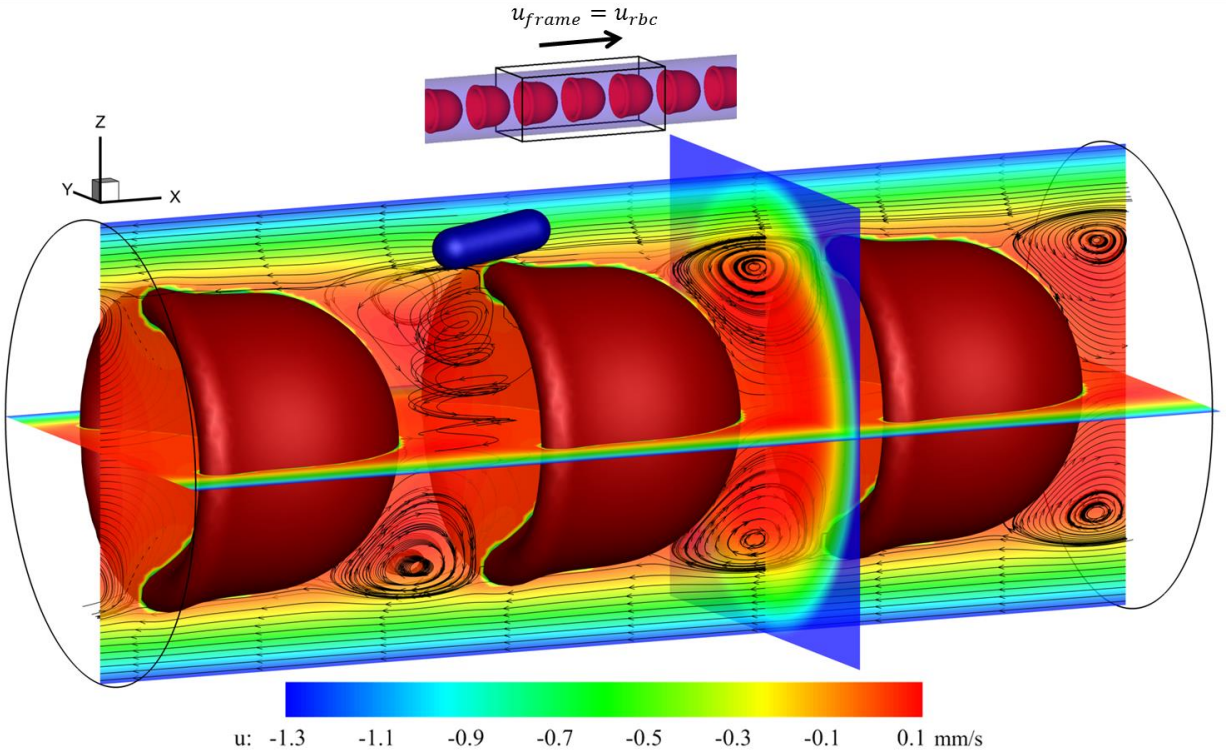

Figure 5.25. Contours of relative velocity with streamlines. The plasma velocity is normalized by the red blood cell velocity.

The fluid velocity field is very similar between the non-motile bacteria and motile bacteria cases differing only due to the instantaneous bacteria location. This is to be expected since inertia is quite low and insignificant in the system. The motion and location of the bacterium varied dramatically between the non-motile and motile cases. Motile bacteria tended to migrate radially eventually reaching the plasma layer regardless of starting location. Conversely, the non-motile bacteria tended to settle either at the capillary centerline or the plasma layer depending on their starting location. Radial and streamwise bacteria traces are shown in Figure 5.26 and Figure 5.27.

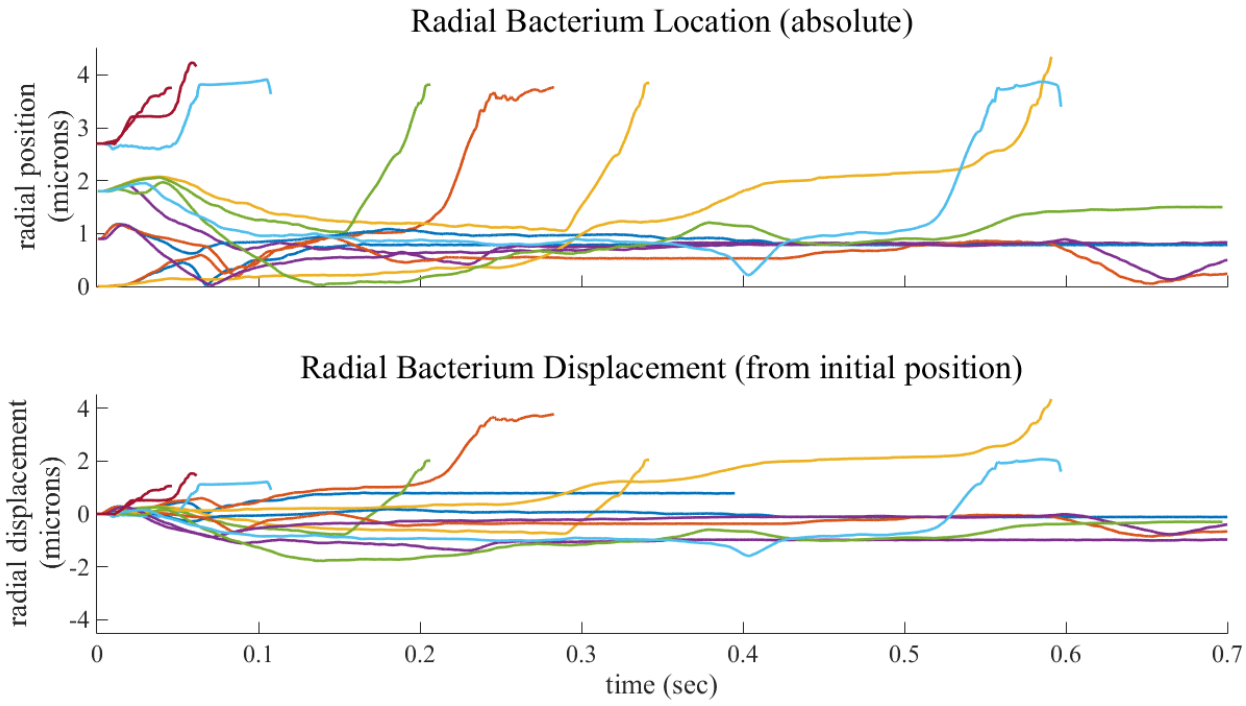

Figure 5.26. Radial position traces for fourteen different motile bacterium are shown. The trend is for a bacterium to move predominately in the streamwise direction until a rapid event causes the bacterium to quickly shift into the plasma layer near the wall.

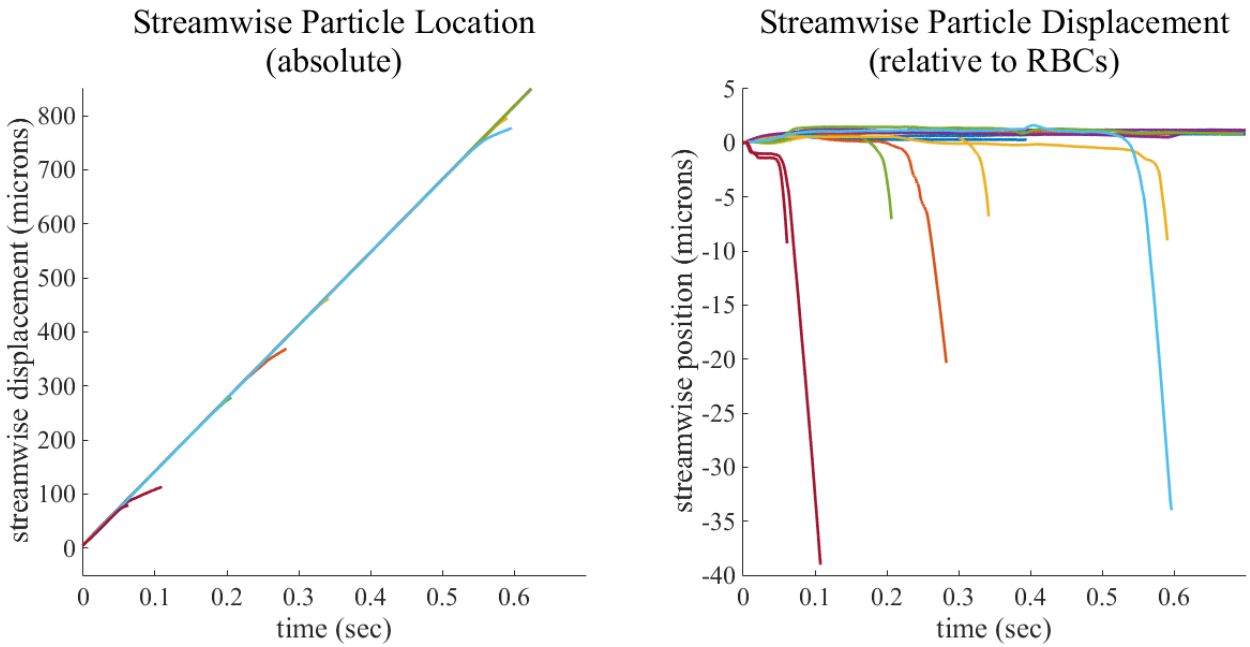

Figure 5.27. Streamwise position traces for fourteen different motile bacterium. A similar trend can be observed as in Figure 5.26.

5.5 Discussion of Results

In order to better understand trends in bacteria and nanoparticle transport, three regions of the flow are defined in Figure 5.28.

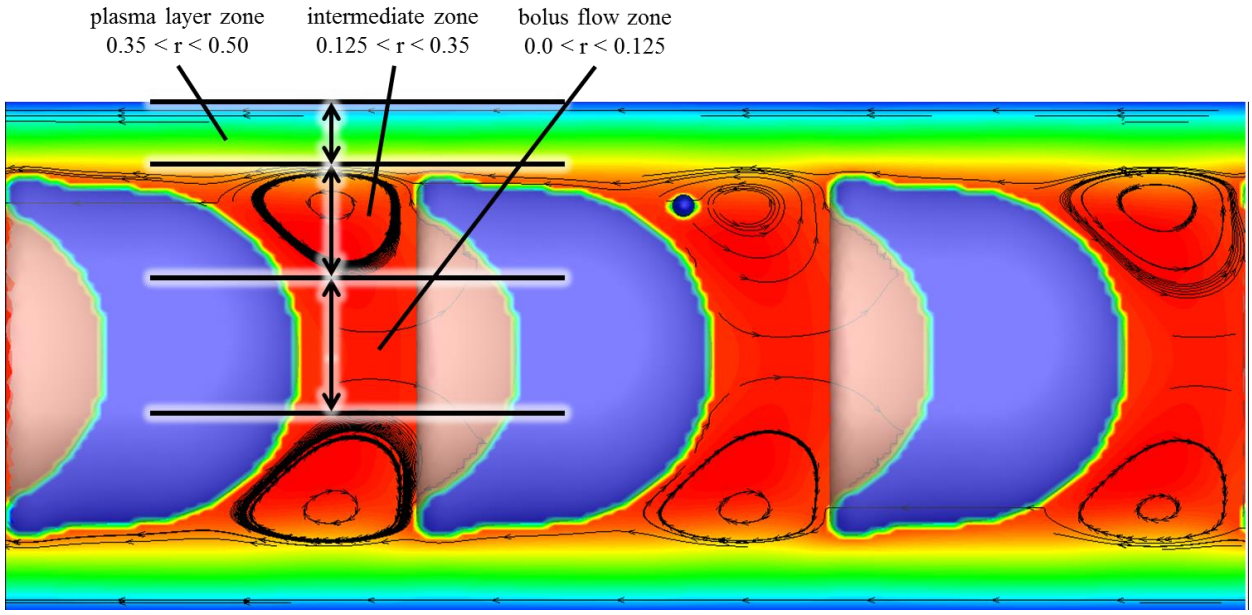

Figure 5.28. Three regions of flow are defined—the plasma layer, the intermediate zone, and the bolus flow.

The first observation is that the viscous dominated system can force rapid shifts in position and orientations of the solids. These changes can happen in durations on the order of 0.1 seconds or smaller. This was observed in the movement of both nanoparticles and bacteria. If the flow through time in a capillary is less than a second, many complex phenomena can be observed in that window of time.

Nanoparticles are smaller than the flow structures in the intermediate zone so they move around more than the bacteria. A nanoparticle in this region may end up either in the bolus region or the plasma layer—conversely, a non-motile bacterium predictably moves from the eddy region to the bolus region.

Both nanoparticles and bacterium in the bolus region or plasma layer tend to stay in those respective regions. Brownian motion increases instances of nanoparticles moving into a different region, however they can move through all three regions of the capillary due to fluid forces alone. Motile bacteria can swim out of the bolus region but tend to get stuck in the plasma layer due to the quickly passing RBC pushing them back to the wall.

Non-motile bacteria reach an equilibrium position on the order of 0.1 seconds as illustrated by Figure 5.21. Bacteria starting $0 < r < 0.35$ (bolus and intermediate zone) predictably end up in the bolus region, while bacteria starting $0.35 < r < 0.5$ stay in the plasma layer. Diffusion is negligible due to the large size of bacteria as described earlier.

Motile bacteria which start in the bolus or eddy region move out to the plasma layer during the run phase. If pointed towards an RBC, the bacteria may “idle” for a run cycle but will eventually exit after a subsequent tumble reorients it. When a bacterium tried to swim in the +x direction into the back of an RBC, it was observed to get caught and idle for one or more run cycles. The

bacteria could not pass the RBCs in the capillary so their residence time was always equal to or longer than the RBC residence time.

The mean radial velocity across all motile bacteria simulations yielded a net outward radial velocity of 2.8 μm/s. The mean radial velocity for the nanoparticles was 0.2 μm/s, and for the non-motile bacteria was -0.5 μm/s. This confirms the qualitative observation that the motile bacteria end up on the periphery of the capillary at a higher frequency than the other agents. The mean residence time of motile bacteria in a 1 mm capillary was found to be 0.78 sec. The average residence time for non-motile bacteria was 0.76 sec, and for nanoparticles 0.67 sec. These values are relatively close however it shows that motile bacteria, on average, stay in a capillary for slightly longer than the other agents. Both the higher radial velocity and longer residence time suggests that motile bacteria may by more likely to exit a capillary into the interstitium. At the population level, this may result in higher concentrations of therapeutic in the tumor.

5.6 Future Work

A fundamental strategy for modeling human capillaries and bacteria in a dynamic fluid environment has been laid out in the present work. However, there are several possible improvements to the model which could be made. Also, there are several additional paths to carry the work forward in new directions. This section will feature six modifications to the current model, followed by two examples of other problems which could be examined using ideas and methods from the present work.

Once aspect of therapeutic transport not explored in this work is the effect of varying parameters in the simulations. A characteristic value for capillary diameter, flow velocity, and hematocrit

were chosen, however these parameters could be varied to see how transport changes in capillaries with different properties. Additionally, the bacteria motility parameters could be varied to model other strains or species of bacteria. The size of nanoparticles could also be varied over a larger range, especially including smaller particles in the 10–100 nm range.

Additionally, several modifications could be made to the capillary model. The first and simplest modification would be to relax the assumption of uniformly space RBCs in the axial direction. From optical images of capillary flow it is clear that the RBCs are not perfectly spaced. A given hematocrit can be maintained while varying the spacing between consecutive red blood cells in a line. This could be parameterized by taking the standard deviation of gap length. For uniformly spaced cells, the standard deviation would be minimum at zero. It would be interesting to look at how plasma flow patterns and drug transport are impacted by varying the standard deviation of gap length for a fixed hematocrit. A three RBC periodic framework may not be sufficient for this study since the number of gap lengths to modify is small. A five to eight RBC periodic domain may be effective for this study.

A second modification would be to relax the assumption of axisymmetric RBC shape. Red blood cells approach axis symmetry at low capillary diameters and high flow velocities. This assumption was validated (see Chapter 3), however physiological capillary diameters and flow velocities in tumors are on the edge of the range at which axis symmetry can be assumed. Further, the present human capillary model works for non-axisymmetric RBCs. Asymmetry can be parameterized by the ratio of the cell length at the shortest and longest points. An axisymmetric cell would have a ratio of 1. It would be insightful to look at plasma flow and drug transport at varying degrees of asymmetry.

A third modification would be to model fenestration in the capillary wall. The effect of fenestration could be studied by modeling flow seeping in or out of a smooth capillary wall. Another way to implement fenestration would be to resolve actual pores in the capillary wall.

A fourth modification would be to model the endothelial surface layer (ESL). This is a thin layer of protein fibers which lie near the capillary wall. There have been several studies quantifying the properties of the ESL as well as several studies examining how it can be modeled [49, 57].

A fifth modification would be to model branching capillaries. When a capillary branches, it may have a significant effect on the local flow field. This may impact the distribution of bacteria or nanoparticles in blood vessel.

The sixth and last modification presented here would be to model actively deforming red blood cells. This could be done either using a coupled finite element solver (fluid structure interaction), or by some simplified fluid force-membrane stress balance.

The present work on intracapillary therapeutic transport could be used as the basis for studying penetration into a solid tumor on a larger scale than simply the capillary level. One method of doing this would be to model approximately 100 μm of tissue surrounding the capillary. A porous media model could be applied to approximate the extra cellar matrix (ECM) in the interstitium. Bacteria or nanoparticles could exit the capillary through fenestration and swim or diffuse through the interstitium. Chemotaxis or quorum sensing could be modeled in this framework by solving species equations to track the transport of chemoeffectors [68].

Another possible set up would be to model the tumor on a macro scale. Species equations could be solved to model the distribution of VEGF in the tumor. An angiogenesis model could be implemented to grow blood vessels based on the local concentration of VEGF [92]. Results from capillary simulations such as in the present work could be used to determine the rate at which

therapeutics enter the interstitium. This could be variable and based on the flow rate and diameter of a given blood vessel. The tumor could be modeled using a variable property porous media. The geometry could be reconstructed from imaging data. Additional species equations could be solved to model chemoeffectors in the tumor. Bacteria could be modeled as point particles with effects of chemotaxis included in their motility model.

Appendix

Below is the general structure of GenIDLEST with the IBM section to the left. The portion modified for the present work is indicated in red.

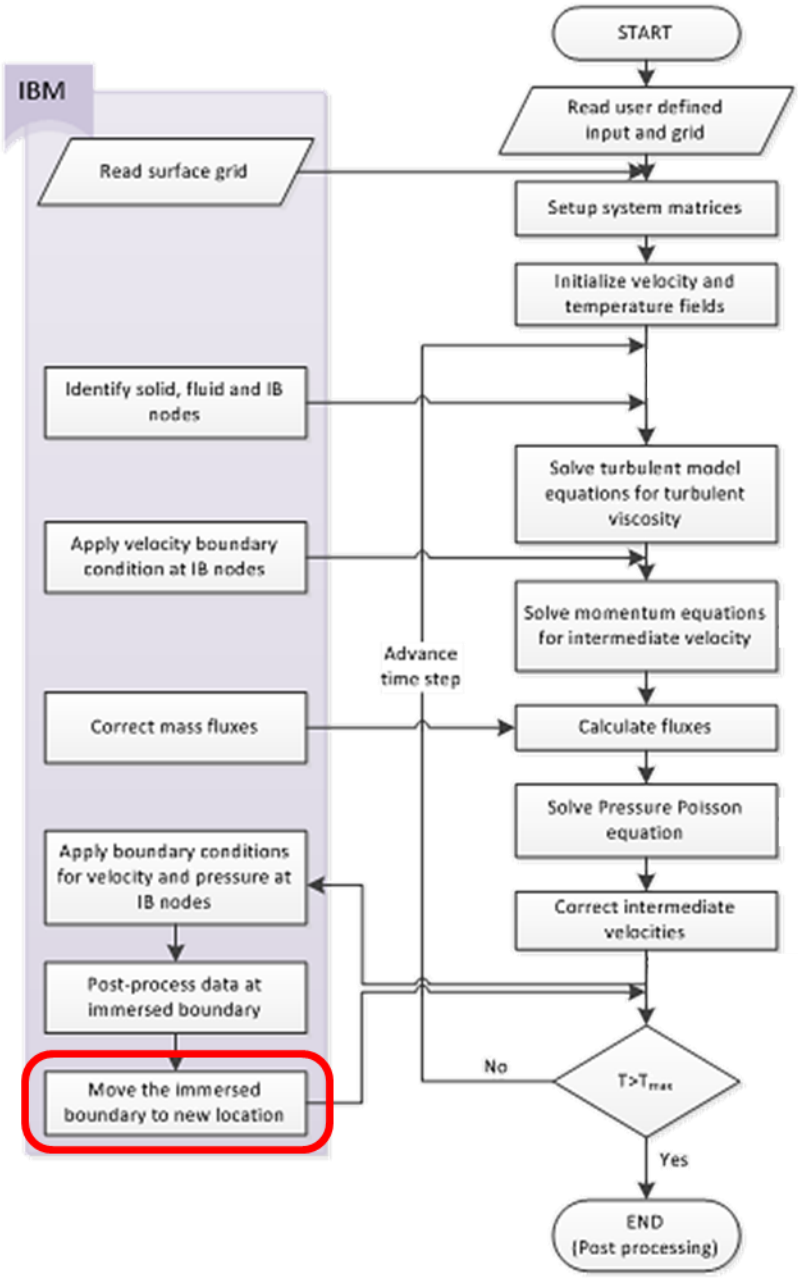

These modifications are shown in more detail below in a subroutine call graph. The subroutine ibm_solid_movement() is called from the top level program (genidlest.f) and contains all the movement, bacteria motility, and contact related code.

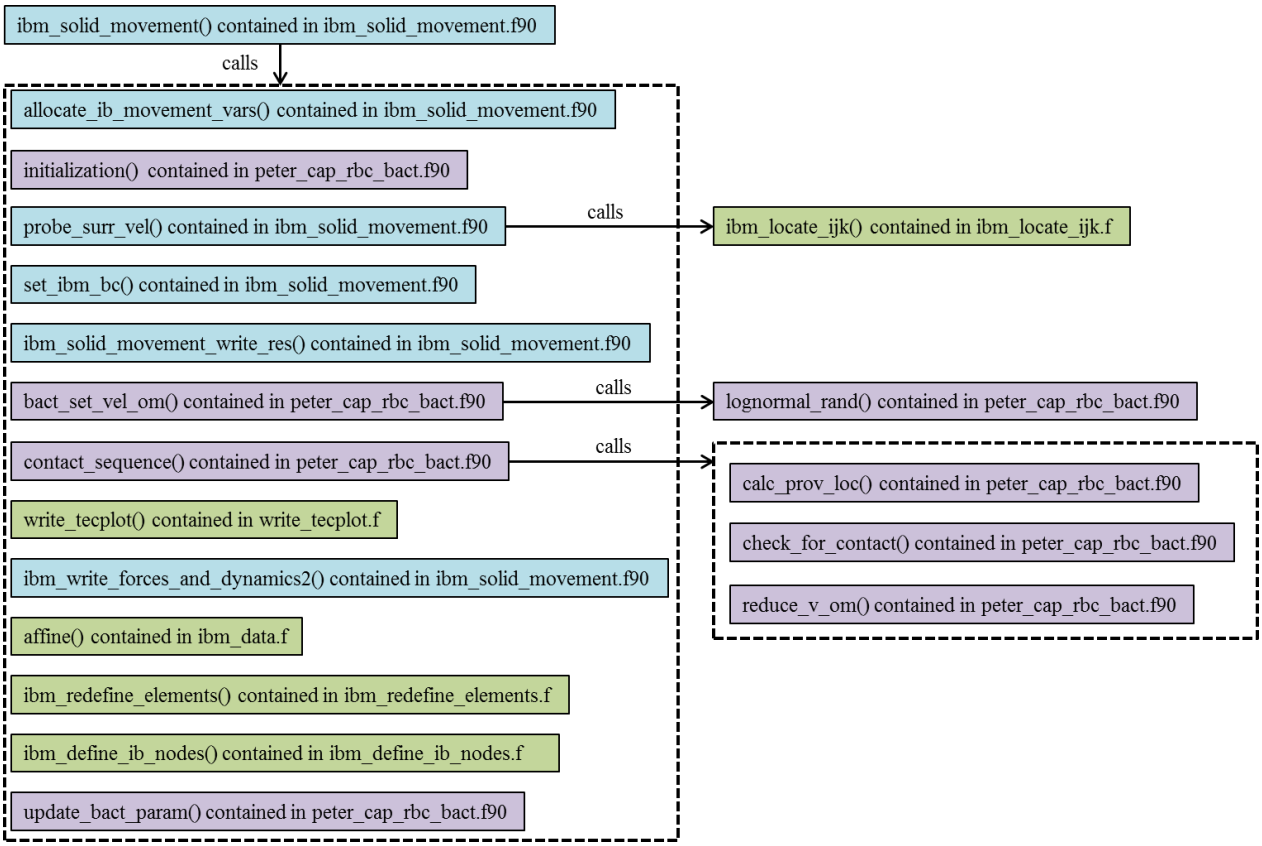

Blue subroutines are contained in the file ibm_solid_movement.f90, purple subroutines are contained in the file peter_cap_bact.f90, and green subroutines are contained in various files from the existing body of code comprising GenIDLEST.

References

[1] Y. H. Bae, R. J. Mrsny, and K. Park, *Cancer Targeted Drug Delivery: An Elusive Dream*, New York: Springer, 2013.

[2] P. Koumoutsakos, I. Pivkin, and F. Milde, "The Fluid Mechanics of Cancer and Its Therapy," *Annual Review of Fluid Mechanics,* vol. 45, no. 1, pp. 325–355, 2013.

[3] M. Hejmadi, *Introduction to Cancer Biology,* Bookboon, 2009.

[4] V. P. Chauhan, T. Stylianopoulos, Y. Boucher, and R. K. Jain, "Delivery of Molecular and Nanoscale Medicine to Tumors: Transport Barriers and Strategies," *Annual Review of Chemical and Biomolecular Engineering,* vol. 2, no. 1, pp. 281–298, 2011.

[5] D. Hanahan and R. A. Weinberg, "The Hallmarks of Cancer," *Cell,* vol. 100, pp. 57–70, 2000.

[6] Y. H. Bae and K. Park, "Targeted drug delivery to tumors: Myths, reality and possibility," *Journal of Controlled Release*, vol. 153, no. 3. pp. 198–205, 2011.

[7] A. Z. Wang, R. Langer, and O. C. Farokhzad, "Nanoparticle Delivery of Cancer Drugs," *Annual Review of Medicine*, vol. 63, no. 1, pp. 185–198, 2012.

[8] J. M. Pawelek, K. B. Low, and D. Bermudes, "Bacteria as tumour-targeting vectors," *Lancet Oncology,* vol. 4, no. 9. pp. 548–556, 2003.

[9] C. Agorio, F. Schreiber, M. Sheppard, P. Mastroeni, M. Fernandez, M. A. Martinez, *et al.*, "Live attenuated *Salmonella* as a vector for oral cytokine gene therapy in melanoma," *Journal of Gene Medicine,* vol. 9, no. 5, pp. 416–23, 2007.

[10] S. A. Rosenberg, P. J. Spiess, and D. E. Kleiner, "Antitumor Effects in Mice of the Intravenous Injection of Attenuated *Salmonella Typhimurium*," *Journal of Immunotherapy,* vol. 25, no. 3, pp. 218–25, 2002.

[11] K. Westphal, S. Leschner, J. Jablonska, H. Loessner, and S. Weiss, "Containment of Tumor-Colonizing Bacteria by Host Neutrophils," *Cancer Research*, vol. 68, no. 8, pp. 2952–2960, 2008.

[12] N. S. Forbes, "Engineering the perfect (bacterial) cancer therapy," *Nature Reviews Cancer,* vol. 10, no. 11, pp. 785–794, 2013.

[13] M. Loeffler, G. Le'Negrate, M. Krajewska, and J. C. Reed, "*Salmonella typhimurium* engineered to produce CCL21 inhibit tumor growth," *Cancer Immunology Immunotherapy*, vol. 58, no. 5, pp. 769–775, 2009.

[14] D. K. Tafti, "GenIDLEST: A scalable parallel computational tool for simulating complex turbulent flows," *ASME-PUBLICATIONS-FED*, vol. 256, pp. 347–356, 2001.

[15] S. V. Patankar, C. H. Liu, and E. M. Sparrow, "Fully Developed Flow and Heat Transfer in Ducts Having Streamwise-Periodic Variations of Cross-Sectional Area," *Journal of Heat Transfer*, vol. 99, no. 2, p. 180, 1977.

[16] L. W. Zhang, D. K. Tafti, F. M. Najjar, and S. Balachandar, "Computations of flow and heat transfer in parallel-plate fin heat exchangers on the CM-5: effects of flow unsteadiness and three-dimensionality," *International Journal of Heat and Mass Transfer*, vol. 40, no. 6, pp. 1325–1341, 1997.

[17] K. Nagendra, D. K. Tafti, and K. Viswanath, "A new approach for conjugate heat transfer problems using immersed boundary method for curvilinear grid based solvers," *Journal of Computational Physics*, vol. 267, pp. 225–246, 2014.

[18] R. Mittal and G. Iaccarino, "Immersed Boundary Methods," *Annual Review of Fluid Mechanics*, vol. 37, no. 1, pp. 239–261, 2005.

[19] J. Diebel, "Representing attitude: Euler angles, unit quaternions, and rotation vectors," *Matrix*, vol. 58, pp. 1–35, 2006.

[20] H. C. Berg, *Random Walks in Biology*, Princeton, NJ: Princeton University Press, 1993.

[21] K. B. Chandran, S. E. Rittgers and A. P. Yoganathan, *Biofluid Mechanics: The Human Circulation*, Boca Raton, FL: CRC Press, Taylor & Francis Group, 2012.

[22] C. Chernecky and B. Berger, *Laboratory Tests and Diagnostic Procedures*, 6th ed. St. Louis, MO: Elsevier/Saunders, 2013.

[23] V. Kumar, A. Abbas, J. Aster and S. Robbins, *Robbins Basic Pathology*, 9th ed. Philadelphia, PA: Elsevier/Saunders, 2013.

[24] M. Brust, C. Schaefer, R. Doerr, L. Pan, M. Garcia, P. E. Arratia, *et al.*, "Rheology of Human Blood Plasma: Viscoelastic Versus Newtonian Behavior," *Physical Review Letters*, vol. 110, no. 7, 2013.

[25] G. Késmárky, P. Kenyeres, M. Rábai, and K. Tóth, "Plasma viscosity: A forgotten variable," *Clinical Hemorheology and Microcirculation*, vol. 39, pp. 243–246, 2008.

[26] R. Hillman, K. Ault and H. Rinder, *Hematology in Clinical Practice*, 4th ed. New York: McGraw-Hill, Medical Pub. Division, 2005.

[27] W. X. Pan, D. A. Fedosov, B. Caswell, and G. E. Karniadakis, "Predicting dynamics and rheology of blood flow: A comparative study of multiscale and low-dimensional models of red blood cells," *Microvascular Research*, vol. 82, pp. 163–170, 2011.

[28] R. N. Pittman, *Regulation of Tissue Oxygenation*, Morgan & Claypool Life Sciences, 2011. [Online]. Available: http://bit.ly/2fO9bQ0

[29] A. S. Tsiftsoglou, I. S. Vizirianakis, and J. Strouboulis, "Erythropoiesis: Model Systems, Molecular Regulators, and Developmental Programs," *IUBMB Life*, vol. 61, no. 8. pp. 800–830, 2009.

[30] P. R. Zarda, S. Chien, and R. Skalak, "Elastic Deformations of Red Blood-Cells," *Journal of Biomechanics*, vol. 10, pp. 211–221, 1977.

[31] Electron Microscopy Facility at The National Cancer Institute at Frederick (NCI-Frederick) 2014. [Online]. Available: http://bit.ly/2go9lRU

[32] D. H. Boal, "Computer-Simulation of a Model Network for the Erythrocyte Cytoskeleton," *Biophysical Journal*, vol. 67, pp. 521–529, 1994.

[33] G. R. Cokelet, H. J. Meiselman, and D. E. Brooks, *Erythrocyte Mechanics and Blood Flow*, New York: A.R. Liss, 1980.

[34] J. Li, G. Lykotrafitis, M. Dao, and S. Suresh, "Cytoskeletal dynamics of human erythrocyte," *Proceedings of the National Academy of Sciences*, vol. 104, pp. 4937–4942, 2007.

[35] A. Nans, N. Mohandas, and D. L. Stokes, "Native Ultrastructure of the Red Cell Cytoskeleton by Cryo-Electron Tomography," *Biophysical Journal*, vol. 101, pp. 2341–2350, 2011.

[36] M. Dao, C. T. Lim, and S. Suresh, "Mechanics of the human red blood cell deformed by optical tweezers," *Journal of the Mechanics and Physics of Solids*, vol. 51, pp. 2259–2280, 2003.

[37] D. H. Boal, *Mechanics of the Cell*, Cambridge, UK: Cambridge University Press, 2002.

[38] R. M. Hochmuth, "Micropipette aspiration of living cells," *Journal of Biomechanics*, vol. 33, pp. 15–22, 2000.

[39] M. M. Guest, J. R. Derrick, R. G. Cooper, and T. P. Bond, "Red Blood Cells: Change in Shape in Capillaries," *Science,* vol. 142, pp. 1319–1321, 1963.

[40] R. Skalak and P. I. Branemark, "Deformation of Red Blood Cells in Capillaries," *Science,* vol. 164, pp. 717–719, 1969.

[41] K. L. Lin, L. Lopez, and J. D. Hellums, "Blood Flow in Capillaries," *Microvascular Research,* vol. 5, pp. 7–19, 1973.

[42] P. B. Canham, "Minimum Energy of Bending as a Possible Explanation of Biconcave Shape of Human Red Blood Cell," *Journal of Theoretical Biology,* vol. 26, pp. 61–81, 1970.

[43] C. Pozrikidis, *Modeling and simulation of capsules and biological cells*, Boca Raton, FL: Chapman & Hall/CRC, 2003.

[44] A. S. Popel, "Theory of Oxygen-Transport to Tissue," *Critical Reviews in Biomedical Engineering,* vol. 17, pp. 257–321, 1989.

[45] A. C. Barnard, L. Lopez, and J. D. Hellums, "Basic theory of blood flow in capillaries," *Microvascular Research,* vol. 1, no. 1, pp. 23–34, 1968.

[46] T. W. Secomb, R. Skalak, N. Özkaya, and J. F. Gross, "Flow of axisymmetric red blood cells in narrow capillaries," *Journal of Fluid Mechanics,* vol. 163, pp. 405–423, 1986.

[47] J. B. Freund, "Numerical Simulation of Flowing Blood Cells," *Annual Review of Fluid Mechanics,* vol. 46, no. 1, pp. 67–95, 2014.

[48] V. Cristini and G. S. Kassab, "Computer modeling of red blood cell rheology in the microcirculation: A brief overview," *Annals of Biomedical Engineering,* vol. 33, pp. 1724–1727, 2005.

[49] A. R. Pries and T. W. Secomb, "Microvascular blood viscosity in vivo and the endothelial surface layer," *American Journal of Physiology-Heart and Circulatory Physiology,* vol. 289, pp. H2657–H2664, 2005.

[50] R. Fahraeus and T. Lindqvist, "The viscosity of the blood in narrow capillary tubes," *American Journal of Physiology,* vol. 96, pp. 562–568, 1931.

[51] K. H. Albrecht, P. Gaehtgens, A. Pries, and M. Heuser, "Fahraeus Effect in Narrow Capillaries (id 3.3 to 11.0 μm)," *Microvascular Research,* vol. 18, pp. 33–47, 1979.

[52] M. Sugihara-Seki and B. M. M. Fu, "Blood flow and permeability in microvessels," *Fluid Dynamics Research,* vol. 37, pp. 82–132, 2005.

[53] R. M. Hochmuth, R. N. Marple, and S. P. Sutera, "Capillary blood flow. I. Erythrocyte deformation in glass capillaries," *Microvascular Research,* vol. 2, pp. 409–19, 1970.

[54] P. Gaehtgens, C. Duhrssen, and K. H. Albrecht, "Motion, deformation, and interaction of blood cells and plasma during flow through narrow capillary tubes," *Blood Cells,* vol. 6, pp. 799–817, 1980.

[55] A. R. Pries, D. Neuhaus, and P. Gaehtgens, "Blood Viscosity in Tube Flow: Dependence on Diameter and Hematocrit," *American Journal of Physiology,* vol. 263, pp. H1770–H1778, 1992.

[56] T. W. Secomb and A. R. Pries, "Blood viscosity in microvessels: Experiment and theory," *Comptes Rendus Physique,* vol. 14, pp. 470–478, 2013.

[57] E. R. Damiano, "The effect of the endothelial-cell glycocalyx on the motion of red blood cells through capillaries," *Microvascular Research,* vol. 55, pp. 77–91, 1998.

[58] F. R. Blattner, G. Plunkett, C. A. Bloch, N. T. Perna, V. Burland, M. Riley, *et al.*, "The complete genome sequence of *Escherichia coli* K-12," *Science,* vol. 277, no. 5331, pp. 1453–1462, 1997.

[59] R. M. Macnab, "Flagella and Motility," in *Escherichia Coli and Salmonella: Cellular and Molecular Biology,* 2nd ed., F. Neidhardt, Ed. 1996, pp. 123–145.

[60] H. C. Berg, "Motile behavior of bacteria," *Physics Today,* vol. 53, pp. 24–29, 2000.

[61] H. C. Crenshaw, "A new look at locomotion in microorganisms: Rotating and translating," *American Zoologist,* vol. 36, pp. 608–618, 1996.

[62] E. M. Purcell, "Life at Low Reynolds-Number," *American Journal of Physics,* vol. 45, pp. 3–11, 1977.

[63] R. Vogel and H. Stark, "Rotation-Induced Polymorphic Transitions in Bacterial Flagella," *Physical Review Letters,* vol. 110, 2013.

[64] H. C. Berg, *E. coli in Motion,* New York: Springer, 2004.

[65] L. Turner, L. Ping, M. Neubauer, and H. C. Berg, "Visualizing Flagella while Tracking Bacteria," *Biophysical Journal,* vol. 111, pp. 630–639, 2016.

[66] L. Turner, W. S. Ryu, and H. C. Berg, "Real-time imaging of fluorescent flagellar filaments," *Journal of Bacteriology,* vol. 182, pp. 2793–2801, 2000.

[67] H. C. Berg, "Chemotaxis in Bacteria," *Annual Review of Biophysics and Bioengineering,* vol. 4, pp. 119–136, 1975.

[68] T. Hillen and K. J. Painter, "A user's guide to PDE models for chemotaxis," *Journal of Mathematical Biology,* vol. 58, pp. 183–217, 2009.

[69] B. Geuther and B. Behkam, "Towards Quorum Sensing Based Distributed Control for Networks of Mobile Sensors," *2013 IEEE/RSJ International Conference on Intelligent Robots and Systems (IROS),* pp. 1549–1554, 2013.

[70] R. Maniyeri and S. Kang, "Numerical study on bacterial flagellar bundling and tumbling in a viscous fluid using an immersed boundary method," *Applied Mathematical Modelling,* vol. 38, pp. 3567–3590, 2014.

[71] S. Lim and C. S. Peskin, "Fluid-mechanical interaction of flexible bacterial flagella by the immersed boundary method," *Physical Review E,* vol. 85, 2012.

[72] C. Y. Hsu and R. Dillon, "A 3D Motile Rod-Shaped Monotrichous Bacterial Model," *Bulletin of Mathematical Biology,* vol. 71, pp. 1228–1263, 2009.

[73] H. C. Berg and D. A. Brown, "Chemotaxis in *Escherichia coli* analyzed by Three-dimensional Tracking," *Nature,* vol. 239, pp. 500–504, 1972.

[74] W. H. Press, *Numerical Recipes: The Art of Scientific Computing*, 3rd ed. Cambridge, MA: Cambridge University Press, 1989.

[75] N. Pfennig, "Photosynthetic Bacteria," *Annual Review of Microbiology,* vol. 21, pp. 285–324, 1967.

[76] B. L. Taylor, I. B. Zhulin, and M. S. Johnson, "Aerotaxis and other energy-sensing behavior in bacteria," *Annual Review of Microbiology,* vol. 53, pp. 103–128, 1999.

[77] R. P. Blakemore, "Magnetotactic Bacteria," *Annual Review of Microbiology,* vol. 36, pp. 217–238, 1982.

[78] P. D. Frymier, R. M. Ford, H. C. Berg, and P. T. Cummings, "Three-dimensional tracking of motile bacteria near a solid planar surface," *Proceedings of the National Academy of Sciences,* vol. 92, pp. 6195–6199, 1995.

[79] W. R. DiLuzio, L. Turner, M. Mayer, P. Garstecki, D. B. Weibel, H. C. Berg, *et al.*, "*Escherichia coli* swim on the right-hand side," *Nature,* vol. 435, pp. 1271–1274, 2005.

[80] E. Lauga, W. R. DiLuzio, G. M. Whitesides, and H. A. Stone, "Swimming in circles: Motion of bacteria near solid boundaries," *Biophysical Journal,* vol. 90, pp. 400–412, 2006.

[81] A. P. Berke, L. Turner, H. C. Berg, and E. Lauga, "Hydrodynamic attraction of swimming microorganisms by surfaces," *Physical Review Letters,* vol. 101, 2008.

[82] K. J. Duffy, P. T. Cummings, and R. M. Ford, "Random-Walk Calculations for Bacterial Migration in Porous-Media," *Biophysical Journal,* vol. 68, pp. 800–806, 1995.

[83] J. W. Barton and R. M. Ford, "Mathematical model for characterization of bacterial migration through sand cores," *Biotechnology and Bioengineering,* vol. 53, pp. 487–496, 1997.

[84] A. J. Wolfe and H. C. Berg, "Migration of Bacteria in Semisolid Agar," *Proceedings of the National Academy of Sciences,* vol. 86, pp. 6973–6977, 1989.

[85] N. A. Licata, B. Mohari, C. Fuqua, and S. Setayeshgar, "Diffusion of Bacterial Cells in Porous Media," *Biophysical Journal,* vol. 110, pp. 247–257, 2016.

[86] A. Sokolov and I. S. Aranson, "Physical Properties of Collective Motion in Suspensions of Bacteria," *Physical Review Letters,* vol. 109, 2012.

[87] K. C. Chen, R. M. Ford, and P. T. Cummings, "Mathematical models for motile bacterial transport in cylindrical tubes," *Journal of Theoretical Biology,* vol. 195, 1998.

[88] L. Zhu, E. Lauga, and L. Brandt, "Low-Reynolds-number swimming in a capillary tube," *Journal of Fluid Mechanics,* vol. 726, pp. 285–311, 2013.

[89] B. Liu, K. S. Breuer, and T. R. Powers, "Propulsion by a helical flagellum in a capillary tube," *Physics of Fluids,* vol. 26, 2014.

[90] L. Formaggia, A. Quarteroni, and A. Veneziani, *Cardiovascular Mathematics: Modeling and Simulation of the Circulatory System,* Milan, Italy: Springer, 2009.

[91] Y. C. Fung, *Biomechanics: Circulation*, 2nd ed. New York, NY: Springer, 2009.

[92] T. L. Jackson, *Modeling Tumor Vasculature: Molecular, Cellular, and Tissue Level Aspects and Implications,* New York, NY: Springer, 2012.